CZECH TECHNICAL UNIVERSITY IN PRAGUE
Faculty of Civil Engineering

Ph.D. Programme: Civil Engineering
Branch of study: Physical and Material Engineering

Ing. Jan Vorel

Multi-scale Modeling of Composite Materials

Víceúrovňové modelování kompozitních materiálů

DOCTORAL THESIS FOR OBTAINING THE DEGREE OF Ph.D.

Supervisor: Prof. Ing. Michal Šejnoha, Ph.D., DSc.

November, 2009

ACKNOWLEDGMENTS

First of all, I would like to express my deepest gratitude to Prof. Ing. Michal Šejnoha, Ph.D., DSc. and Prof. Ing. Jiří Šejnoha, DrSc. for their support and patience not only during the whole course of the work on this thesis but also during my whole studies.

I wish also to thank other colleagues who have given me valuable comments and advice.

Most importantly, I would like to thank my parents, my brother and friends for their never ending encouragement and support that help me to attain the goal I have set for myself and the opportunity to fully concentrate on my study.

Last but not least, the financial support provided by the GAČR Grant No. 106/07/1244 and partially by the research project CEZ MSM 684077003 is also gratefully acknowledged.

TABLE OF CONTENTS

List of Figures iv

List of Tables vii

Abstract (english) viii

Abstrakt (czech) x

Notation xii

Chapter 1: Introduction 1

1.1 Motivation 1

1.2 Carbon-Carbon composites 5

1.2.1 Tow path imperfections 6

1.2.2 Porosity 8

1.2.3 Material models 9

1.2.4 Image analysis 10

1.2.5 Length scales 10

Chapter 2: Conceptual and methodical approaches 13

2.1 Methods based on statistical information 14

2.1.1 Mean field approaches (MFAs) 14

2.1.2 Variational bounding methods (VBMs) 19

2.2 Methods studying discrete microstructure 21

2.2.1 Periodic microfield approaches (PMAs) 22

2.2.2 Embedded cell approaches (ECAs) 25

2.2.3 Window approaches (WAs) 26

Chapter 3: Experimental program **27**

3.1 Two-dimensional image analysis 28

3.2 Three-dimensional X-ray microtomography 30

3.3 Phase elastic moduli from nanoindentation 30

3.4 Laboratory evaluation of effective properties 33

Chapter 4: Modeling strategy of C/C plain weave composites **36**

4.1 Statistically equivalent period unit cell 36

4.1.1 Quantification of random microstructure 37

4.1.2 Calibration of SEPUC parameters 37

4.1.3 Verification of optimization procedure 38

4.1.4 Multi-layered C/C composites 40

4.2 Micro-scale 41

4.3 Meso-scale 42

4.3.1 Mori-Tanaka analysis 43

4.3.2 Finite element analysis - computational model 45

4.4 Macro-scale 47

Chapter 5: Evaluation of effective material properties **51**

5.1 Mori-Tanaka analysis 54

5.1.1 Micro-scale 55

5.1.2 Meso-scale 58

5.1.3 Macro-scale 66

5.2 Finite element analysis 67

5.2.1 SEPUC 68

5.2.2 Representative PUCs 71

5.3 Conclusions 72

Chapter 6: Conclusions and future perspectives **77**

Bibliography **79**

List of author's publications **91**

Appendix A: Eshelby's tensor for an ellipsoidal inclusion **96**

Appendix B: $\mathrm{HE_LP}$ program **98**

B.1 Basic specifications and method 98

B.2 User guide 98

B.2.1 Effective elastic properties and thermal conductivities 99

B.2.2 Weave composite 100

B.2.3 Input/Output file 102

Appendix C: Numerical Modeling of Strain Hardening Fiber-Reinforced Composites **103**

C.1 Introduction 103

C.2 Model definition 104

C.2.1 Poisson's ratio effect and equivalent principal stresses 106

C.2.2 Equivalent stress 107

C.2.3 Biaxial behavior 111

C.2.4 Cyclic loading 112

C.3 Implementation and application 113

C.4 Conclusion and future work 116

LIST OF FIGURES

1.1 Real composite system 3
1.2 Example of complex structure of C/C composites: (a) Plain view of C/P composite, (b) cross section of ten-layer C/C composite 4
1.3 Basic structural components of woven C/C composite 10
1.4 Multi-scale: (a) Macro-scale, (b) meso-scale, (c) micro-scale 11
1.5 Grayscale images of a real composite system identifying individual scales . 12

2.1 Mean field approaches: (a) The dilute approximation, (b) the self-consistent method, (c) the Mori-Tanaka method 15
2.2 Microstructure: (a) Cubic arrangement, (b) hexagonal arrangement, (c) real (quasi-periodic) structure 21
2.3 Conditions of periodicity 25
2.4 Schematic depiction: (a) Embedded cell approach, (b) window approaches . 26

3.1 Examples of scanned microstructures: (a) Woven fabric, (b) carbonized composite, (c) graphitized composite 28
3.2 Image processing steps: (a) Manual marking of object borders, (b) automatic marking of objects 29
3.3 Examples of image analysis: (a) Woven fabric, (b) multi-layered C/C composite 29
3.4 X-ray microtomography: (a) Interior distribution and shape of large vacuoles, (b) three-dimensional view of the porous composite structure 31
3.5 Nanoindentation - location of indents: (a) Transverse direction, (b) longitudinal direction (compression) 32

4.1 The resulting three-dimensional scheme of the statistically optimal unit cell 41
4.2 Homogenization on micro-scale: (a) Fiber tow composite, (b) fiber-matrix composite 41

4.3 Inclination angles: (a) Example of a real histogram, (b) approximate distribution (PUC) 43
4.4 Idealized geometrical model for plane weaved composite: (a) Geometrical parameters, (b) three-dimensional view 44
4.5 Local coordinate system and definition of the Euler angles 44
4.6 Geometrical model of two-layer SEPUC (two-dimensional cut) 46
4.7 Computational model: (a) Two-dimensional cut of a two-layer model with voids (b) 3D view of the geometry of a two-layer UC model with voids . . 46
4.8 Finite element mesh generation: (a) Primitive volume, (b) one layer of reinforcements,(c) two layers of reinforcements, (d) two layers of reinforcements with voids, (e) FEM mesh of tows and voids, (f) FEM mesh of SEPUC . . 48
4.9 Micromechanics and macromechanics 49

5.1 Evolution of the objective function as a function of the aspect ratio 57
5.2 Evolution of the objective function as a function of the aspect ratio: (a) Heat conduction problem, (b) elasticity 62
5.3 Homogenization on meso-scale: (a)-(b) PUC1 representing carbon tow-carbon matrix composite, (c)-(d) PUC2 with vacuoles aligned with delamination cracks due to slip of textile plies, (e)-(f) PUC3 with extensive vacuoles representing the parts with textile reinforcement reduction due to bridging effect in the middle ply 67
5.4 Comparison of the numerical and experimental results: (a) Coefficients of thermal conductivity, (b) elastic properties 75

A.1 Case study: Effective conductivities as a function of the volume fraction of the porous phase 97

B.1 $\mathbf{HE_LP}$ window structure: (a) Common tool strip buttons, (b) general informations, (c) matrix properties, (d) inclusions (tows) properties, (e) result viewer 99

B.2 Heat conduction: (a) Thermal conduction matrix, (b) matrix volume fraction, (c) inclusion list, (d) semi-axes, (e) Euler angles, (f) material properties for an inclusion, (g) name and volume fraction, (h) output window 100

B.3 Weave composite: (a) Problem type, (b) PUC dimensions, (c) matrix properties, (d) tows volume fraction, (e) semi-axes, (f) Euler angles, (g) material properties for bundles, (h) homogenization type, (i) output window 101

C.1 Coordinates and transformation angle 104

C.2 Tensile response: (a) Virgin loading, (b) loading/unloading 107

C.3 Tension: (a) Evolution of inelastic strain, (b) comparison of softening branches 109

C.4 Compressive response: (a) Virgin loading, (b) loading/unloading 110

C.5 Failure envelope in the principal stress space 112

C.6 Schematic cyclic behavior 114

C.7 Three-point bending test: (a) Setup, (b) results 116

C.8 Evolution of ε_{11} during three-point flexural test simulation (load vs. mid-span vertical deflection 117

LIST OF TABLES

3.1 Material parameters of individual phases 33
3.2 Phase, unidirectional (UD) C/C composite (porous fiber tow) and laminate effective thermal conductivities 34
3.3 Effective elastic properties of UD C/C composite (porous fiber tow) and C/C laminate 35

4.1 Results of the verification procedure 39
4.2 Accuracy of identified parameters 39
4.3 Bounds and optimal parameters on the two-layer SEPUC 40
4.4 Statistics of local minima 40

5.1 Effective thermal conductivities of the fiber tow for optimization 57
5.2 Effective thermal conductivities of the fiber tow 58
5.3 Effective elastic properties. Comparison of MT and measured (EXP) results 59
5.4 Quantification of PUC1 parameters 60
5.5 Effective thermal conductivities of a plain weave fabric without porosity . . 65
5.6 Effective elastic properties of a plain weave fabric without porosity 66
5.7 Effective thermal conductivities of the porous textile plies and laminates . . 68
5.8 Effective elastic properties of the porous textile plies and laminates 69
5.9 Effective thermal conductivities of the laminate 70
5.10 Effective elastic properties of the laminate 70
5.11 Parameters of the periodic unit cell 71
5.12 Effective thermal conductivities of the SEPUC 71
5.13 Effective elastic properties of the SEPUC 72
5.14 Correlation matrix 72
5.15 Effective thermal conductivities and elastic properties for different PUCs . . 73

C.1 Model parameters 115

Czech Technical University in Prague

Abstract

Multi-scale Modeling of Composite Materials

Jan Vorel

Many industrial and engineering materials as well as the majority of natural materials are inhomogeneous, i.e. they consist of dissimilar constituents (phases) that are distinguishable at some (small) length scale. Each constituent shows different material properties or material orientations and may itself be inhomogeneous at some even smaller length scale. Typical examples of inhomogeneous materials are composites, concrete, porous and cellular materials, functionally graded materials, wood, bone, and others.

The main interest of theoretical studies of multi-phase materials is targeted on the homogenization of material overall behavior (stiffness, thermal conduction, transport properties, ...) from the corresponding phase properties and geometrical arrangement. There are many variations of homogenization procedures which differ in their accuracy and computational effort.

The main focus of this thesis is the determination of effective thermomechanical properties of carbon-carbon (C/C) plain weave fabric composites, particularly the effective thermal coefficients and the effective stiffness matrices. The selection of mechanical and heat conduction problems is promoted not only by available experimental measurements but also by their formal similarity, considerably simplifying the theoretical treatment as seen hereinafter.

The C/C plain weave composites belong to an important class of high-temperature material systems. An exceptional thermal stability together with high resistance to thermal shocks or fracture following rapid and strong changes in temperature have made these materials almost indispensable in a variety of engineering spheres. While their appealing properties such as high strength, low coefficients of thermal expansion and high thermal conductivities are known, their prediction from the properties supplied by the manufacturer for individual constituents is far from being trivial since these systems are generally highly complicated.

Apart from the characteristic three-dimensional structure of textile composites the geometrical complexity is further enhanced by the presence of various imperfections in the

woven path developed during the manufacturing process. A number of models properly accounting for the three-dimensional effects have been developed in the past. However, a major shortcoming of many of these models is the omission of the porous phase, which in real systems may exceed 30% of the overall volume.

During recent years, significant research effort has been put into providing a simple yet accurate scheme for predicting the overall properties of fabric composites. With an increasing level of sophistication, these models are mostly based on the fully detailed three-dimensional finite element method (FEM) simulations. The disadvantage of the FEM-based approach is, however, a high cost associated with the analysis, not only in terms of computational time, but especially when accounting for the generation of three-dimensional finite element meshes. Moreover, incorporation of inevitable microstructural imperfections into the FEM model is far from being straightforward and requires a special treatment based on appropriate statistical characterization. On the other hand, if these obstacles are overcome, the FE simulations typically deliver more accurate results.

In the last decade, effective media theories, widely used in classical continuum micromechanics, have been recognized as an attractive alternative to FEM-based methods. Therefore, the Mori-Tanaka (MT) procedure introduced by Hatta and Taya (1986) for thermal conductivity and by Jeong et al. (1998) for electrical conductivity is utilized to determinate the effective thermal conductivity coefficients for C/C composites on the micro- and meso-scale. A similar approach is used to determined effective stiffness matrices. On both scales a two step homogenization approach is adopted. It combines the evaluation of effective properties in the absence of pores with a subsequent homogenization step in which the porous phase is introduced into a new homogenized matrix.

To take into account an inherent layered characteristic of C/C composites the laminate theory introduced by Milton (2002) is employed for elastic properties on the macro-scale and the simple rules of mixture are used to obtain the demanded thermal conductivities.

A numerical application of effective properties of composite materials is briefly demonstrated at the end of this thesis. Experimental data of Strain Hardening Cement-based Composites (SHCC) are utilized to define the numerical model based on rotating cracks. The suitability of a designed model is proved by confrontation of the numerical results with the experimental data.

České vysoké učení technické v Praze

Abstrakt

Víceúrovňové modelování kompozitních materiálů

Jan Vorel

Mnoho materiálů, které se využívají ve stavebnictví a průmyslové výrobě, stejně tak jako většina přírodních materiálů, jsou nehomogenní, tj. skládají se z rozdílných složek (fází). Složky vykazují různé materiálové vlastnosti nebo orientace a mohou být sami o sobě nehomogenní na nižší rozlišovací úrovni. Typické příklady nehomogenních materiálů jsou kompozity, beton, porézní a buněčné materiály, dřevo, atd.

Teoretické studie vícefázových materiálů jsou často zaměřeny na komplexní chování materiálu (tuhost, tepelná vodivost, transportní vlastnosti, dots), vyjadřující odpovídající vlastnosti a geometrické uspořádání. Existuje více homogenizačních postupů, které se liší v přesnosti a výpočetním úsilí.

Předložená práce je zaměřena především na určování efektivních termomechanických vlastností tkaných kompozitů uhlík-uhlík, zvláště pak na určení koeficientů tepelné vodivosti a elastických vlastností. Tato volba je provedena s ohledem jak na dostupná laboratorní měření, tak na formální podobnost mechaniky a vedení.

Tkané kompozity uhlík-uhlík se řadí do významné třídy materiálů využívaných v prostředí s vysokými teplotami. Mimořádná tepelná stabilita spolu s vysokou odolností proti porušení v důsledku rychlé změny teploty řadí tyto materiály mezi nepostradatelné v různých technických oblastech. Přestože jejich atraktivní materiálové vlastnosti (vysoké pevnosti, nízké koeficienty tepelné roztažnosti a vysoké tepelné vodivosti) jsou známy, jejich odhad z vlastností jednotlivých složek není zdaleka triviální. Toto je způsobeno především složitou strukturou těchto materiálů. Kromě charakteristické třídimenzionální (3D) geometrické struktury textilních kompozitů hraje významnou roli také přítomnost různých vad, které vznikají během výrobního procesu. Mnoho modelů bere v úvahu 3D strukturu, ale často stále trpí absencí porézní fáze, která v reálných systémech může přesáhnout 30% z celkového objemu.

Značné úsilí bylo věnováno výzkumu jednoduchého a přesného schématu pro odhad celkových vlastností materiálu. Vytvořené modely jsou většinou založeny na zcela detailní

třídimenzionální simulaci pomocí metody konečných prvků (MKP). Nevýhodou přístupu založeného na MKP je však vysoká časová náročnost spojená s analýzou. Nejedná se pouze o výpočetní čas potřebný k analýze, ale také o čas nezbytný na přípravu 3D sítě konečných prvků. Dalším neméně komplikovaným problémem je zahrnutí nedokonalosti mikrostruktury do modelu MKP a zaslouží si zvláštní zacházení na základě vhodné statistické charakterizace. Je však nutné poznamenat, že po překonáních těchto úskalí, simulace pomocí MKP nám poskytují cenné výsledky včetně detailního rozložení lokálních polí.

V posledních letech se jako výhodná alternativa ke zdlouhavé konečně prvkové analýze jeví zjišťování efektivních vlastností materiálů na základě průměrných polí, které jsou hojně užívané v mikromechanice kontinua. A proto metoda Mori-Tanaka (MT), popsaná v (Hatta and Taya, 1986) pro tepelnou vodivost a v (Jeong et al., 1998) pro elektrickou vodivost, je využita v této práci k určení koeficientů tepelné vodivosti na mikro-a mezoúrovni C/C kompozitů. Podobný přístup je použit k určení efektivní matice tuhosti. Na obou úrovních je homogenizace provedena ve dvou krocích. V prvním kroku je určena efektivní vlastnost pro materiál bez vzduchových pórů. Toto je následováno zavedením porézní fáze do nově určené efektivní matrice.

Při použití zjednodušených metod k určení efektivních vlastností je nezbytné při určení elastických vlastností na makroúrovni využít teorie pro lamináty (Milton, 2002). Efektivní tepelné vlastnosti jsou získány na základě jednoduchých průměrovacích vztahů.

Aplikace efektivních vlastností kompozitních materiálů pro numerický model je popsána v poslední části této práce. Zde jsou využita experimentální data získaná pro vláknocementové kompozity s řízenými vlastnostmi. Navržený model je založen na rotujících trhlinách pro zachycení typických vlastností vláknokompozitů, tj. zpevnění, změkčení, lokalizace. Vhodnost modelu je prokázána porovnáním numerických výsledků s experimenty.

NOTATION

General notation

$\mathbf{a}$	Vector
$\boldsymbol{a}$	Second-order tensor
$\mathbf{A}$	Fourth-order tensor
$\mathcal{A}$	Function
$\{\mathsf{a}\}$	Column vector or vectorial representation of symmetric second-order tensor
$[\mathsf{A}]$	Matrix or matrix representation of symmetric fourth-order tensor
Σ	Sum
∇	Nabla operator
$\lvert \cdot \rvert$	Absolute value
$\lVert \cdot \rVert$	Weighted arithmetic mean
$\langle \cdot \rangle$	Volumetric average
$\langle\langle \cdot \rangle\rangle$	Orientational average
$\cdot^{-1}$	Inverse of number or matrix
$\cdot^{\mathsf{T}}$	Transpose of vector or matrix

Specific notation

a	Half-period of tow undulation
$\boldsymbol{A}$	Concentration factor for temperature gradient
A_{PL}	Projected contact area at peak load
b	Tow thickness
$\boldsymbol{B}$	Concentration factor for heat flux
c	Volume fraction
$[\mathsf{C}]$	Stiffness matrix
$\mathbf{C}$	Fourth-order stiffness tensor

d	Length of PUC
E	Elastic modulus
f	Probability density function
g	Width of intra-tow gap
G	Shear modulus
h	Hight of the ply
$\mathbf{h}$	Temperature gradient
$\mathbf{H}$	Macroscopic temperature gradient
$\boldsymbol{I}$	Identity matrix
$\mathbf{l}$	Lower bound
$\mathcal{L}$	Linear path function
M	Number of laminas
N	Number of phases
$\mathcal{O}_D$	Objective function related to statistical descriptor D
$\boldsymbol{P}$	Transformation matrix
$\mathcal{P}_D$	Exponential exterior penalty function related to statistical descriptor D
$\mathbf{q}$	Heat flux
$\mathbf{Q}$	Macroscopic heat flux
$\boldsymbol{R}$	Thermal resistivity matrix
s	Centreline of the warp/weft tow
$\mathbf{S}$	Eshelby tensor
$\mathcal{S}$	Two-point probability function
T	Temperature
$\mathbf{u}$	Upper bound
v	height of PUC
$\mathbf{x}$	Local coordinate system
$\mathbf{X}$	Global coordinate system
$\mathbf{y}$	Independent parameters describing SEPUC

Γ	Boundary
$\Delta_1, \Delta_2, \Delta_3$	Shift of plies in direction of corresponding coordinate axes
ϕ, θ, β	Euler angles
ν	Poisson ration
$\xi_{1,2,3}$	Semi-axes
$\boldsymbol{\chi}$	Thermal conductivity matrix
Ω	Volume

$\cdot^{\mathsf{dil}}$	Dilute approximation
$\cdot^{\mathsf{f}}$	Fluctuation
$\cdot_f$	Fiber
$\cdot^{\mathsf{FEM}}$	Finite Element Method
$\cdot^{\mathsf{H}}$	Homogenized effective property
$\cdot^{\mathsf{MT}}$	Mori-Tanaka method
$\cdot^{\mathsf{SC}}$	Self-consistent method
$\cdot_{\mathsf{trans}}$	Transversal direction
$\cdot_v$	Void
$\cdot_{\mathsf{warp}}$	Warp tow
$\cdot_{\mathsf{weft}}$	Weft tow

Numerical model (Appendix C)

a	Parameter governing the unloading trajectory
b	Parameter governing the inelastic strains
d	Localization band in real material
$[\tilde{\mathsf{D}}]$	Tangent material stiffness matrix
$\mathbf{e}$	Principal strain vector
$\hat{e}$	Effective principal strain
$\dot{e}$	Strain increment

E	Young's modulus
h	Element size
$\mathbf{s}$	Principal stress vector
$\hat{s}$	Equivalent stress
$[\mathsf{T}]_{\varepsilon}$	Transformation matrix for strains
$[\mathsf{T}]_{\sigma}$	Transformation matrix for stresses
w_t	Crack opening for the complete force transfer loss
w_c	Displacement for the complete force transfer loss in compression
α	Rotation angle
$\Delta\boldsymbol{\varepsilon}$	Strain increment vector
$\boldsymbol{\varepsilon}$	Strain vector
ε_{cmin}	Minimum strain experienced in previous steps
ε_{tmax}	Maximum strain experienced in previous steps
ν	Poisson's ratio
$\boldsymbol{\sigma}$	Stress vector
σ_{cmin}	Stress associated with ε_{cmin}
σ_{tmax}	Stress associated with ε_{tmax}
ω	Damage parameter
$\cdot_0$	Undamaged material
$\cdot_c$	Compression
$\cdot_{c0}$	Compression state
$\cdot^{cl}$	Cyclic loading
$\cdot_{cp}$	Compression state
$\cdot_{cu}$	Compression state
$\cdot^{\mathsf{el}}$	Elastic part
$\cdot_t$	Tension

$\cdot_{t0}$ Tension state

$\cdot_{tp}$ Tension state

$\cdot_{tu}$ Tension state

Chapter 1

INTRODUCTION

Everything should be made as simple as possible, but not simpler.

Albert Einstein

The above mentioned statement simplifies the Occam's razor principle which declares that the explanation of any phenomenon should make as few assumptions as possible, eliminating those that make no difference in the observable predictions of the explanatory hypothesis or theory (Ockham, 14th-century). If we take this theorem into consideration the mean field theory is seen as a suitable and efficient tool, in comparison to finite element based methods (FEM), for the evaluation of effective material properties of composites. Note that this approach is valuable for a restricted area of interest. In other cases the FEM has a non-substitutable position.

1.1 Motivation

Well known engineering materials like brick, stone, concrete, etc. have their irreplaceable position, but the modern age is demanding new technologies and materials for use in engineering constructions which are built faster, bigger, higher, slighter, ... As somebody said: "We have had a stone age, iron age and many other ages so far. Maybe once our epoch will be called composite age." And it is true. The new invented materials are mainly composites which take an advantage of cooperation of individual constituents and diminish their weaker properties. The building industry benefits from different modern materials, even though they were not primarily created for this branch of engineering, for instance carbon-carbon composites and different types of hydrocarbons.

The correct prediction of material behavior and properties is arising in association with their applications. Many experimental tests are carried out to learn more about their charac-

teristics. Nevertheless, the computational approach is an irresistible and indestructible tool which is based on the experimentally measured data and is for that reason more than helpful, see Chapter 5. Numerical modeling allows us to design a remarkable construction as well as to reduce acquisition costs.

As mentioned above, many industrial and engineering materials as well as the majority of natural materials are inhomogeneous, i.e. they consist of dissimilar constituents (phases) that are distinguishable at some (small) length scale. Each constituent shows different material properties or material orientations and may itself be inhomogeneous at some even smaller length scales. Typical examples of inhomogeneous materials are composites, concrete, porous and cellular materials, functionally graded materials, wood, bone, and others.

The main interest of theoretical studies of multi-phase materials is targeted to the homogenization of material overall behavior (stiffness, thermal conduction, transport properties, ...) from the corresponding phase properties and geometrical arrangement. There are many variations of homogenization procedures which differ in their accuracy and computational effort (see Chapter 2).

The main focus of this thesis is the determination of effective thermomechanical properties of carbon-carbon (C/C) plain weave fabric composites, particularly the effective thermal coefficients and the effective stiffness matrices. This selection of mechanical and heat conduction problems is promoted not only by available experimental measurements but also by their formal similarity, considerably simplifying the theoretical treatment as seen hereinafter.

The C/C plain weave composites belong to an important class of high-temperature material systems (Section 1.2). An exceptional thermal stability together with high resistance to thermal shocks or fracture following rapid and strong changes in temperature have made these materials almost indispensable in a variety of engineering spheres. While their appealing properties such as high strength, low coefficients of thermal expansion and high thermal conductivities are known, their prediction from the properties supplied by the manufacturer for individual constituents is far from being trivial, because these systems are generally highly complicated.

Apart from the characteristic three-dimensional (3D) structure of textile composites the geometrical complexity is further enhanced by the presence of various imperfections in the woven path developed during the manufacturing process, Fig. 1.1. A route for incorpo-

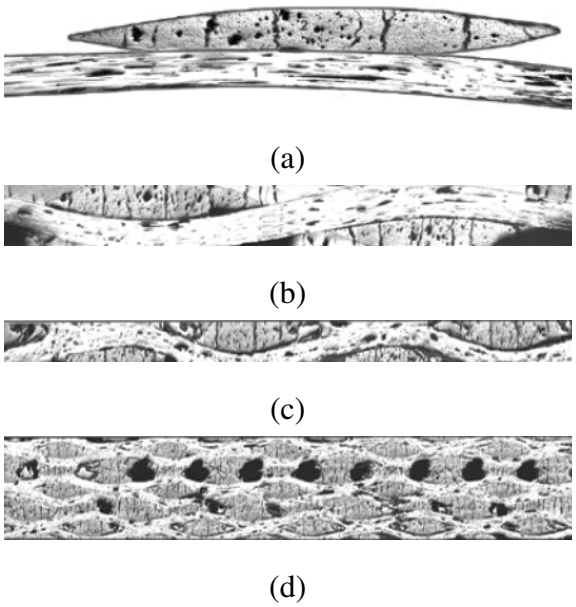

(a) (b) (c) (d)

Figure 1.1: Real composite system

rating at least the most severe imperfections in predictions of the mechanical properties of these systems has been outlined in (Zeman and Šejnoha, 2004a) in the context of statistically equivalent periodic unit cell. Although properly accounting for three-dimensional effects the resulting representative volume element still suffers from the absence of the porous phase, which in real systems, Fig. 1.2, may exceed 30% of the overall volume. As suggested in (Palán, 2002) neglecting the material porosity may severely overestimate the resulting thermal properties of textile composites.

During recent years, significant research effort has been put into providing a simple yet accurate scheme for predicting the overall properties of fabric composites. With an increasing level of sophistication, these models are mostly based on the fully detailed three-dimensional finite element method (FEM) simulations, see (Tomková et al., 2007). It is generally accepted that this class of models is the most accurate one when supplied with reliable geometrical data based on, e.g., micrographs of a composite structure (Fig. 1.2(b)). The disadvantage of the FEM-based approach is, however, a high cost associated with the analysis, not only in terms of computational time but especially when accounting for the generation of three-dimensional finite element meshes. Moreover, incorporation of inevitable microstructural imperfections into the FEM model is far from being straightforward and requires a special treatment based on appropriate statistical characterization, see Section 4.1.

On the other hand, if these obstacles are overcome, the FE simulations typically deliver more accurate results (Section 5.2).

(a) (b)

Figure 1.2: Example of complex structure of C/C composites: (a) Plain view of C/P composite, (b) cross section of ten-layer C/C composite

In the last decade, effective media theories, widely used in classical continuum micromechanics, have been recognized as an attractive alternative to FEM-based methods. This approach was pioneered by Gommers et al. (1998) and Huysmans et al. (1998), who modeled knitted composites as assembly of circular fibers in an isotropic matrix and used the Mori-Tanaka method (MT) (Mori and Tanaka, 1973) to evaluate the overall mechanical response, and recently generalized by Barbero et al. (2005) in the framework of the theory of periodic eigenstrains employing an idealized three-dimensional geometrical model. All these studies report good correspondence with experimental data with an error comparable to an experimental scatter. Moreover, the MT-based approaches presented in (Gommers et al., 1998; Huysmans et al., 1998) allow us to easily incorporate imperfections in the tow path, typically introduced in terms of histograms of the distribution of inclination angles (Skoček et al., 2008; Vopička, 2004), as they rely on the orientation averaging techniques. This is a definite advantage of an approximate MT model when compared to a rigorous approach of Barbero et al. (2005), which relies on a well-defined geometry.

In this regard, the MT procedure introduced by Hatta and Taya (1986) for thermal conductivity and by Jeong et al. (1998) for electrical conductivity is utilized to determine the effective thermal coefficients for C/C composites on the micro- and meso-scale. A similar approach is used to determine effective stiffness matrices. On both scales a two step homogenization approach is adopted. It combines evaluation of effective properties in the absence of pores with a subsequent homogenization step in which the porous phase is introduced into

a new homogenized matrix.

To taken into account an inherent layered characteristic of C/C composites the laminate theory introduced by Milton (2002) is employed for elastic properties on the macro-scale and the simple rules of mixture are used to obtain the demanded thermal conductivities (Section 4.4).

A numerical application of effective properties of composite materials is briefly demonstrated at the end of this thesis. Experimental data of Strain Hardening Cement-based Composites (SHCC) are utilized to define the numerical model based on rotating cracks. The suitability of a designed model is proved by confrontation of the numerical results with the experimental data, see Appendix C.

1.2 Carbon-Carbon composites

Carbon-Carbon (C/C) composites (also denoted as a carbon fiber reinforced carbon (CRFC)) present a well-established and attractive material variant used in numerous branches of engineering design with applications ranging from rehabilitation and repair of concrete and masonry structures to design of biocompatible medical implants. In comparison with traditional materials, composites offer higher strength, light weight, non-corrosive properties, dimensional stability, good conformability and possibility of performance-based design. Nowadays, an increasing number of fiber reinforced composite components are being fabricated with load-carrying fibers, which are woven to form a fabric. This reinforcement system has advantages with respect to fabrication as well as mechanical properties. The weaving and interlacing of the fiber tows produces a self-supporting system that can be manipulated to form complex shapes. In terms of mechanical performance, the geometry of a fabric provides bi-directional stiffness for in-plane of loading, increased interlaminar stiffness for out-of-plane loading and superior impact tolerance and wear resistance. A lucid discussion of these aspects can be found, e.g., in (Cox and Flanagan, 1997). From these material systems, Carbon-Carbon woven composites present the most progressive and versatile material combination allowing their use in structural, mechanical and aerospace engineering as well as biomedical applications thanks to their biocompatibility with a soft tissue.

Although woven composites are frequently used in practice, an accurate and reliable

thermomechanical analysis of these material systems still presents a non-trivial challenge due to their complex geometry displayed at several length scales. This is especially true for C/C composites, where such a feature directly follows from the manufacturing process which includes transition from Carbon-Polymer (C/P) composite to C/C through pyrolysis of polymeric precursor (Chow and Ko, 1989). This is documented in Fig. 1.2, showing an example of a balanced plain weave composite displaying various geometrical imperfections on several length scales. With this case in mind, we can conclude that in order to provide a reliable and accurate description of the material, the following aspects need to be taken into account:

- yarn waviness and misalignment of individual tows,
- high porosity of C/C woven composite,
- non-linear behavior of matrix and tows including their interface,
- realistic geometry description based on image analysis of in-situ observed microstructures.

Each of these topics is briefly covered below.

1.2.1 Tow path imperfections

Although a majority of approaches to the modeling of overall behavior of woven composites rely on a well-defined regular geometry (Cox and Flanagan, 1997; Chung and Tamma, 1999), a careful examination of morphology of real materials reveals substantial departure from such an idealization. To keep the discussion on a concrete level, consider an example of the plane view of a C/P composite shown in Fig. 1.2(a), clearly demonstrating a (quasi-) periodic character of the geometrical arrangement of fiber tows. Apart from that the figure also suggests various geometrical imperfections attributed to the manufacturing processes. These are mainly influenced by two technologies (Pastore, 1993):

- textile (woven fabric preparation),

- composite (impregnation of fabric reinforcement by matrix precursor, pressing and heat treatment).

Although it is generally accepted that such a class of imperfections to a large extent influences the overall behavior of the composite, this problem has been mainly addressed in the literature in the form of numerical parametric studies trying to asses the influence of typical imperfections observed in experiments (Whitcomb and Tang, 2001; Lomov et al., 2003). An alternative approach to this problem, employing basic principles of quantification of geometry of random media, has been proposed in (Zeman, 2003; Zeman and Šejnoha, 2004a; Skoček et al., 2006). Here, the actual complicated microstructure is optimally fitted by a simplified geometrical model of (Kuhn and Charalambides, 1999) in terms of the two-point probability function and/or the lineal path function. This allows a substantial reduction in the problem complexity while capturing the most important characteristics of in-situ observed microstructures.

Even though the characterization of the disordered microstructure of a woven composite based on a statistically optimized model presents a flexible tool of incorporating tow path imperfections, it may prove to be rather expensive, especially in the cases when a quick estimation of the linear behavior is on demand. In this connection, well-established effective media theories (Torquato, 2002), when supplied with a proper microstructural characterization, provide an interesting alternative to FEM-based simulations.

Procedures for acquisition of relevant data can be found, e.g. in the work of Vopička (2004), where an image analysis of composite micrographs was used to get the frequency spectrum of the Fourier series to describe the yarn shape in both woven and braided fabrics. In particular, it has been demonstrated that the crimp waveform is subjected to deformation when pressed during the manufacturing process and the frequency spectrum is therefore distorted compared to that of the unprocessed (free) fabric. Deformation of reinforcements can be described by histograms of yarn angles with respect to the textile fabric plane. These data can be utilized, e.g., as an input into the Mori-Tanaka method to determine the effective behavior of a composite. This approach has been pioneered by Gommers et al. (1998) for modeling of knitted composites, see also (Skoček et al., 2006) for the generalization to imperfect woven composites.

1.2.2 Porosity

Although the tow path imperfections present one of important sources of uncertainties to the analysis, it is by no means the only one. This is again nicely illustrated in Fig. 1.2(b), showing a very high intrinsic porosity of the composite as a result of curing and/or pyrolysis of polymeric precursor. Note that porosity of this class of materials could actually be a desirable feature as it contributes to a compatibility between the bulk material and a soft tissue in biomedical applications (Pešáková et al., 2003).

The structure of voids is complex and difficult to describe. Voids may be characterized in various ways, e.g. according to their size (macro-, meso-, micro- or nanopores), their position in composite structure (transverse cracks, delamination cracks, crimp voids, matrix pores etc.) or their shape (rod-like shape, thin plates, rough branch structures) (Yurgartis et al., 1992). In any case the proper knowledge of voids' shape, size and distribution is important for both controlling the porosity due to manufacturing as well as formulation of the structural models for prediction of final composite properties. This was clearly demonstrated in the thesis of (Palán, 2002), which compares results of detailed finite element studies of overall thermal properties of C/C composite and experimental data. In this case, the theoretical predictions, based on ideal pore-free structure, differ from measured data almost by an order of magnitude.

Quite surprisingly, assessment of the impact of high porosity on the overall behavior of textile composites has acquired relatively little attention in the literature and has been mainly focused on experimental characterization. Examples of studies of this phenomena include, e.g., quantification of influence of pressure on pore characteristics (Oh et al., 1999), assessment of interlaminar strength (Casal et al., 2001) and oxidation resistance (Liao et al., 2002). In the field of numerical modeling, the only study we are aware of is due to (Kuhn and Charalambides, 1998), who nevertheless considered a highly idealized geometry of the porous space. Therefore, this research topic offers a great potential, both in the framework of detailed numerical models as well as for simplified models based on continuum micromechanics.

1.2.3 Material models

In addition to detailed characterization of geometry of a composite, material properties of individual components are an equally important input to the analysis. However, this step is far from being trivial for C/C composites, where each phase undergoes a very complex thermal treatment influencing its intrinsic behavior. Therefore, similar to previously discussed topics, the material parameters should be obtained on the basis of in-situ measurements rather than from an independent tests. Recognizing that the typical size of fibers is of the order of micrometers, this requirement rules out most traditional experimental procedures.

The depth-sensing nanoindentation, based on indenting the surface of a material by a very small diamond tip, is a modern experimental technique ideally suited to examination of intrinsic material properties (such as Young's modulus, hardness, fracture energy) on the pertinent lengthscale (Fischer-Cripps, 2004). Initially developed for analysis of metals, it has been later intensively used for analysis of heterogeneous materials; see, e.g. (Nowicki and Susla, 2003) for a more detailed discussion. This technique is also readily applicable to experimental treatment of C/C material systems as demonstrated by a number of studies available in open literature (Marx and Riester, 1999; Diss et al., 2002a; Ozcan and Filip, 2005, and references therein) dealing mainly with materials for high-temperature applications.

Although the previously mentioned works present an impressive amount of experimental effort, the interpretation of results is typically based on load-displacement curves and on the assumptions of material's isotropy and elasticity. However, this methodology is rather questionable for the present material system, mainly due to anisotropy of individual phases and their mutual interaction (Gregory and Spearing, 2005). A more realistic approach requires a mixed numerical-experimental approach, consisting of a detailed numerical model (based on, e.g., the finite element method (Mackerle, 2004)) and an appropriate inverse identification procedure that enables us to asses parameters of the model (Sol et al., 1997). A more refined inelastic simulation also allows us to incorporate additional data to force-displacement curve, such as the tip imprint on a surface, into the identification procedure. This substantially increases the reliability of identification procedure and representativeness of material parameters (Fischer-Cripps, 2004).

1.2.4 Image analysis

As indirectly discussed in all previous topics, image processing and comprehensive geometry description provides a stepping stone for a reliable numerical analysis and vice-versa. In this regard, automated image analysis procedures based on a high-resolution microstructural images become a necessity for a successful completion of the proposed study. A more detailed description of methods employed in image analysis can be found in the theses by Vopička (2004) and Tomková (2006). For the sake of illustration we present a representative result in Fig. 1.3.

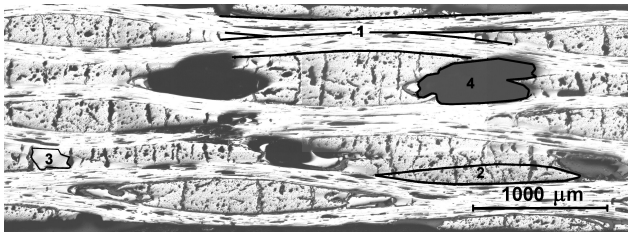

Figure 1.3: Basic structural components of woven C/C composite. (1-parallel cuts of carbon tows, 2-cross-section cuts of carbon tows, 3-carbon matrix, 4-voids. Resolution is 1.7 μm/pixel)

Finally note that, in a broader sense, the ultimate goal of any composite-based research is a formulation of a multi-scale based model incorporating non-linear behavior. Note that this topic is not explicitly covered in the proposed study. Moreover, as demonstrated in detail in the work of Wierer (2005), numerical homogenization of non-linear behavior is extremely ill-conditioned problem due to complex geometry of the composite. This deserves a special treatment, which is out of the scope of the presented research.

1.2.5 Length scales

In micromechanical approaches the heat flux (stress) and temperature gradient (strain) in an inhomogeneous material are splitted into contributions corresponding to different length scales. It is assume that these length scales are sufficiently different (Böhm, 2007). Therefore, for each pair of them the following statements have to be validated:

- fluctuation of the heat flux and temperature gradient fields at the lower level influence

the macroscopic behavior at the higher level only in the sense of the volume averages,

- gradients of the heat flux field and laplace operator of temperature field at the larger length scale are not significant at the smaller one, where the fields appear to be locally constant and can be described in the forms of uniform "applied" or "far field" loading.

The splitting form for temperature gradient

$$\mathbf{h}(\mathbf{x}) = \nabla T(\mathbf{x}) = \left\{ \frac{\partial T}{\partial x_1}; \frac{\partial T}{\partial x_2}; \frac{\partial T}{\partial x_3} \right\}^{\mathsf{T}}, \tag{1.1}$$

$$\mathbf{q}(\mathbf{x}) = -\boldsymbol{\chi}(\mathbf{x})\,\mathbf{h}(\mathbf{x}) \tag{1.2}$$

and heat flux, respectively, into the described contributions is written as

$$\mathbf{h}(\mathbf{x}) = \langle \mathbf{h} \rangle + \mathbf{h}^{\mathsf{f}}(\mathbf{x}) \quad \text{and} \quad \mathbf{q}(\mathbf{x}) = \langle \mathbf{q} \rangle + \mathbf{q}^{\mathsf{f}}(\mathbf{x}), \tag{1.3}$$

where $\langle \mathbf{h} \rangle$ and $\langle \mathbf{q} \rangle$ stand for the macroscopic fields (the volumetric averages) while the $\mathbf{h}^{\mathsf{f}}$ and $\mathbf{q}^{\mathsf{f}}$ denote the microscopic fluctuations, $\boldsymbol{\chi}(\mathbf{x})$ refers to the corresponding local conductivity matrix $\left[\mathrm{Wm^{-1}K^{-1}}\right]$. Similar relation can be written for the elasticity problem by substituting corresponding variables.

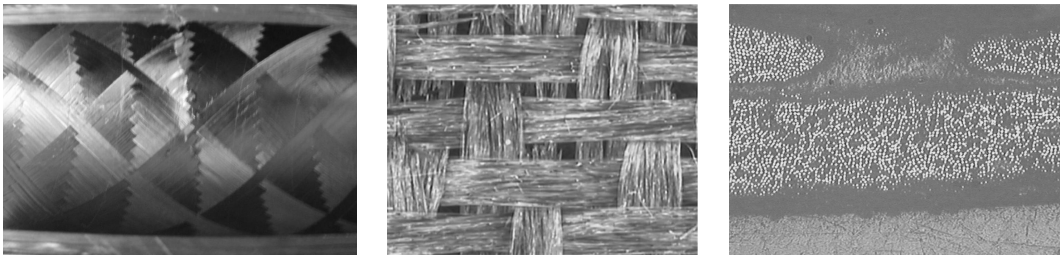

(a) (b) (c)

Figure 1.4: Multi-scale: (a) Macro-scale, (b) meso-scale, (c) micro-scale

In C/C plain weave composites at least three length scales that can be described by continuum mechanics are recognized:

- macro-scale (sample, component, etc.), Fig. 1.4(a),
- meso-scale (individual plies), Fig. 1.4(b),
- micro-scale (tow = fiber-matrix-void interaction), Fig. 1.4(c).

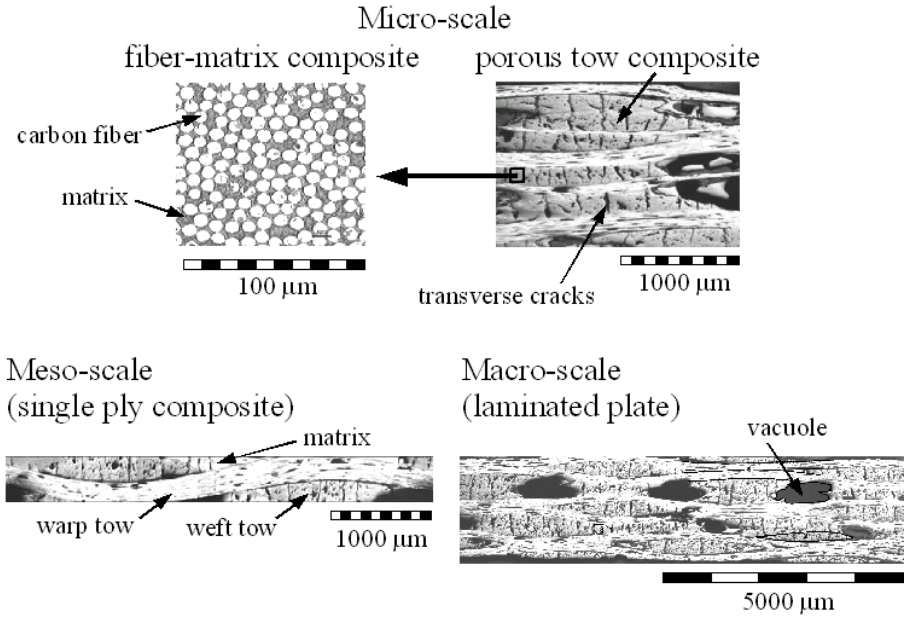

Figure 1.5: Grayscale images of a real composite system identifying individual scales

In the presented work, all the computational approaches are referred to these scales. The comparison of individual scales and a terminology use are represented in Fig. 1.5.

Chapter 2

CONCEPTUAL AND METHODICAL APPROACHES

Recall that in this study, the emphasis is put on a reliable modeling and characterization of multi-phase C/C composite materials. Basic homogenization procedures are listed below. Some of them can be used for micromechanically based constitutive material models at higher length scales. The overall thermomechanical response of homogenized materials is ordinarily based on the interaction of the constituents. Therefore, in some cases a simple description of material parameters change is not sufficient enough to give true picture of the material behavior and the functional relationships in the constitutive law have to be adapted as well (Böhm, 2007).

Due to the variations of the microfields caused by phase distribution in adequate volume elements the computational effort is enormous for most of the material structures. Therefore, some approximations are needed. For convenience, the majority of the modeling approaches can be sorted into two groups:

- Methods based on statistical information (Mean field approaches, Variational bounding methods).

- Methods studying discrete microstructure (Periodic microfield approaches, Embedded cell or Embedding approaches, Window Approaches, etc.).

Some of the commonly used methods are mentioned and described in the following text. Owing to the proposed research of the C/C composites, the main emphasis is put on the mean field and the periodic microfield approaches.

For the sake of simplicity the description of homogenization techniques is provided for the heat conduction problem. Extension to the elasticity problem can be obtained by an adequate substitution of inherent variables.

2.1 Methods based on statistical information

2.1.1 Mean field approaches (MFAs)

The microfields inside each constituent are approximated by their volume averages ($\langle \mathbf{h}_r \rangle, \langle \mathbf{q}_r \rangle$). These methods usually use information about the microscopic topology, the inclusion shape and a orientation. The localization relations then take the forms

$$\begin{aligned} \langle \mathbf{h}_r \rangle &= \boldsymbol{A}_r \langle \mathbf{h} \rangle , \\ \langle \mathbf{q}_r \rangle &= \boldsymbol{B}_r \langle \mathbf{q} \rangle , \end{aligned} \tag{2.1}$$

and the homogenization relations become

$$\langle \mathbf{h}_r \rangle = \frac{1}{\Omega_r} \int_{\Omega_r} \mathbf{h}(\mathbf{x}) \, \mathrm{d}\Omega \quad \text{with} \quad \langle \mathbf{h} \rangle = \sum_{r=1}^{N} c_r \langle \mathbf{h}_r \rangle , \tag{2.2}$$

$$\langle \mathbf{q}_r \rangle = \frac{1}{\Omega_r} \int_{\Omega_r} \mathbf{q}(\mathbf{x}) \, \mathrm{d}\Omega \quad \text{with} \quad \langle \mathbf{q} \rangle = \sum_{r=1}^{N} c_r \langle \mathbf{q}_r \rangle , \tag{2.3}$$

where index $r = 1, \ldots, N$ refers to individual constituents (in the following text index 1 is reserved for the matrix phase), Ω_r stands for the phase volumes and $c_r = \Omega_r / \sum_i \Omega_i$ is the corresponding volume fraction. The matrices $\boldsymbol{A}_r$ and $\boldsymbol{B}_r$ are termed the concentration factors (Benveniste et al., 1990; Jeong et al., 1998) for the heterogeneity. The concentration tensors relevant for thermal conduction problems are the gradient concentration tensors and the flux concentration tensors.

Here we address the problem for the evaluation of overall thermal conduction tensor $\boldsymbol{\chi}$ (Eq. (2.4)) of a C/C composites where many inhomogeneities are embedded in a matrix material. Three approximate methods are now available in literature, which are worthwhile mentioning:

- the dilute approximation (Fig. 2.1(a)),
- the self-consistent method (Fig. 2.1(b)),
- the Mori-Tanaka method (Fig. 2.1(c)).

Before contemplation with individual methods we mention some general relations for the following treatment. The overall flux-gradient relation has the form

$$\langle \mathbf{q} \rangle = \boldsymbol{\chi} \langle \mathbf{h} \rangle . \tag{2.4}$$

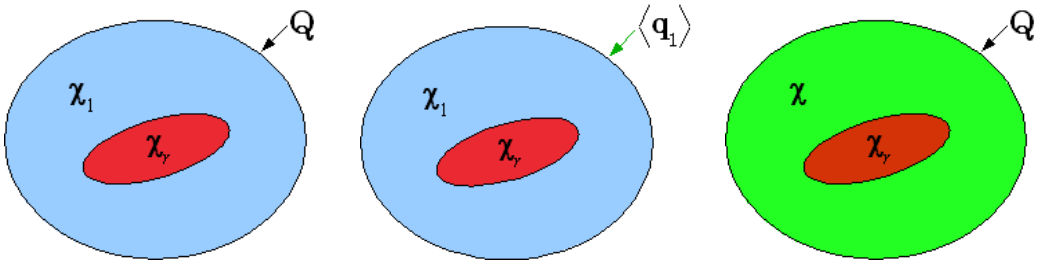

(a) (b) (c)

Figure 2.1: Mean field approaches: (a) The dilute approximation, (b) the self-consistent method, (c) the Mori-Tanaka method

Similarly, for each phase we write

$$\langle \mathbf{q}_r \rangle = \boldsymbol{\chi}_r \langle \mathbf{h}_r \rangle , \tag{2.5}$$

where $\boldsymbol{\chi}_r$ is the phase conductivity tensor.

From the definition of volume averaging (Eq. (2.2)) the following relations are obtained

$$\begin{aligned} \langle \mathbf{h} \rangle &= \sum_{r=1}^{N} c_r \langle \mathbf{h}_r \rangle = \mathbf{H}, \\ \langle \mathbf{q} \rangle &= \sum_{r=1}^{N} c_r \langle \mathbf{q}_r \rangle = \mathbf{Q}, \end{aligned} \tag{2.6}$$

where vectors $\mathbf{H}$ and $\mathbf{Q}$ are prescribed macroscopically uniform temperature gradient and flux, respectively. In the isothermal case volume averages are equal to the corresponding homogenous boundary conditions. Combining Eqs. (2.1) and (2.6) further gives

$$\sum_{r=1}^{N} c_r \boldsymbol{A}_r = \boldsymbol{I}, \tag{2.7}$$

where $\boldsymbol{I}$ expresses the identity matrix. By introducing homogenization relations for the whole volume (Ω_s)

$$\begin{aligned} \langle \mathbf{h} \rangle &= \frac{1}{\Omega_s} \int_{\Omega_s} \mathbf{h}(\mathbf{x}) \, \mathrm{d}\Omega, \\ \langle \mathbf{q} \rangle &= \frac{1}{\Omega_s} \int_{\Omega_s} \mathbf{q}(\mathbf{x}) \, \mathrm{d}\Omega, \end{aligned} \tag{2.8}$$

and employing Eq. (2.4) gives the effective conductivity tensor in the form

$$\boldsymbol{\chi} = \sum_{r=1}^{N} c_r \boldsymbol{\chi}_r \boldsymbol{A}_r. \tag{2.9}$$

Note that Eqs. (1.3) and (2.8) imply that the fluctuations vanish for sufficiently large integration volume

$$\frac{1}{\Omega_s}\int_{\Omega_s}\mathbf{h}^{\mathrm{f}}(\mathbf{x})\,\mathrm{d}\Omega = 0. \tag{2.10}$$

2.1.1.1 Eshelby and ellipsoidal inclusion problems

Most of the useful theories of composite materials depend one way or the other on the solution of the ellipsoidal inclusion problem. The problem was addressed by Eshelby (1957). He proved that the local stress and strain fields in a ellipsoidal inhomogeneity embedded into a different infinite homogenous elastic material that is loaded by remotely applied uniform stress or strain fields, respectively, are also uniform. This result has then provided a stepping stone for the evaluation of effective properties in a variety of composites systems.

Solution of the Eshelby problem for thermal conductivity relies on a certain transformation problem. In particular, consider a homogenous infinite anisotropic material, which contains an ellipsoidal inclusion of the same material. The surrounding material is neither constrained nor loaded. Suppose that the inclusion is now loaded by a certain transformation uniform temperature gradient $(\mathbf{h}^*)$. If free, it would undergo homogenous temperature change, but due to constraint of the matrix it attains in situ temperature gradient

$$\mathbf{h}_r = \boldsymbol{S}\mathbf{h}^*, \tag{2.11}$$

where the second-order tensor $\boldsymbol{S}$ is analogous to the Eshelby tensor for elasticity, see Appendix A. Note that the Eshelby tensor for generic anisotropic material is not known in an explicit form. Therefore, the numerical integration (e.g. Gauss quadrature) has to be employed in such a case (Gavazzi and Lagoudas, 1990).

When the Eshelby tensor is known and the heat flux and temperature gradient fields in inhomogeneous inclusions embedded in a matrix are of interest (for the mean field theories), the concept of equivalent homogeneous inclusions have to be employed. This strategy involves replacing an actual perfectly bonded inhomogeneous inclusion, which has different material properties than the matrix and which is subjected to a given unconstrained transformation temperature gradient, with an equivalent homogenous inclusion loaded by an appropriate equivalent transformation temperature gradient $\mathbf{h}^*$. This equivalent transformation gradient has to be chosen in such a way that the same flux and gradient fields are obtained in

the constrained state for the actual inhomogeneous inclusion and the equivalent homogenous inclusion.

2.1.1.2 Dilute approximation

Consider a matrix-based (index 1) composite consisting of N phases. When using the dilute approximation we assume that there is no interaction between inclusions $r = 2, \ldots, N$. This means that the concentration factor of each phase can be evaluated as if a single inclusion of each phase was embedded in a infinite volume of matrix.

Let this composite be subjected on its outside boundary Γ_s to a homogeneous temperature boundary condition defined in global coordinate system $\mathbf{X}$ as (Benveniste et al., 1990; Hatta and Taya, 1986)

$$T(\mathbf{X}) = \mathbf{H}^{\mathsf{T}}\mathbf{X} \qquad \text{on } \Gamma_s. \tag{2.12}$$

The local temperature gradient of a single inclusion in a large volume of matrix loaded by $\mathbf{H}$ assumes according Eq. (2.1) that

$$\langle \mathbf{h}_r \rangle = \boldsymbol{A}_r^{\mathsf{dil}} \mathbf{H}. \tag{2.13}$$

The local temperature gradient in the inclusion can be decomposed as

$$\langle \mathbf{h}_r \rangle = \mathbf{H} + \boldsymbol{S}\mathbf{h}^*. \tag{2.14}$$

The local heat flux (Eq. (2.5)) for the heterogeneity and equivalent inclusion is given by

$$\langle \mathbf{q}_r \rangle = -\boldsymbol{\chi}_r \langle \mathbf{h}_r \rangle = -\boldsymbol{\chi}_1 \left(\langle \mathbf{h}_r \rangle - \mathbf{h}^* \right), \tag{2.15}$$

so that

$$\mathbf{h}^* = (\boldsymbol{\chi}_1)^{-1} (\boldsymbol{\chi}_1 - \boldsymbol{\chi}_r) \langle \mathbf{h}_r \rangle . \tag{2.16}$$

Next, substitute Eq. (2.16) into Eq. (2.14) to get

$$\langle \mathbf{h}_r \rangle = \mathbf{H} + \boldsymbol{S}(\boldsymbol{\chi}_1)^{-1} (\boldsymbol{\chi}_1 - \boldsymbol{\chi}_r) \langle \mathbf{h}_r \rangle , \tag{2.17}$$

and finally

$$\langle \mathbf{h}_r \rangle = \left[\boldsymbol{I} - \boldsymbol{S}(\boldsymbol{\chi}_1)^{-1} (\boldsymbol{\chi}_1 - \boldsymbol{\chi}_r) \right]^{-1} \mathbf{H}. \tag{2.18}$$

Comparing Eqs. (2.13) and (2.18) yields the concentration factor as

$$\boldsymbol{A}_r^{\mathsf{dil}} = \left[\boldsymbol{I} - \boldsymbol{S}(\boldsymbol{\chi}_1)^{-1} (\boldsymbol{\chi}_1 - \boldsymbol{\chi}_r) \right]^{-1} . \tag{2.19}$$

Finally, the desired effective thermal conductivity matrix is derived from Eqs. (2.3) and (2.19)

$$\boldsymbol{\chi}^{\mathsf{dil}} = \boldsymbol{\chi}_1 + \sum_{r=2}^{N} c_r \left(\boldsymbol{\chi}_r - \boldsymbol{\chi}_1\right) \boldsymbol{A}_r^{\mathsf{dil}}. \tag{2.20}$$

2.1.1.3 Self-consistent method

Another group of estimates for the overall thermomechanical behavior of inhomogeneous materials are self-consistent schemes, in which an inclusion or some phase arrangement is embedded in the effective material (the properties of which are not known a priori). Actually, it assumes that interactions of phases is accounted for by this assumption.

A similar procedure as for the dilute method is used herein and so the self-consistent scheme can be formally described by the relation

$$\boldsymbol{\chi}^{\mathsf{SC}} = \boldsymbol{\chi}_1 + \sum_{r=2}^{N} c_r \left(\boldsymbol{\chi}_r - \boldsymbol{\chi}_1\right) \boldsymbol{A}_r^{\mathsf{dil},*}, \tag{2.21}$$

where $\boldsymbol{A}_r^{\mathsf{dil},*}$ is the concentration factor for a inclusion embedded in the effective medium in analogy to Eq. (2.19) and is a function of $\boldsymbol{\chi}^{\mathsf{SC}}$. Therefore, Eq. (2.21) represents an implicit solution and an iterative scheme has to be used

$$\boldsymbol{\chi}_{n+1}^{\mathsf{SC}} = \boldsymbol{\chi}_1 + \sum_{r=2}^{N} c_r \left(\boldsymbol{\chi}_r - \boldsymbol{\chi}_1\right) \left[\boldsymbol{I} - \boldsymbol{S}_n (\boldsymbol{\chi}_n^{\mathsf{SC}})^{-1} \left(\boldsymbol{\chi}_n^{\mathsf{SC}} - \boldsymbol{\chi}_r\right)\right]^{-1}. \tag{2.22}$$

The mentioned tensor $\boldsymbol{S}_n$ pertains to a given inclusion enclosed in the n-th iteration by the resulting effective conductivity and has to be computed for each iteration.

2.1.1.4 Mori-Tanaka method

The last method, mentioned in this section is the procedure proposed by Mori and Tanaka (1973). There an interaction between the inclusions is accounted for by assuming that the flux in each phase is equal to that of a single inclusion embedded into an unbounded matrix subjected to as yet unknown average temperature gradient ($\langle \mathbf{h}_1 \rangle$) or flux ($\langle \mathbf{q}_1 \rangle$) in the matrix, see e.g. (Benveniste, 1987; Benveniste et al., 1990, for further details) .

Let us consider an N-phase composite medium with the heterogeneities (reinforcements or voids). This composite is subjected on its outside boundary to a homogeneous temperature boundary condition defined as (Benveniste et al., 1990; Tomková et al., 2008), Eq. (2.12).

Next, in the context of the Mori-Tanaka method, consider a certain auxiliary transformation problem where a single heterogeneity in an infinite matrix is replaced by an equivalent inclusion of the same shape and orientation but having the material properties of the matrix phase. The local temperature gradient in the inclusion is then associated with the gradient in matrix phase through the concentration factor $\boldsymbol{A}_r^{\mathsf{dil}}$ (sometimes called as partial concentration factor for these procedure), see derivation of Eq. (2.19)

$$\langle \mathbf{h}_r \rangle = \boldsymbol{A}_r^{\mathsf{dil}} \langle \mathbf{h}_1 \rangle . \tag{2.23}$$

In the Mori-Tanaka mean field theory the mutual interaction of individual heterogeneities is taken into account as mentioned above. Therefore, assume that the local temperature gradient $\mathbf{h}_r$ is expressed in terms of the prescribed macroscopically uniform temperature gradient $\mathbf{H}$ as

$$\langle \mathbf{h}_r \rangle = \boldsymbol{A}_r^{\mathsf{MT}} \mathbf{H}, \tag{2.24}$$

where the matrix $\boldsymbol{A}_r^{\mathsf{MT}}$ is again termed the concentration factor (Benveniste et al., 1990; Jeong et al., 1998) for the heterogeneity.

Substitution of Eq. (2.23) into Eq. (2.2) and then into Eq. (2.24) leads to the relation for the concentration factor

$$\boldsymbol{A}_r^{\mathsf{MT}} = \boldsymbol{A}_r^{\mathsf{dil}} \left[c_1 \boldsymbol{I} + \sum_{i=2}^{N} c_i \boldsymbol{A}_i^{\mathsf{dil}} \right]^{-1} . \tag{2.25}$$

which, together with Eq. (2.3) gives

$$\boldsymbol{\chi}^{\mathsf{MT}} = \boldsymbol{\chi}_1 + \sum_{r=2}^{N} c_r \left(\boldsymbol{\chi}_r - \boldsymbol{\chi}_1 \right) \boldsymbol{A}_r^{\mathsf{MT}}. \tag{2.26}$$

Keep in mind that above mentioned list of mean field approaches do not cover all of the known methods, see (Böhm, 2007) for more details.

2.1.2 Variational bounding methods (VBMs)

A brief description of this metod is mentioned hereafter, a more interested reader is referred to the work of Böhm (2007). Variational principles are used to obtain upper and lower bounds on the overall thermal conductivity as well as other physical properties of inhomogeneous materials. Many analytical bounds are obtained on the basis of phase-wise constant

flux (polarization) fields. Bounds can be used for assessing other models of inhomogeneous materials. Furthermore, in many cases one of the bounds provides good estimates for the physical property under consideration, even if the bounds are rather slack. Many bounding methods are closely related to MFAs. It is noteworthy that VBMs are limited to homogenization and can not be used for localization task.

To get the variational bounds on effective properties, one must first express the effective parameter in terms of some functional (e.g. energy functional) and then formulate an appropriate variational principle for the functional. Once the variational principle is established then specific bounds on the property of interest are obtained by constructing trial or admissible fields that conform with the variational principle (Torquato, 2002).

The bounds are useful because:

- they rigorously incorporate nontrivial information about the microstructure via statistical correlation functions and consequently serve as a guide in identifying appropriate statistical descriptors,
- as successively more microstructural information is included, the bounds become progressively narrowed,
- one of the bounds can provide a relatively sharp estimate of the property for a wide range of conditions, even when the reciprocal bound diverges from it,
- they are usually exact under certain conditions,
- they can be utilized to test the merits of a theory or computer experiment,
- they provide a unified framework to study a variety of different effective properties.

Many definitions of the bounds can be found in literature . They can be sorted in accordance with Böhm (2007) into these groups:

- classical bounds - Hill bounds, Hashin-Strinkman-type bounds,..., see (Cherkaev, 2000, and references therein)
- improved bounds, see (Torquato, 2002),

- bounds for nonlinear behavior, see (Castañeda, 1992).

2.2 Methods studying discrete microstructure

Micromechanical approaches based on the discrete microstructure are used for the capability of studying general microstructure of materials and describing the diversity of temperature field at the scale of inhomogeneities. This can be a goal of treatment when the understanding of a material behavior is desired or the fluctuations in the local temperature are considerable and can not be grasp by average fields.

For the simply periodic materials, in which the microstructure exhibits strong periodicity, the generation of microgeometry can be reached for instance by a hexagonal or cubic arrangement of the inhomogeneities (Fig. 2.2(a,b)). If more complex (quasi-periodic) microstructure of material is investigated (Fig. 2.2(c)), more sophisticated arrangement of the inhomogeneities has to be involved. In this case the generation of the unit cell is proposed on the basis of real structure or with the help of computational algorithm. The former approach stands on the analysis of digital images of the real material structure and the selection of appropriate representative volume. The second group of structure's reconstruction comes out of the computer generated microgeometries - based on generic random arrangements of a small to a fair number of inhomogeneities or approximation of some given phase distribution statistics, see (Zeman, 2003).

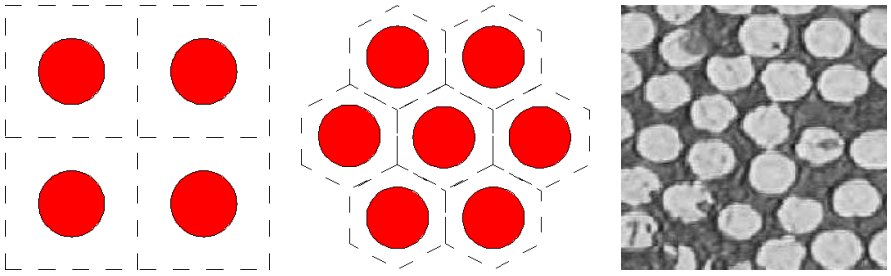

(a) (b) (c)

Figure 2.2: Microstructure: (a) Cubic arrangement, (b) hexagonal arrangement, (c) real (quasi-periodic) structure

For both the computer generated phase arrangements and real structure models there is a need of a geometrical complexity which is required for adequately representing the physical

behavior of the inhomogeneous material to be studied. Therefore, the suitable representative volume element (RVE) has to be chosen. The size can be determined in accordance with (Zeman and Šejnoha, 2001) where the size is governed by a requirement of two statistically independent inhomogeneities or utilizing the correlation length (Zeman and Šejnoha, 2007). On the other hand, the element size is possible to determine by employing the error between some physical properties (Gajdošík, 2005).

2.2.1 Periodic microfield approaches (PMAs)

Periodic microfield approaches (unit cell models) simulate the behavior of a real inhomogeneous material through the modeling of a unit cell which presents a periodic phase arrangement. The response of this system can be obtained by the analysis of such a unit cell with periodic boundary conditions. It is convenient for engineering problems involving two or more length scales where the higher scales is made up of repeating periodic unit cells (PUCs). They have become very popular in recent years to compute the linear and non-linear responses of composite materials as the unit cell behavior is easily determined through the finite element analysis (Sýkora et al., 2009; Vorel et al., 2006).

The key step of the definition of the optimal periodic unit cell is a choice of proper description of heterogeneous materials with random structure. The useable statistical descriptors can be found in (Torquato, 2002), e.g. the application of one- and two-point probability functions is presented in the work by Skoček et al. (2006) and Zeman (2003), see Section 4.1 as well.

In typical periodic microfield approaches the temperature gradient and heat flux are split into constant macroscopic contributions and periodically varying microscopic fluctuations, compare with Eq. (1.3). One can consider the linear variation of the local temperature $T(\mathbf{X})$ written in terms of the uniform macroscopic quantity $\mathbf{H}$ as

$$T(\mathbf{X}) = \mathbf{H}\mathbf{X} + T^{\mathrm{f}}(\mathbf{X}), \tag{2.27}$$

where T^{f} is periodic temperature fluctuation and $\bullet(\mathbf{X})$ is introduced to represent a given quantity in the global coordinate system $\mathbf{X}$. The local microscopic constitutive equation written in the local coordinate system $\mathbf{x}$ takes the form presented in Eq. (1.2). To complete the set of equations needed in the derivation of effective properties we recall the Fourier

inequality (Malvern, 1969) (the Hill lemma for mechanical problem) for an equivalent representation of steady state heat conduction problem together with Eq. (1.2) and write the global-local variational principles, see e.g. (Tomková et al., 2008; Šejnoha and Zeman, 2008, for further details) in the forms

$$\left\langle \delta\mathbf{h}(\mathbf{x})^{\mathsf{T}}\boldsymbol{\chi}(\mathbf{x})\mathbf{h}(\mathbf{x})\right\rangle = 0. \tag{2.28}$$

(If the PUCs are arranged into the large structure element, each of them contributes with the same temperature change along the same direction.) In the framework of finite element approximation the discrete form of local gradients derived from Eq. (2.27) reads

$$\mathbf{h}(\mathbf{X}) = \mathbf{H} + \boldsymbol{B}(\mathbf{X})\mathbf{T}_d^f, \tag{2.29}$$

where $\boldsymbol{B}$ stores the derivatives of the element shape functions with respect to $\mathbf{X}$ and $\mathbf{T}_d^f$ is the vector of the fluctuation parts of nodal temperatures. Substituting Eq. (2.29) into Eq. (2.28) gives

$$\left(\delta\mathbf{T}_d^f\right)^{\mathsf{T}}\left\langle \boldsymbol{B}(\mathbf{X})^{\mathsf{T}}\boldsymbol{\chi}(\mathbf{X})\boldsymbol{B}(\mathbf{X})\right\rangle \mathbf{T}_d^f = -\left(\delta\mathbf{T}_d^f\right)^{\mathsf{T}}\left\langle \boldsymbol{B}(\mathbf{X})^{\mathsf{T}}\boldsymbol{\chi}(\mathbf{X})\right\rangle \mathbf{H}, \tag{2.30}$$

to be solved for nodal temperatures $\mathbf{T}_d^f$. Combining Eqs. (2.29) and Eqs. (1.2) now allows us to write the volume averages of local heat fluxes as

$$\mathbf{Q} = \left\langle \boldsymbol{P}(\mathbf{X})^{\mathsf{T}}\mathbf{q}(\mathbf{x})\right\rangle = -\frac{1}{|\Omega|}\int_{\Omega}\boldsymbol{P}(\mathbf{X})^{\mathsf{T}}\boldsymbol{\chi}(\mathbf{x})\boldsymbol{P}(\mathbf{X})\mathbf{h}(\mathbf{X})\,\mathrm{d}\Omega, \tag{2.31}$$

also showing the relationship between material matrices in the local and global coordinate systems in terms of certain transformation matrix $\boldsymbol{P}$, see e.g. (Bittnar and Šejnoha, 1996; Zeman, 2003; Tomková et al., 2008; Vorel and Šejnoha, 2009),

$$\boldsymbol{\chi}(\mathbf{X}) = \boldsymbol{P}(\mathbf{X})^{\mathsf{T}}\boldsymbol{\chi}(\mathbf{x})\boldsymbol{P}(\mathbf{X}). \tag{2.32}$$

The result of Eq. (2.31) now allows for writing the macroscopic constitutive laws as

$$\mathbf{Q} = -\boldsymbol{\chi}^{\mathsf{H}}\mathbf{H}, \tag{2.33}$$

where $\boldsymbol{\chi}^{\mathsf{H}}$ is the searched homogenized effective thermal conductivity. In particular, for a three-dimensional PUC the components of the 3×3 conductivity matrix $\boldsymbol{\chi}^{\mathsf{H}}$ follow directly from the solution of three successive steady state heat conduction problems. To that end, the

periodic unit cell is loaded, in turn, by each of the three components of $\mathbf{H}$, while the other two vanish. The volume flux averages, Eq. (2.31), normalized with respect to $\mathbf{H}$ then furnish individual columns of $\boldsymbol{\chi}^{\mathsf{H}}$. The components of the 6×6 elastic stiffness matrix $\left[\mathsf{L}^{\mathsf{H}}\right]$ could be found analogously from the solution of six independent elasticity problems.

The effective thermal conductivities can been obtained assuming the solution derived in terms of the fluctuation part T^{f} of the local temperature T when loading an RVE directly by the prescribed macroscopic temperature gradient $(\mathbf{H})$ or by the macroscopic uniform heat flux $(\mathbf{Q})$ as mentioned above. The designer, however, must often rely on the use of standard finite element codes, either academic or commercial, where the loading is represented in terms of the prescribed boundary temperatures or fluxes and the solution is searched directly in terms of the local temperatures $T(\mathbf{X}), \mathbf{X} \in \Omega_s$.

For illustration, consider now the most simple case illustrated in Fig. 2.3, when the PUC is loaded by the uniform heat flux (Q_1) along the two vertical boundaries at $x_1 = 0, x_1 = d$ while no flow boundary conditions are specified $(Q_2 = 0)$ along the two horizontal boundaries at $x_2 = 0, x_2 = v$. Eq. (2.8) is then immediately satisfied and the horizontal component of the effective heat conductivity is, in view of Eq. (2.4), provided by

$$\chi_1 = -\frac{Q_1}{\langle h_1 \rangle}. \tag{2.34}$$

If no action is taken this result corresponds to the assumption of $T^{\mathsf{f}} = 0$ on boundary Γ_s. If, on the other hand, the periodic boundary conditions are on demand it is necessary to proceed as follows.

Consider again a two-dimensional rectangular RVE with dimensions u and v (see Fig. 2.3).

Observe that for a pair of points (e.g. A - master and a - slave) located on the opposite sides of the PUC the following relations hold

$$T_A = \langle h_2 \rangle \, x_{2,A} + T_A^{\mathsf{f}} + T(\mathbf{x}_0), \quad T_a = \langle h_1 \rangle \, u + \langle h_2 \rangle \, x_{2,a} + T_a^{\mathsf{f}} + T(\mathbf{x}_0), \tag{2.35}$$

Taking into account the fact that the fluctuation field of temperatures T^{f} satisfies the periodicity condition

$$T_a^{\mathsf{f}} = T_A^{\mathsf{f}}, \tag{2.36}$$

and subtracting corresponding terms on the opposite edges, we finally obtain (compare with

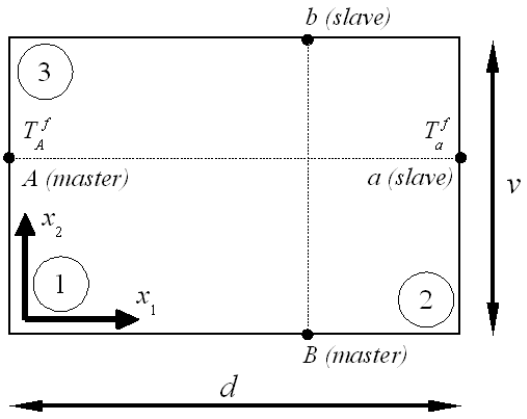

Figure 2.3: Conditions of periodicity

the work of Oezdemir et al. (2008))

$$\begin{aligned} \langle h_1 \rangle u &= T_a - T_A = T_2 - T_1, \\ \langle h_2 \rangle v &= T_b - T_B = T_3 - T_1, \end{aligned} \tag{2.37}$$

where T_1, T_2 and T_3 are the temperatures at the control points 1,2 and 3 seen in Fig. 2.3. These conditions can be introduced into most commercial software products using the multi-point constraint equations.

Note that neither the assumption of $T^{\mathrm{f}} = 0$ on Γ_s nor the periodic conditions (2.36) (or constraints (2.37)) are sufficient to specify the local temperature field uniquely. This condition is established by introducing a reference temperature $T(\mathbf{x}_0)$ at an arbitrary point $\mathbf{x}_0 \in \Gamma_s$ as indicated in Eq. (2.35).

In a linear case, when the effective thermal conductivities are independent of the actual temperature, this value is arbitrary and can be set equal to zero in the selected node of the finite element mesh. In the temperature dependent problem the instantaneous effective properties might, however, be strongly influenced by the current temperature. This term then plays an important role.

2.2.2 Embedded cell approaches (ECAs)

A developing area of computational micromechanics involves the analyzing of the mechanical behavior by means of embedded cell models. In this approximation, full details of the

composite microstructure (including the matrix, reinforcements and interfaces) are resolved in the desired region, while simple constitutive equations (based on any suitable homogenization approximation) and coarser discretizations are used in the rest of the model to save computer time (Fig. 2.4(a)), for more see (González and Lorca, 2007; Böhm, 2007, and references therein).

The embedded region serves mostly as a transition zone for transmitting the applied loads into the core. In comparison with periodic microfield approaches these methods do not require strictly periodic microfields. Therefore, they can be used to study temperature dependent conductivities in thermal analysis.

2.2.3 Window approaches (WAs)

These approaches are possibly the simplest one of the methods studying discrete microstructure at least from the effort consuming cell's preparation point of view. To study the discrete microstructure the simply shaped windows (cells) are extracted from the image of the real material arrangement and subjected to the non-periodic conditions guarantying the macrohomogeneity conditions. For that reason, the phase distribution statistics are also employed, see (Cluni and Gusella, 2004).

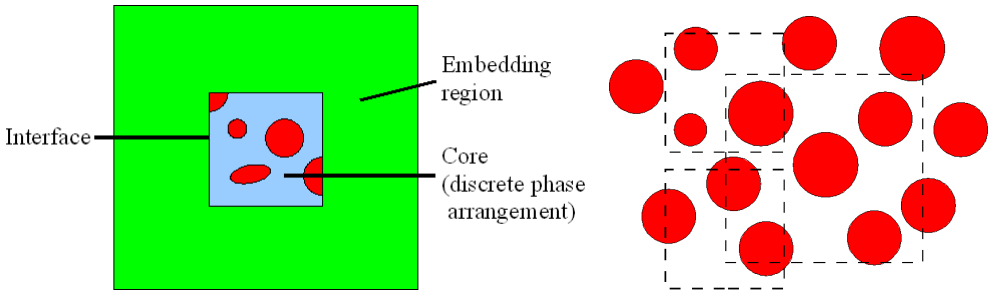

Figure 2.4: Schematic depiction: (a) Embedded cell approach, (b) window approaches (possible windows are scatched by the dashed line)

Chapter 3

EXPERIMENTAL PROGRAM

As already stated in the introductory part much of the considered here is primarily computational. However, no numerical predictions can be certified if not supported by proper experimental data (Knauss, 2000). The objective of the experimental program in the context of the present study is twofold. First, reliable geometrical data for the construction of the unit cell and material parameters of both the carbon fibers and carbon matrix for the prediction of effective properties are needed. Since still derived on the basis of various assumptions these results must be next confirmed experimentally to acquire real predictive power. Hereinafter, only the former perception of computation-theory interaction is discussed while the latter one will be mentioned in due course.

Considering the mesoscopic complexity of C/C composites the supportive role of experiments is assumed to have the following three components:

- Two-dimensional image analysis providing binary sections of the composite further exploited in the derivation of one- or two-layer statistically equivalent periodic unit cell (SEPUC)

- X-ray tomography yielding a three-dimensional map of distribution, shape and volume fraction of major pores to be introduced into, yet void-free, SEPUC.

- Nanoindentation tests supplying the local material parameters which either depend on the manufacturing process or are not disclosed by the producer.

For the above purposes a carbon-polymer (C/P) laminated plate was first manufactured by molding together eight layers of carbon fabric Hexcel G 1169 composed of carbon multifilament Torayca T 800 HB and impregnated by phenolic resin Umaform LE. A set of twenty specimens having dimensions $25 \times 2.5 \times 2.5$ mm were then cut out of the laminate and subjected to further treatment (carbonization C at 1000°C, reimpregnation I, recarbonization,

second reimpregnation and final graphitization G at 2200°C $(CICICG)$) to create the C/C composite, see Fig. 3.1 for an illustration and (Tomková, 2006) for more details. The reported specimens were then fixed into the epoxy resin and subject to curing procedure. In the last step, the specimen was subjected to final surface grounding and polishing using standard metallographic techniques. This part of the specimen preparation should deserve a special attention as it has a detrimental influence on the quality of digitized images.

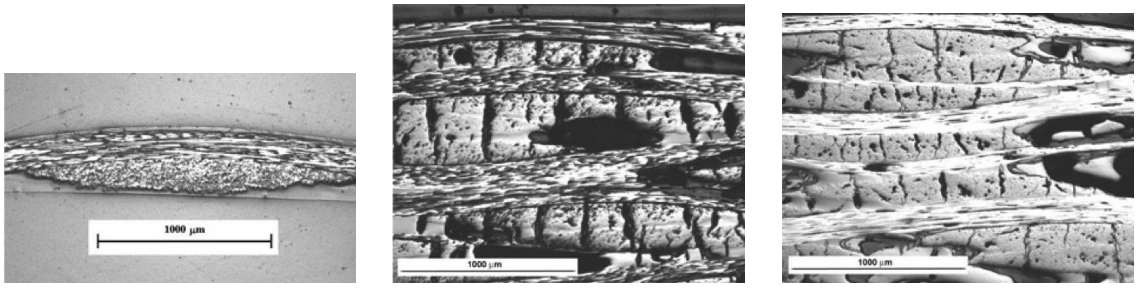

(a) (b) (c)

Figure 3.1: Examples of scanned microstructures: (a) Woven fabric, (b) carbonized composite, (c) graphitized composite

3.1 Two-dimensional image analysis

The actual image analysis device used for structural image acquisition and analysis consists of NIKON ECLIPSE E 600 microscope, Märzhauser motorized scanning stage, digital monochrome camera VDC 1300C and image analysis software **LUCIA G**[1] (LIM, 2008). Note that high reflectance of the woven fabric allows relatively good visual resolution of individual parts of a composite structure as demonstrated in Fig. 3.1. Using the method of gradual abrasion of the surface of transverse sections of the composite laminate allowed us to generate a voluminous database of micro-images intended for further processing. Unfortunately, a low color contrast of the reinforcement (carbon fabric) and matrix is a major impediment to an automatic separation of individual objects. Therefore, a manual preprocessing of images by marking the borders of selected objects becomes often necessary, cf. Fig. 3.2. Further image analysis and object measurement was, however, fully automatic providing a sufficient insight into the space arrangement of the reinforcements and pores including an

[1] `www.lim.cz`

average thickness of carbon tows, shape and essential dimensions of fiber tow cross-section, size and shape of major voids, distribution of transverse and delamination cracks, etc.

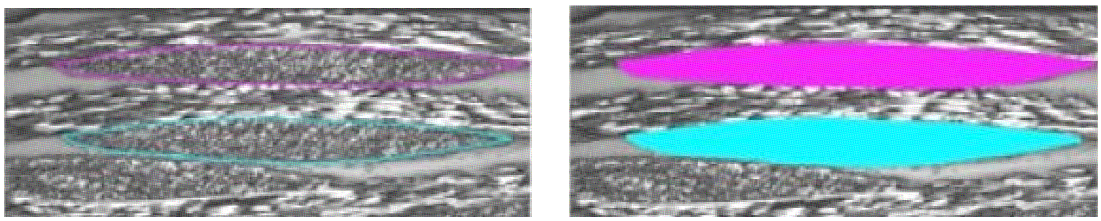

(a) (b)

Figure 3.2: Image processing steps: (a) Manual marking of object borders, (b) automatic marking of objects

Although, as demonstrated in Section 5.2.1, statistical consideration of the acquired results proved useful, the essential input for the preparation of physical models for computational analysis (SEPUC) is given by binary images of the composite. A particularly perspicuous illustration of the result of two-dimensional image processing is available in Fig. 3.3 implicating that material porosity is paid no attention to when treating only the geometrical imperfections of the fabric reinforcements. At this point, a direct comparison of the resulting mesoscopic predictions with experimental measurements would therefore be meaningless.

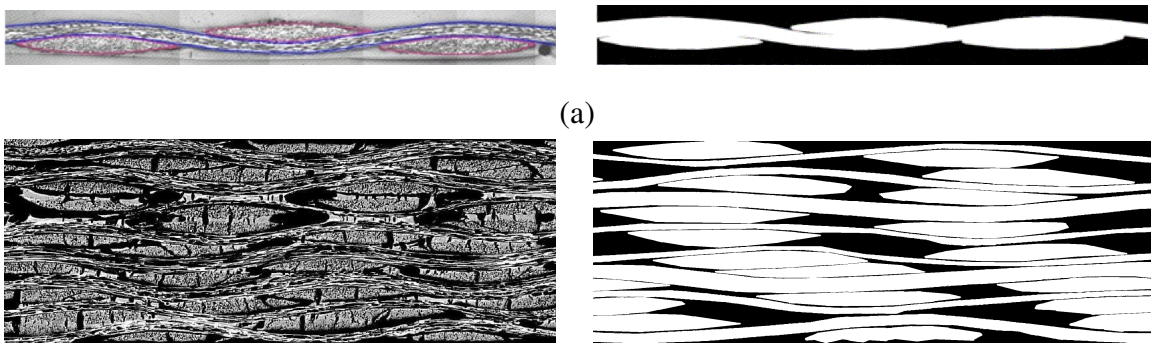

(a)

(b)

Figure 3.3: Examples of image analysis: (a) Woven fabric, (b) multi-layered C/C composite

3.2 Three-dimensional X-ray microtomography

There is no dispute that porosity of C/C composites plays an important role in the derivation of effective material properties. Most common approach to characterizing this property employs sectioning, recall Section 3.1. The influence of shape of pores, estimated from 2D images or real C/C composites (Tomková and Košková, 2004), on the mechanical response has been addressed e.g. in (Košek et al., 2008; Tsukrov et al., 2005). However, as suggested in (Vorel and Šejnoha, 2009), two-dimensional estimates of the porosity may significantly pollute the final predictions of the material response when compared to three-dimensional simulations. In this regard, the X-Ray microtomography (Dobiášová et al., 2002; Djukic et al., 2008; Pahr and Zysset, 2006) becomes a valuable tool rendering three-dimensional phase information. In the present study, high resolution computer tomography images provided by the Interfacultary Laboratory for Micro- and Nanomechanics of Biological and Biomimetical Materials of the Institute of Lightweight Design and Structural Biomechanics were used to obtain the shape, size, location and volume fraction of inter-layer (crimp) voids. A particular example of the distribution of major porosity in C/C multi-layered plane-weave composite is presented in Fig. 3.4. While the basic characteristics of the porosity can be extracted from these images with no particular difficulty, a direct introduction of pores in their full complexity as seen in Fig. 3.4(a) is impossible. Instead, a discrete set of oblate spheroids approximating the shape and volume of actual pores is accommodated in between the two layers of the SEPUC fitting their true location as close as possible. Further details together with the way of handling the minor porosity observed in individual tows are presented in Section 4.3.2.

3.3 Phase elastic moduli from nanoindentation

Prediction of complex macroscopic response of highly heterogeneous materials from local phase constitutive theories is a formidable aspect of micromechanical modeling. The reliability of these predictions, however, is considerably influenced by available information on material data of individual constituents. Even though supplied by the producer, these information are often insufficient for three-dimensional analysis. It is also known that material properties of the matrix much depend on the fabrication of composite and may considerably

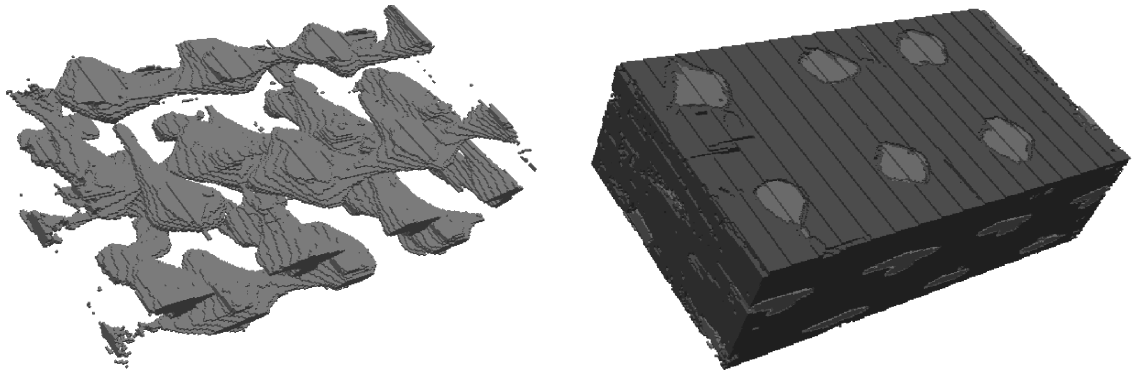

(a) (b)

Figure 3.4: X-ray microtomography: (a) Interior distribution and shape of large vacuoles, (b) three-dimensional view of the porous composite structure

deviate from those found experimentally for large unconstrained material samples (Dvorak, 2000).

Carbon matrix developed in the composite through a repeated process of impregnation, curing and carbonization of the phenolic resin is a solid example. This resin falls into the category of non-graphitizing resins so that the final carbon matrix essentially complies, at least in terms of its structure, with the original cross-linked polymeric precursor. Therefore, the resulting material symmetry is more or less isotropic with material parameters corresponding to those of glassy carbon. Nevertheless, when constrained the assumed matrix isotropy may evolve into the one of the fibers particularly in their vicinity. Although the carbon fibers are known to have a relatively low orderliness of graphen planes on nano-scale, they still posses a transverse isotropy with the value of longitudinal tensile modulus (usually available) considerably exceeding the one in the transverse direction (often lacking). Additional experiments, preferably performed directly on the composite, are therefore often needed to either validate the available local data or to derive the missing ones.

At present, nanoindentation is the only experimental technique that can be used for direct measurement of mechanical properties at material micro-level. A successful application of nanoindentation to C/C composites has been reported in (Kanari et al., 1997; Marx and Riester, 1999; Diss et al., 2002b). In the present study, our only attention was limited to the evaluation of the matrix elastic modulus and the transverse elastic modulus of the fiber. The remaining data were estimated from those available in the literature for similar material

systems.

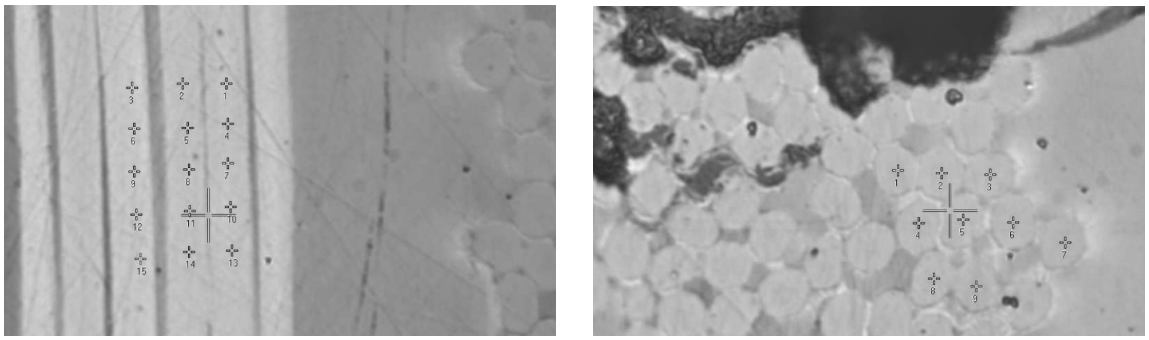

(a) (b)

Figure 3.5: Nanoindentation - location of indents: (a) Transverse direction, (b) longitudinal direction (compression)

Three locations, distinctly separated in optic microscope, were tested - matrix, parallel fibers Fig. 3.5(a), perpendicular fibers Fig. 3.5(b). The matrix was therefore assumed isotropic and possible anisotrophy, which may arise inside the fiber tow, was not considered. As seen in Fig. 3.5 several measurements were recorded for each of the three locations. The measurements were performed using CSM Nanohardness tester equipped with a Berkovich tip allowing for 0.1-500 mN loading range. To ensure elastic response relatively low indentation forces up to 10 mN were considered. The elastic moduli were extracted from an unloading part of the indentation curve using the well known method proposed by Oliver and Pharr (1992). The analysis is based on the analytical solution known for rotational bodies punched into the elastic isotropic half-space. The indentation elastic modulus is then provided by

$$E_r = \frac{K\sqrt{\pi}}{2\sqrt{A_{PL}}}, \tag{3.1}$$

where A_{PL} is the projected contact area at the peak load and K is the contact stiffness evaluated as the initial slope of the unloading curve. The following equation is then adopted to account for a finite elastic stiffness of the indenter

$$\frac{1}{E_r} = \frac{1-\nu^2}{E} + \frac{1-\nu_i^2}{E_i},$$

where E and ν are the elastic modulus and Poisson ratio of the tested material and E_i and ν_i are parameters of the indenter (for diamond: E_i=1141 GPa and ν_i =0.07). In this study, the

matrix Poisson ratio was assumed equal to 0.2 while the fiber Poisson ration was set equal to 0.4. The complete set of parameters, both measured averages labeled by $\cdot^*$ and those adopted from literature, is available in Tab. 3.1. Note that the matrix modulus agrees relatively well with the one found for the glassy carbon in (Diss et al., 2002b).

Table 3.1: Material parameters of individual phases

Material		Young modulus [GPa]	Shear modulus [GPa]	Poisson ratio [-]
fiber	longitudinal	294	11.8	0.24
	transverse	12.8*	4.6	0.4
matrix		23.6*	9.8	0.2

The final note is concerned with heat treatment of the C/C composite during fabrication. It has been observed experimentally (Černý et al., 2000) that even for T800 based composites the tensile Young's modulus increases for graphitized specimens ($CICICG$) when compared to only carbonized ones ($CICIC$). It is suggested that this phenomenon may be caused by further stiffening of carbon fibers. This, however, is difficult to address in the present study as the tensile modulus cannot be measured via nanoindentation. On the contrary, neither the matrix properties nor the porosity profile is expected to change considerably with graphitization. Therefore, the experimental data reported in (Černý et al., 2000) for the $CICIC$ system rather than those for $CICICG$ system will be fostered for comparison with numerical predictions.

3.4 Laboratory evaluation of effective properties

Corroboration of a mechanics model by experimental data is still thought vital for the model to be accepted, inasmuch as there is simply nothing better, even though an experiment often comprises laboratory measurements and a theory for calculating not directly measurable parameters.

With regard to thermophysical parameters the pulse transient method (Kubičár et al., 2002) combined with a heat loss model for the calculation of temperature response, when

lower currents are used for pulse generation, is often adopted. The searched thermal conductivities are found subsequently using a general relation between thermal conductivity, specific heat and thermal diffusivity, the latter two given in terms of the maximum attained temperature, the elapsed time to reach this temperature, total amount of generated heat and a set of correction factors characterizing deviations of calculated thermal diffusivity and specific heat from those derived for an ideal system (ideal heat source placed in boundless isotropic body). It is not the objective of this section to provide all details of this method, as these can be found, e.g. in (Kubičár et al., 2002; Boháč, 2005), but rather to suggest the complexity of deriving the effective thermal conductivities from an experiment, which in turn are to be used to question the quality of numerical predictions presented later in Chapter 5. In particular, in support of the proposed approach to the numerical computation of effective thermal conductivities of C/C composites we borrow the results presented by Boháč (2005). Averages of the measurements from six samples of a C/C laminate are available in Tab. 3.2.

Table 3.2: Phase (Tomková, 2006), unidirectional (UD) C/C composite (porous fiber tow) and laminate effective thermal conductivities (Boháč, 2005)

Material	Thermal conductivities $[\mathrm{Wm^{-1}K^{-1}}]$		
	χ_{11}	χ_{22}	χ_{33}
air	0.02	0.02	0.02
fiber	35	0.35	0.35
matrix	6.3	6.3	6.3
C/C laminate	10 (warp)	10 (weft)	1.6

Similar difficulties arise when deriving the dynamic tensile and shear moduli from a resonant frequency method. While the basic longitudinal resonant frequency of a beam with free ends is used to extract the tensile Young's modulus E_{11}, the complete frequency equation for flexural vibration of a beam with free ends is solved to obtain the longitudinal shear modulus G_{12} (Vozková, 2008).

Among other material system this technique was employed in (Černý et al., 2000) to derive the homogenized tensile and shear moduli of a four layer T800 fiber fabric based plain weave C/C composite. As part of their study a unidirectional (UD) carbonized $CICIC$

composite was examined. The resulting moduli stored in Tab. 3.3 were utilized here to validate the Mori-Tanaka estimates of the homogenized properties of the porous fiber tow, see Section 5.1. Contemplation of the MT micromechanics model on the level of fiber tow has two reasons. First, it provides the homogenized fiber tow conductivity and stiffness matrices needed in the mesoscopic study (Chapter 5) relatively easily. Second, the acquired predictions are sufficiently "reliable" when no microstructure information other than volume fractions of individual constituents are at hand. In the present study a relatively high volume fractions of fibers equal to 68% and open porosity by water penetration of 6.6% were taken from Černý et al. (2000). Comparison of the predicted and measured longitudinal moduli presented in Section 5.1 verifies both the local phase properties given in Tab. 3.1 and justifies the use of the MT method (Section 2.1.1.4).

Table 3.3: Effective elastic properties of UD C/C composite (porous fiber tow) and C/C laminate (Černý et al., 2000)

Material	E_{11} [GPa]	G_{12} [GPa]
porous tow	≈ 200	≈ 11.5
C/C laminate	≈ 65	≈ 6

Chapter 4

MODELING STRATEGY OF C/C PLAIN WEAVE COMPOSITES

As mentioned in Section 1.2.5 one can recognize three different scales in plain weave composites. It has been demonstrated in previous works, see e.g. (Šejnoha et al., 2008; Zeman and Šejnoha, 2001) that image analysis of real, rather then artificial, material systems plays an essential role in the derivation of a reliable and accurate computational model. This issue is revisited here for the case of a woven fabric C/C laminate with particular relation to the adopted uncoupled multi-scale solution strategy (first order homogenization procedure).

For illustration, let us now consider an eight-layer carbon-carbon composite laminate. Individual plies are made of plain weave carbon fabric embedded in a carbon matrix. Each filament (fiber tow) contains about 6000 carbon fibers, see Chapter 3. A typical segment of the composite laminate appears in Fig. 1.2(b) showing characteristic porosity which may exceed at the structural level (macro-scale) 30% and is often considered as an intrinsic property of this type of composite. Several such micrographs were processed by Tomková et al. (2007) to acquire information regarding the basic structural units like an average thickness of carbon tows, size of voids, shape and essential dimensions of fiber tow cross-section, distribution of transverse and delamination cracks etc. These parameters were exploited in (Tomková et al., 2007) to construct statistically equivalent periodic unit cells (SEPUC) subsequently used in the FEM simulations.

4.1 Statistically equivalent period unit cell

The concept of statistically equivalent periodic unit cell for random or imperfect microstructures is now well established. A lucid presentation of individual steps enabling the substitution of real microstructures by their simplified artificial representatives - the SEPUCs - is available, e.g. in (Zeman and Šejnoha, 2001, 2004a, 2007) and additional references given below. Herein, these steps are briefly reviewed concentrating on the specifics of SEPUC for

two-layer woven composites.

4.1.1 Quantification of random microstructure

Assuming a statistically homogeneous and ergodic binary material system, two basic two-point statistical functions are available to capture the essential characteristics of the analyzed tow-matrix material system. In particular, the first descriptor is a two-point probability function $\mathcal{S}(\mathbf{x})$ (Torquato and Stell, 1982), which quantifies the probability that two points, separated by vector $\mathbf{x}$, will be both found in the domain occupied by warp and weft tows (i.e. the white region in Fig. 3.3). Additional statistics, proposed by Lu and Torquato (1992) to better describe long-large effects, is the linear path function $\mathcal{L}(\mathbf{x})$ giving the probability of locating a randomly placed segment $\mathbf{x}$ fully in the tow region. Both descriptors can be easily computed for digitized microstructures: in particular, the Fast Fourier transform library **FFTW** (Frigo and Johnson, 2005) is used for the $\mathcal{S}$ function, while the sampling template procedure is introduced for the determination of the linear path function; see also (Torquato, 2002) for an in-depth discussion of this topic.

4.1.2 Calibration of SEPUC parameters

In overall, the adopted model of the unit cell involves seven independent parameters

$$\mathbf{y} = [a, b, g, h, \Delta_1, \Delta_2, \Delta_3]\,, \tag{4.1}$$

to be determined form available microstructural data, see Fig. 4.6. For the sake of generality, we assume that the microstructure configuration is characterized by microstructural function associated with (at most) warp and weft directions; i.e. functions $\mathcal{S}_{\mathsf{warp}}$ and $\mathcal{L}_{\mathsf{warp}}$ for the warp and descriptors $\mathcal{S}_{\mathsf{weft}}$ and $\mathcal{L}_{\mathsf{weft}}$ for the weft directions, recall Fig. 4.6(b). Following (Yeong and Torquato, 1998a), the following quantities are introduced to measure the similarity between the SEPUC and the original microstructure:

$$\mathcal{O}^2_{\mathcal{S}}(\mathbf{y}) = \sum_{p\in\{\mathsf{warp},\mathsf{weft}\}} \sum_{i=i_{\min}}^{i_{\max}} \sum_{j=j_{\min}}^{j_{\max}} \left(\mathcal{S}_p(\mathbf{y},i,j) - \overline{\mathcal{S}_p}\right)^2, \tag{4.2}$$

$$\mathcal{O}^2_{\mathcal{L}}(\mathbf{y}) = \sum_{p\in\{\mathsf{warp},\mathsf{weft}\}} \sum_{i=i_{\min}}^{i_{\max}} \sum_{j=j_{\min}}^{j_{\max}} \left(\mathcal{L}_p(\mathbf{y},i,j) - \overline{\mathcal{L}_p}\right)^2, \tag{4.3}$$

$$\mathcal{O}_{\mathcal{S}+\mathcal{L}}(\mathbf{y}) = \alpha_{\mathcal{S}}\mathcal{O}_{\mathcal{S}}(\mathbf{y}) + \alpha_{\mathcal{L}}\mathcal{O}_{\mathcal{L}}(\mathbf{y}), \tag{4.4}$$

where e.g. $\mathcal{S}_{\mathsf{warp}}(\mathbf{y}, i, j)$ denotes the two-point probability function determined for the warp direction of a SEPUC described by parameters $\mathbf{y}$ and the value of argument $\mathbf{x} = [i, j]$. The $\alpha_\bullet$ symbol in Eq. (4.4) denotes a scale factor used to normalize the influence of both descriptors.[1]

An additional term is introduced into the objective function to eliminate the intersection of the upper-layer and lower-layer tows. To that end, we compute the overlap δ as the signed distance between the upper and lower tow surfaces and introduce the constraint $\delta \geq 0$ via an exponential exterior penalty function:

$$\mathcal{P}_D(\mathbf{y}) = \left(1 + \frac{\delta_-(\mathbf{y})}{h}\right)^{\lambda} \mathcal{O}_D(\mathbf{y}), \tag{4.5}$$

where δ_- denotes the negative part of δ, D can take values $[\mathcal{S}, \mathcal{L}, \mathcal{S}+\mathcal{L}]$ and the value of exponent $\lambda = 3$ was used in all the reported calculations. Note that a similar procedure was adopted by Kumar et al. (2007) in the formulation of SEPUC for high-density polydisperse particulate composites.

Now, the optimal values of the SEPUC parameters can be determined from the solution of a box-constrained global optimization problem

$$\mathbf{y} \in \operatorname*{Argmin}_{\mathbf{l} \leq \mathbf{z} \leq \mathbf{u}} \mathcal{O}_D(\mathbf{z}), \tag{4.6}$$

where the lower and upper bounds $\mathbf{l}$ and $\mathbf{u}$ can be, e.g. determined on the basis of image analysis.[2] A closer inspection reveals that all objective functions (4.5) are multi-modal and discontinuous due to the effect of limited bitmap resolution (Zeman, 2003). According to our previous experience with evolutionary optimization algorithms, a stochastic optimization algorithm **RASA** (Matouš et al., 2000; Hrstka et al., 2003), based on a combination of real-valued genetic algorithm and simulated annealing method, is used to solve the problem (4.6).

4.1.3 Verification of optimization procedure

To examine the robustness and performance of the proposed optimization process based on the two-point probability function $\mathcal{S}(\mathbf{x})$, the artificial 512×224 pixels bitmap of a two-

[1] In all reported computations, values of the weights were determined to normalize the average value of each summed to one and were estimated from 20 independent simulations.

[2] Note that when the same statistics is assumed for both warp and weft directions, cf. Section 4.1.3, we set $\Delta_1 = \Delta_2$ and consider only one set of descriptors.

layer composite with parameters $a = 10$, $h = 4.5$, $b = 1.5$, $g = 2$, $\Delta_1 = \Delta_2 = 5$ and $\Delta_3 = -1$ was generated as a reference microstructure. For each component of the vector $\mathbf{x}$, the lower and upper bounds were set to 50% and 200% of the target value, respectively. Finally, the algorithm was terminated once the solution with the value $\mathcal{P}_{\mathcal{S}}$ smaller then 10^{-6} was found. The setting of all parameters of the **RASA** algorithm are specified in detail in (Zeman, 2003, Appendix C). In order to take into account the stochastic character of the algorithm, the optimization method was run 20 times and the minimum and maximum values of the searched geometric parameters and the number of the objective function evaluations until convergence were recorded. Results of this numerical experiment are stored in Tabs. 4.1 and 4.2.

Table 4.1: Results of the verification procedure

Success rate	Number of function calls		
	Minimum	Average	Maximum
20/20	4,316	8,866	21,456

Table 4.2: Accuracy of identified parameters

a	b	g	h	$\Delta_1 = \Delta_2$	Δ_3
10.01 ± 0.05	1.5 ± 0.00	2.00 ± 0.08	4.50 ± 0.02	5.02 ± 0.08	1.00 ± 0.04

Notice that the optimization algorithm was able to find a solution corresponding to a given value of the objective function for every run in a moderate number of iterations, which justifies the choice of the global stochastic optimization algorithm. Furthermore, it is clearly evident that the precision of identified parameters stays roughly on the same level, the "horizontal" parameters g, Δ_1 and a are associated with the highest error. Nevertheless, the maximum scatter of identified parameters is less than 4% for all coefficients, which is more than sufficient for the required accuracy in practical problems, dealing with systems with substantially more irregular geometry. Moreover, it should be emphasized that the scatter in geometrical parameters can be solely attributed to the problem discretization and to the

nature of genetic algorithms. From the material statistics point of view, all the unit cells resulting from the optimization procedure are identical.

4.1.4 Multi-layered C/C composites

For the procedure of the two-layer SEPUC determination, all the internal parameters of the optimization method were the same as in the case of the verification experiment. The maximum number of function evaluation was set to $50,000$. The lower and upper bounds correspond to the scaled 5 and 95% probability quantiles of parameters measured directly from several bitmaps (Fig. 3.3(b)) and appear in Tab. 4.3, see (Tomková and Košková, 2004; Skoček et al., 2008; Zeman and Šejnoha, 2004b) and Tab. 5.11 for unscaled values. The optimum found from 20 independent executions of the **RASA** algorithm is stored in the last row of the same table. In addition, statistics of the optimal values appears in Tab. 4.4, confirming robustness of the found global minimum.

Table 4.3: Bounds and optimal parameters on the two-layer SEPUC. Dimensions of SEPUC are scaled such that the mean value of a parameter equals to 10

	SEPUC parameters					
	a	b	g	h	$\Delta_1 = \Delta_2$	Δ_3
Lower bound	8.87	0.51	1.01	0.93	-4.93	-0.80
Upper bound	11.13	0.81	2.55	1.74	4.93	0.80
SEPUC	**9.83**	**0.53**	**1.90**	**1.13**	**1.30**	**-0.21**

Table 4.4: Statistics of local minima

Value of objective function $\mathcal{P}_{\mathcal{S}}$		
Minimum	Average	Maximum
6.770×10^{-3}	6.852×10^{-3}	7.256×10^{-3}

The resulting three-dimensional scheme of the statistically optimal unit cell appears in Fig. 4.1s. From the qualitative point of view, it is evident that the SEPUC tries to re-

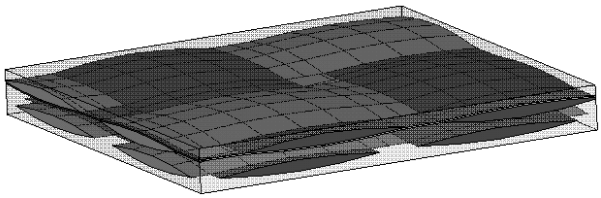

Figure 4.1: The resulting three-dimensional scheme of the statistically optimal unit cell

produce the matrix rich regions together with the strong nesting of individual layers, of course within the constraints of the selected geometrical model and the impenetrability condition. It is worth noting that the "two-dimensional" tow volume fraction in Fig. 3.3(b) is approximately 65%, which corresponds to $\approx 51\%$ volume of tows reported for pore-free composite in (Skoček et al., 2008). This provides additional argument for representativeness of the three-dimensional model, as this information was not included in the objective function Eq. (4.5).

4.2 Micro-scale

Starting with the fiber tow composite as the basic structural element we call Fig. 4.2 showing a typical shape of the fiber tow cross-section and significant amount of transverse cracks and voids resulting in a non-negligible porosity. To evaluate the effective conductivity ten-

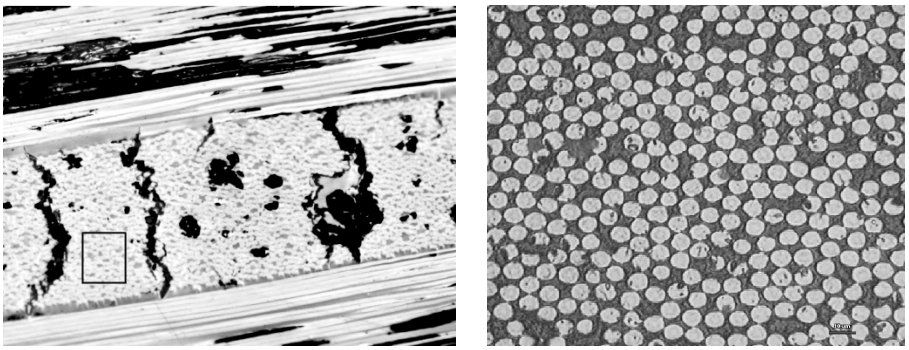

(a) (b)

Figure 4.2: Homogenization on micro-scale: (a) Fiber tow composite, (b) fiber-matrix composite

sor a two-step homogenization approach is adopted together with formulations discussed in Chapter 2, see also (Tomková et al., 2008). It combines evaluation of effective properties in the absence of pores with a subsequent homogenization step in which the porous phase is introduced into a new homogenized matrix.

In the first step of the proposed multi-scale homogenization scheme a single filament (fiber tow) of a plain weave carbon fabric Hexcel 1/1 bonded to a carbon matrix is considered, Fig. 4.2(a). As mentioned, each filament contains significant amount of transverse cracks and voids resulting in a porosity of more than 10% (Tomková and Košková, 2004; Tomková et al., 2008). While the matrix phase, which essentially corresponds to a glassy carbon, is assumed isotropic the carbon fiber possess a transverse isotropy with the values of material properties in longitudinal direction considerably exceeding the one in the transverse direction. For illustration the phase thermal conductivities are listed in Tabs. 3.1,3.2. Considerable difference in the size of the two types heterogeneities (fibers and pores) readily suggests a two step homogenization procedure to predict the effective properties of the fiber tow.

4.3 Meso-scale

The micromechanical analysis of composite materials is primarily concerned with the thermomechanical behavior of a single ply composite, Figs. 1.1(a-c). On this level of sophistication the main stream of research has been directed to prediction of effective behavior of composite aggregate (single lamina), as well as to find estimates of local fields, while accounting for actual behavior of individual material constituents and their interaction. Due to poor transverse properties of the unidirectional lamina in particular it is not usually used as a separate structural unit, but rather as an element of more complex composite structures, such as laminated plates. Appropriate selection of material properties of individual plies, orientation and stacking sequence can considerably enhanced the mechanical behavior of composite structures, e.g. the plain weave composites are utilized to improve the material properties (Fig. 1.2(a)). At the structural level, each layer is usually modeled as an equivalent homogeneous material with effective properties derived from various micromechanical models listed in Chapter 2.

Note, however, that the real composite shows a number of imperfections which certainly should not be completely disregarded. It will be seen later in following chapters that the nonuniform waviness and to some extent also the mutual shift of individual layers clearly visible in Fig. 1.2 can be accounted for by utilizing histograms of inclination angles derived from centerlines of individual fiber tows (Fig. 4.3(a), (Vopička, 2004)).

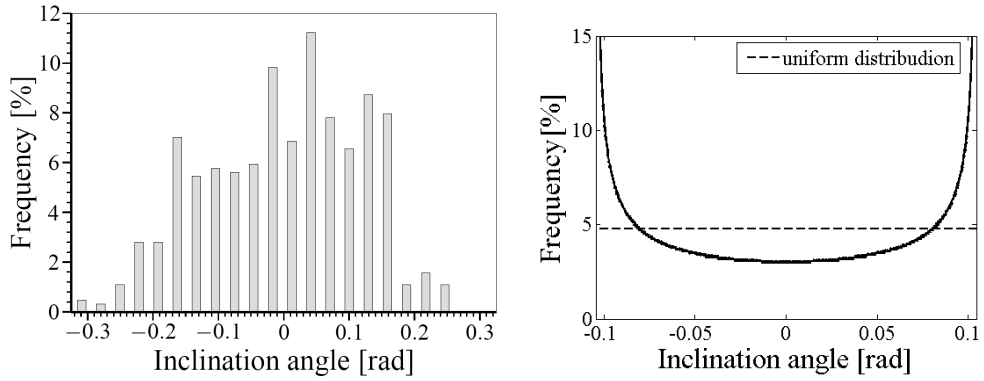

(a) (b)

Figure 4.3: Inclination angles: (a) Example of a real histogram, (b) approximate distribution (PUC)

Having derived the effective material parameters for the fiber tow composite the assumed homogenization procedure continues along the same lines on the meso-scale as on the micro-scale. However, for the finite element based approaches the influence of both the tow paths and pores is mostly accounted for at once (one-step homogenization approach). To motivate the application of the theory summarized in the Chapter 2 to textile composites, consider an idealized geometrical model of a plain weave composite shown in Fig. 4.4.

4.3.1 Mori-Tanaka analysis

The basic building block of the adopted SEPUC is provided by a single-ply model of plain weave composite geometry proposed in (Kuhn and Charalambides, 1999). The model consists of two orthogonal warp and weft tows embedded in the matrix phase and it is parameterized by four basic quantities: the tow wavelength $2a$, the tow height b, tow spacing g and the layer thickness h. For this particular case (as well as for almost all geometrical models available in the literature), the centreline of the warp tow is described using a simple

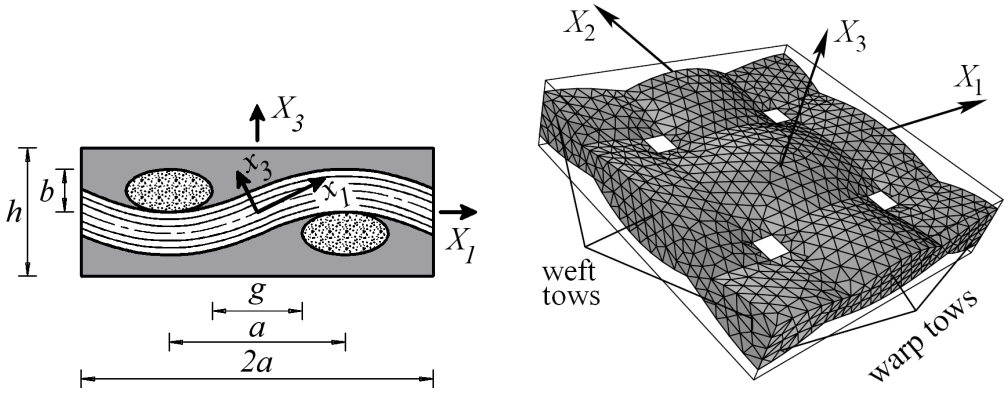

(a) (b)

Figure 4.4: Idealized geometrical model for plane weaved composite: (a) Geometrical parameters, (b) three-dimensional view

trigonometrical function

$$s\left(x\right)=\frac{b}{2}\sin\left(\frac{\pi x}{a}\right). \tag{4.7}$$

To characterize the distribution of inclination angles for idealized model the Euler angles (ϕ,θ,β) are introduced (Fig. 4.5). Recall that the relation between the local coordinate

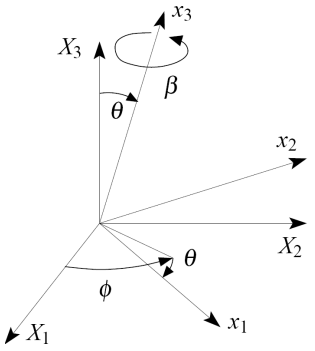

Figure 4.5: Local coordinate system and definition of the Euler angles

system $\mathbf{x}$ and the global coordinate system $\mathbf{X}$ is provided in terms of transformation matrix $\boldsymbol{P}$ as

$$\mathbf{X}=\boldsymbol{P}\mathbf{x}. \tag{4.8}$$

The specific transformation matrix consistent with Fig. 4.5 then reads [3]

$$\boldsymbol{P} = \begin{bmatrix} \cos\phi\cos\theta\cos\beta - \sin\phi\sin\beta & \sin\phi\cos\theta\cos\beta + \cos\phi\sin\beta & -\sin\theta\cos\beta \\ -\cos\phi\cos\theta\sin\beta - \sin\phi\cos\beta & -\sin\phi\cos\theta\sin\beta + \cos\phi\cos\beta & \sin\theta\sin\beta \\ \cos\phi\sin\theta & \sin\phi\sin\theta & \cos\theta \end{bmatrix}. \tag{4.9}$$

If we consider directly the simplified geometrical model in Fig. 4.4(b), the joint probability density function $f(\phi, \theta, \beta)$ results from the harmonic shape of the centerline as described by Eq. (4.7). Applying the change of variable formula (Rektorys, 1994, Section 33.9), we obtain after some algebra the expression of the probability density in the form

$$f(\phi,\theta,\beta) = \begin{cases} \dfrac{2a}{\pi}\dfrac{1+\tan^2(\theta)}{\sqrt{b^2\pi^2 - 4a^2\tan^2(\theta)}} & \text{if } \phi = 0, \beta = 0 \text{ and } -\alpha \leq \theta \leq \alpha, \\ 0 & \text{otherwise,} \end{cases}$$

where

$$\alpha = \arctan\left(\frac{b\pi}{2a}\right).$$

Assuming simply a uniform distribution of inclination angles the joint probability density function attains the form

$$f(\phi,\theta,\beta) = \begin{cases} \dfrac{1}{2\alpha} & \text{if } \phi = 0, \beta = 0 \text{ and } -\alpha \leq \theta \leq \alpha, \\ 0 & \text{otherwise.} \end{cases}$$

Both functions are plotted in Fig. 4.3(b) for comparison. In this study, the latter function is adopted for simplicity.

4.3.2 Finite element analysis - computational model

In this section the formulation of a computational model intended for the finite element based homogenization is presented. As a stepping stone the SEPUC presented in the previous section is utilized. The three-dimensional woven composite SEPUC, shown in Fig. 4.6, is formed by two identical one-layer blocks, relatively shifted by distances Δ_1, Δ_2 and Δ_3 in the direction of the corresponding coordinate axes. Finally, cutting a SEPUC by the plane

[3] Note that so-called "x_2 convention" is used; i.e. a conversion into a new coordinates system follows three consecutive steps. First, the rotation of angle ϕ around the original X_3 axis is done. Then, the rotation of angle θ around the new x_2 axis is followed by the rotation of angle β around the new x_3 axis to finish the conversion.

$X_1 = X_2 = \pm a$ yields the warp and weft two-dimensional sections, used as the basis for the determination of the unit cell parameters.

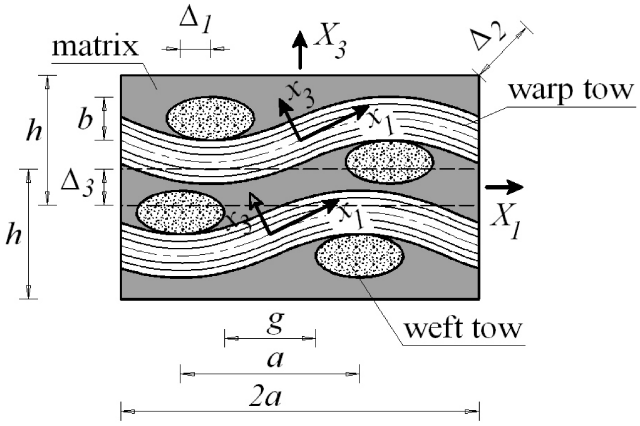

Figure 4.6: Geometrical model of two-layer SEPUC (two-dimensional cut)

The FEM homogenization technique implies the use of conforming finite element meshes easily enabling the implementation of periodic boundary conditions already mentioned in Section 2.2.1. This might seem daunting in that it requires not only incorporation of an arbitrary shift of the two layers of fabric reinforcement, but also an independent introduction of voids in a way broadly similar to that outlined already in Section 3.2. An illustrative example of the geometry of such a model is presented in Fig. 4.7.

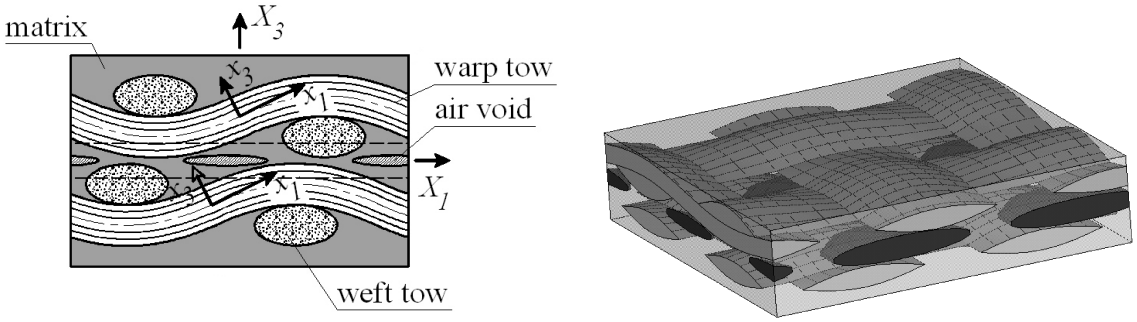

(a) (b)

Figure 4.7: Computational model: (a) Two-dimensional cut of a two-layer model with voids (b) 3D view of the geometry of a two-layer UC model with voids

In the present study this step is accomplished by combining the principles of CAD modeling (Hivet and Boisse, 2005) with the volumetric modeling capacities of the **ANSYS**®

package[4] (ANSYS, 2005).

In order to ensure the symmetry of the resulting FEM mesh, a primitive block of the tow is modeled first, see Fig. 4.8(a). Subsequently, using mirroring, copying and merging operations, the whole volume of one reinforcement layer is generated, Fig. 4.8(b). The second layer is derived analogously and then placed according to parameters Δ_1, Δ_2 and Δ_3 as shown in Fig. 4.8(c). The porous phase is introduced next being represented by four identical oblate spheroids, the volume of which is derived from X-ray microimages shown in Fig. 3.4. These are then periodically extended over the entire model, Fig. 4.8(d). Their location is assumed to mimic the distribution of large vacuoles that typically appear, as also seen in Fig. 1.3, in the location of tow crossing. However, this is difficult to achieve in general, and thereby the porous phase was excluded from the minimization problem presented in Section 4.1. Finally, the volume corresponding to matrix is generated using the subtraction of the body of reinforcements and the $2a \times 2a \times (2h + \Delta_3)$ parallelepiped defining the SEPUC. The resulting geometrical model appears in Fig. 4.7(b).

Now, the mapped meshing technique (Wentorf et al., 1999; Matouš et al., 2007) can be employed to ensure periodicity of the resulting finite element mesh. First, half of the external surfaces of the SEPUC are discretized and the mesh is then copied to the homologous surfaces. Next, the tetrahedral elements corresponding to tows, voids and matrix are generated based on the data created in the previous steps. The corresponding finite element mesh is shown for illustration in Figs. 4.8(e)–(f).

4.4 Macro-scale

The macromechanical analysis of multilayer structure is employed to predict gross mechanical behavior of composite structures regardless of the constituent materials or their interaction. Extensive use of composite laminates in structural engineering has been essentially the driving force in developing sufficiently accurate laminated plate theories during last few decades. A methodology based on shell elements, to study the electromagnetic and thermal behavior of multilayered anisotropic conductive composite materials was presented by Bensaid et al. (2006). The anisotropic behavior and orientation of each layer of the composite

[4] `www.ansys.com`

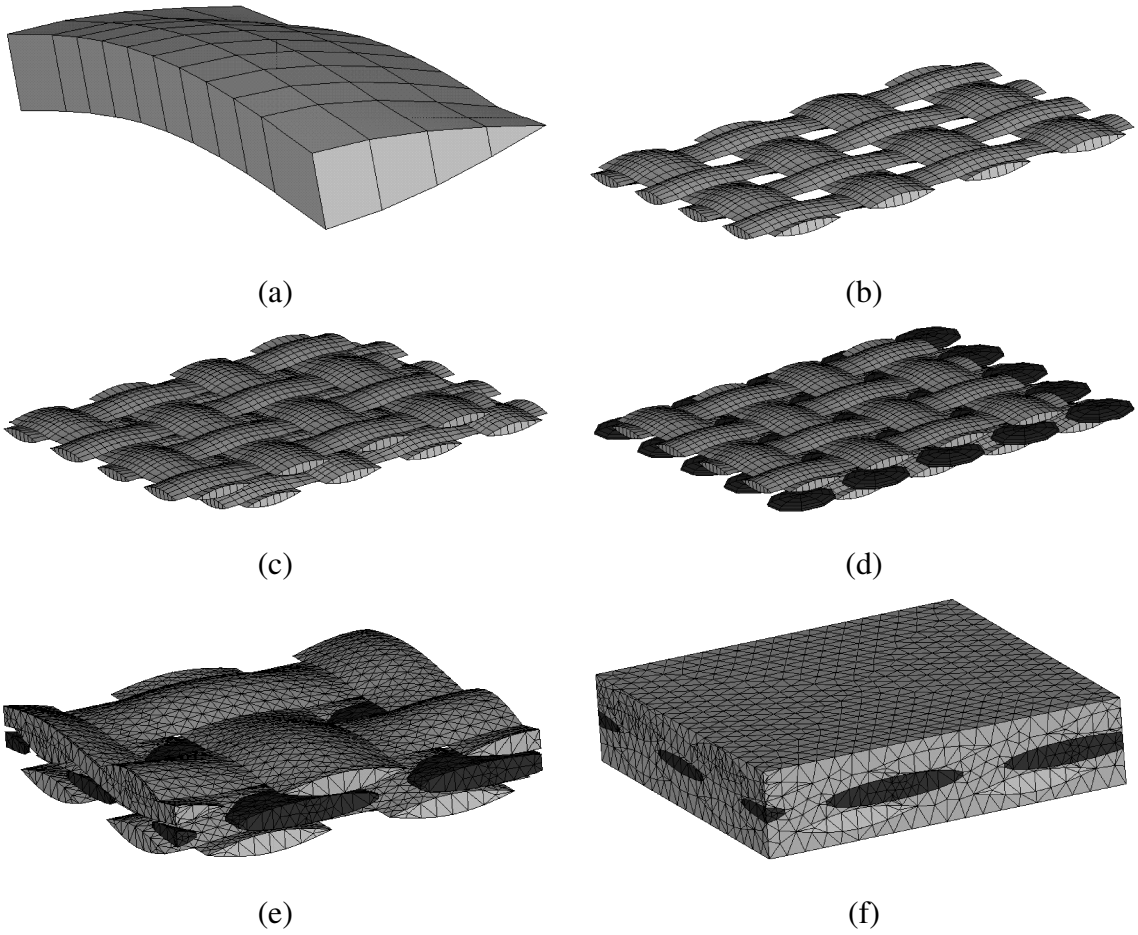

Figure 4.8: Finite element mesh generation: (a) Primitive volume, (b) one layer of reinforcements,(c) two layers of reinforcements, (d) two layers of reinforcements with voids, (e) FEM mesh of tows and voids, (f) FEM mesh of SEPUC

material has been taken into account.

If the effective properties of the single plies are derived then the elementary thermomechanics can be also applied to get the homogenized parameters of the laminate (Fig. 4.9) created from the given amount (M) of laminas. For convenience, the orthotropic properties of each layer are considered with the principal axes of orthotropy coinciding with the global coordinate system. For the longitudinal directions (X_1, X_2) the prescribed macroscopic heat flux Q_l have to fulfil for each considered orientation the equilibrium condition

$$Q_l = \sum_{m=1}^{M} c_m \langle q_{m,l} \rangle \quad \text{with} \quad \langle g_{m,l} \rangle = \chi_{m,l} \langle h_{m,l} \rangle . \tag{4.10}$$

Assuming that average temperature gradients in all layers of the composite are equal provides

the equation for homogenized thermal conductivity (the rule of mixture)

$$\chi_l = \sum_{m=1}^{M} c_m \chi_{m,l}. \tag{4.11}$$

Next, suppose that the macroscopic transverse normal heat flux Q_t is prescribed. The thermo-mechanics law requires that the total resistivity R_t must be equal to the sum of the transverse resistivity of each layer $(R_{m,t})$

$$R_t = \sum_{m=1}^{M} R_{m,t}. \tag{4.12}$$

Using the elementary definition of thermal resistivity

$$R_t = \frac{\sum_{m=1}^{M} B_m}{\chi_t} \quad \text{and} \quad R_{m,t} = \frac{B_m}{\chi_{m,t}}, \tag{4.13}$$

we get (the inverse rule of mixture) after some algebra

$$\frac{1}{\chi_t} = \sum_{m=1}^{M} \frac{c_m}{\chi_{m,t}}. \tag{4.14}$$

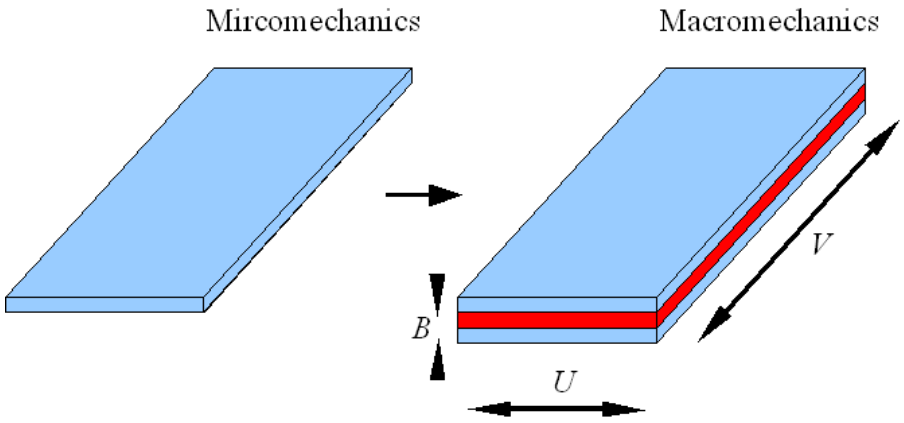

Figure 4.9: Micromechanics and macromechanics

To determine the effective mechanical properties of laminates the more sophisticated approach has to be employed. Such approach can be found in (Milton, 2002) where the solution to the field equation is used. Note that the fields vary only in the direction of lamination. The

effective stiffness tensor $\mathbf{L}$ is then evaluated by means of the separated blocks comprised in matrices (Eq. (4.15)) for the stacking sequence of layers in the direction of a global axis X_1.

$$\boldsymbol{K}_{11}^{m} = \begin{pmatrix} L_{1111}^{m} & \sqrt{2}L_{1113}^{m} & \sqrt{2}L_{1112}^{m} \\ \sqrt{2}L_{1113}^{m} & 2L_{1313}^{m} & 2L_{1312}^{m} \\ \sqrt{2}L_{1112}^{m} & 2L_{1312}^{m} & 2L_{1212}^{m} \end{pmatrix},$$

$$\boldsymbol{K}_{12}^{m} = \begin{pmatrix} L_{1122}^{m} & L_{1133}^{m} & \sqrt{2}L_{1123}^{m} \\ \sqrt{2}L_{2213}^{m} & \sqrt{2}L_{3313}^{m} & 2L_{2313}^{m} \\ \sqrt{2}L_{2212}^{m} & \sqrt{2}L_{3312}^{m} & 2L_{2312}^{m} \end{pmatrix},$$

$$\boldsymbol{K}_{22}^{m} = \begin{pmatrix} L_{2222}^{m} & L_{2233}^{m} & \sqrt{2}L_{2223}^{m} \\ L_{2233}^{m} & L_{3333}^{m} & \sqrt{2}L_{3323}^{m} \\ \sqrt{2}L_{2223}^{m} & \sqrt{2}L_{3323}^{m} & L_{2323}^{m} \end{pmatrix}, \tag{4.15}$$

where $L_{\bullet}^{m}$ stands for elements of a stiffness tensor $\mathbf{L}^{m}$ belonging to individual layers. The associated block of effective tensor are given by the expressions

$$\begin{aligned} \boldsymbol{K}_{11}^{L} &= \| \left(\boldsymbol{K}_{11}^{m}\right)^{-1} \|^{-1}, \\ \boldsymbol{K}_{12}^{L} &= \| \left(\boldsymbol{K}_{11}^{m}\right)^{-1} \|^{-1} \| \left(\boldsymbol{K}_{11}^{m}\right)^{-1} \boldsymbol{K}_{12}^{m} \|, \\ \boldsymbol{K}_{22}^{L} &= \| \boldsymbol{K}_{22}^{m} - \boldsymbol{K}_{21}^{m} \left(\boldsymbol{K}_{11}^{m}\right)^{-1} \boldsymbol{K}_{12}^{m} \| + \\ &\quad \| \boldsymbol{K}_{21}^{m} \left(\boldsymbol{K}_{11}^{m}\right)^{-1} \| \| \left(\boldsymbol{K}_{11}^{m}\right)^{-1} \|^{-1} \| \left(\boldsymbol{K}_{11}^{m}\right)^{-1} \boldsymbol{K}_{12}^{m} \|, \end{aligned} \tag{4.16}$$

where $\| \cdot \|$ stands for the weighted arithmetic mean over the thickness of layers and $\boldsymbol{K}_{21}^{m} = \left(\boldsymbol{K}_{12}^{m}\right)^{\mathsf{T}}$.

Assume that the Voight notation is used and the layers are characterized by orthotropic stiffness matrices $[\mathsf{L}^{m}]$. After some algebra non-zero elements of the effective stiffness matrix $[\mathsf{L}]$ are then provided for the laminate in the stacking sequence aligned with the global axis X_3 (Fig. 4.9) as

$$\begin{aligned} L_{11} &= \| L_{11}^{m} - \left(L_{13}^{m}\right)^{2} / L_{33}^{m} \| + \| L_{13}^{m} / L_{33}^{m} \|^{2} \| 1 / L_{33}^{m} \|^{-1} \\ L_{22} &= \| L_{11}^{m} - \left(L_{23}^{m}\right)^{2} / L_{33}^{m} \| + \| L_{23}^{m} / L_{33}^{m} \|^{2} \| 1 / L_{33}^{m} \|^{-1} \\ L_{12} &= \| L_{12}^{m} - L_{13}^{m} L_{23}^{m} / L_{33}^{m} \| + \| L_{13}^{m} / L_{33}^{m} \| \| L_{23}^{m} / L_{33}^{m} \| \| 1 / L_{33}^{m} \|^{-1} \\ L_{13} &= \| 1 / L_{33}^{m} \|^{-1} \| L_{13}^{m} / L_{33}^{m} \|, \quad L_{23} = \| 1 / L_{33}^{m} \|^{-1} \| L_{23}^{m} / L_{33}^{m} \| \\ L_{33} &= \| 1 / L_{33}^{m} \|^{-1}, \quad L_{44} = \| 1 / L_{44}^{m} \|^{-1}, \quad L_{55} = \| 1 / L_{55}^{m} \|^{-1} \\ L_{66} &= \| L_{66}^{m} \| \end{aligned} \tag{4.17}$$

Chapter 5

EVALUATION OF EFFECTIVE MATERIAL PROPERTIES

Despite a significant progress in theoretical and computational homogenization methods, material characterization techniques and computational resources, the determination of overall response of structural textile composites still remains an active research topic in engineering materials science (Cox and Yang, 2006). From a myriad of modeling techniques developed in the last decades (see e.g. review papers (Cox and Flanagan, 1997; Chung and Tamma, 1999; Lomov et al., 2007)), it is generally accepted that detailed discretization techniques, and the Finite Element Method (FEM) in particular, remain the most powerful and flexible tools available. The major weakness of these methods, however, is the fact that their accuracy crucially depends on a detailed specification of the complex microstructure of a three-dimensional composite, usually based on two-dimensional micrographs of material samples, e.g. (Wentorf et al., 1999; Hivet and Boisse, 2005; Barbero et al., 2006; Lomov et al., 2007, and reference therein). Clearly, such a step is to a great extent complicated by *random* imperfections resulting from technological operations (Pastore, 1993; Yurgartis et al., 1993), which are difficult to be incorporated to a computational model in a well-defined way. If only the overall, or macroscopic, response is the important physical variable, it is sufficient to introduce structural imperfections in a cumulative sense using one of the prominent averaging schemes such as Voight/Reuss bounds (Yushanov and Bogdanovich, 1998) or the Mori-Tanaka methods (Skoček et al., 2008). When, on the other hands, details of local stress and strain fields are required, it is convenient to characterize the mesoscopic material heterogeneity by introducing the concept of SEPUC.

While application of PUCs in problems of strictly periodic media has a rich history, their introduction in the field of random or imperfect microstructures is still very much on the frontier, despite the fact that the roots for incorporating basic features of random microstructures into the formulation of a PUC were planted already in mid 1990s by Povirk (1995). More rigorous extension presented in (Zeman and Šejnoha, 2001), see also recent work (Ze-

man and Šejnoha, 2007) for an overview, gave then rise to what we now call the concept of Statistically Equivalent Periodic Unit Cell (SEPUC). In contrast with traditional approaches, where parameters of the unit cell model are directly measured from available material samples, the SEPUC approach is based on their statistical characterization. In particular, the procedure involves three basic steps (Zeman and Šejnoha, 2007):

- To capture the essential features of the heterogeneity pattern, the microstructure is characterized using appropriate statistical descriptors. Such data is essentially the only input needed for the determination of a unit cell.

- A geometrical model of a unit cell is formulated and its key parameters are identified. Definition of a suitable unit cell model is a modeling assumption made by a user, which sets the predictive capacities of SEPUC for an analyzed material system.

- Parameters of the unit cell model are determined by matching the statistics of the complex microstructure and an idealized model, respectively. Due to multi-modal character of the objective function, soft-computing global optimization algorithms are usually employed to solve the associated problem.

It should be emphasized that the introduced concept is strictly based on the geometrical description of random media and as such it is closely related to previous works on random media reconstruction, in particular to the Yeong-Torquato algorithm outlined in (Yeong and Torquato, 1998a,b). Such an approach is fully generic, i.e. independent of a physical theory used to model the material response. If needed, additional details related to the simulation goals can be incorporated into the procedure without major difficulties, e.g. (Bochenek and Pyrz, 2004; Kumar et al., 2006), but of course at the expense of computational complexity and the loss of its generality.

In the work of Zeman and Šejnoha (2004a), the authors studied the applicability of the SEPUC concept for the construction of a single-layer unit cell reflecting selected imperfections typical of textile composites. A detailed numerical studies, based on both microstructural criteria and homogenized properties, revealed that while a single-ply unit cell can take into account non-uniform layer widths and tow undulation, it fails to characterize inter-layer shift and nesting. Therefore, we propose an extension of the original model allowing us to

address such imperfections, which have a strong influence on the overall response of textile composites (Woo and Whitcomb, 1997; Jekabsons and Byström, 2002; Lomov et al., 2003). A brief summary of the procedure for the determination of the two-ply SEPUC for woven composites was given in Section 4.1.

Such extensions, however, are hardly sufficient particularly in view of a relatively high intrinsic porosity of C/C composites, which are in the center of our current research efforts. It has been demonstrated (Tomková et al., 2008) that unless this subject is properly addressed highly inadequate results are obtained, regardless of how "exact" the geometrical details of the mesostructure are represented by the computational model. Unfortunately, the perceptible complexity of the porous phase seen also in Fig. 1.5(Macro-scale) requires some approximations. While densely packed transverse cracks affect the homogenized properties of the fiber tow through a hierarchical application of the Mori-Tanaka averaging scheme (Section 5.1), large inter-tow vacuoles (crimp voids) attributed to both insufficient impregnation and thermal treatment are introduced directly into the originally void-free SEPUC in a discrete manner.

Not only microstructural details but also properties of individual composite constituents have a direct impact on the quality of numerical predictions. Information supplied by the manufacturer are, however, often insufficient. Moreover, the carbon matrix of the composite has properties dependent on particular manufacturing parameters such as the magnitude and durations of the applied temperature and pressure. Experimental derivation of some of the parameters is therefore needed. In connection with the elastic properties of the fiber and matrix, the nanoindentation tests performed directly on the composite were discussed in Chapter 3 together with the determination of the necessary microstructural parameters mentioned already in the previous paragraphs.

Still, most of the work presented in this thesis is computational. Recall, a brief summary of the procedure for the determination of the two-ply SEPUC for woven composites given in Section 4.1. Numerical evaluation of effective elastic moduli and thermal conductivities, the most classical subject in micromechanics, is described in the following sections in support of the proposed concept of SEPUC in the light of multi-layered C/C composites. Section 5.2.1 is reserved for the verification of the optimization algorithm, validation of the extraction of geometrical and material parameters. To that end, the heat conduction and

classical elasticity homogenization problems are examined with the results corroborated by available experimental measurements.

Similarities between heat conduction and elasticity allow us to adapt equations presented in Section 2.1.1.4 for the determination of the effective stiffness matrices. For clear notation, matrix representations of symmetric fourth-order tensors $[\mathsf{L}]$, $[\mathsf{A}^{\epsilon}]$ are replaced by $\boldsymbol{L}$, $\boldsymbol{A}^{\epsilon}$ in the effective property evaluation process described as follows.

5.1 Mori-Tanaka analysis

A general awareness of the need for incorporating the porous phase in the predictions of overall response of C/C composites has been manifested in several recent works. While all microstructural details were properly identified, the actual analysis was limited to either unidirectional fiber composites represented here by individual yarns (Tsukrov et al., 2005; Piat et al., 2007b,a) or finite element simulations of entire laminate performed in two-dimensional (2D) environment only (Tomková et al., 2008). An extension of this topic taking into the characteristic three-dimensional (3D) structure of C/C textile composites is presented in this work. The formulation given here is in the spirit of multi-scale analysis discussed in (Tomková et al., 2008) combined with the application of the MT method to the prediction of effective elastic properties of C/C composite presented in (Skoček et al., 2008).

The ordering of this section follows the concept of the assumed uncoupled multi-scale homogenization approach in which the results derived from the homogenization step on a lower scale are used as an input to the same analysis performed on the upper scale, see Chapter 4. Following Tomková et al. (2008) and Böhm (2007) three particular scales are examined. The level of fiber tow evident from Fig. 4.2 is treated first. The next section examines various geometrical scenarios encountered at the level of textile ply, see Fig. 1.1. Next section then provides the estimates of the effective thermal conductivities of the laminate and compares those with the available experimental measurements. Last section is focused on discussion and conclusions.

All calculations presented in this section are performed by means of $\mathbf{HE_LP}$ program, see Appendix B for more details.

5.1.1 Micro-scale

The proposed multi-scale homogenization scheme starts on the micro-scale. The material parameters of individual phases are stored in Tabs. 3.1 and 3.2.

5.1.1.1 Effective conductivities of fiber matrix composites

Fig. 4.2(b) shows a representative section of the fiber matrix composite taken from the fiber tow in Fig. 4.2(a). Based on the previous studies (Zeman and Šejnoha, 2001; Šejnoha and Zeman, 2002; Šejnoha et al., 2004, to cite a few) such a composite can be quantified as ergodic, statistically homogeneous with a random distribution of fibers having the volume fraction of approximately 68%. In the MT scheme the effective properties follow from the solution of an auxiliary problem where an infinite cylinder of a circular cross-section with semi-axes $\xi_1 \to \infty,\ \xi_2 = \xi_3$ (the x_1 axis assumed in the fiber direction) is embedded into an infinite isotropic matrix. In this particular case the effective thermal conductivity matrix given by Eq. (2.26) simplifies for two phase composite (index 1 is reserved for matrix and index 2 for inhomogeneity) as

$$\boldsymbol{\chi}^{\mathsf{MT}} = \boldsymbol{\chi}_1 + c_2 \left(\boldsymbol{\chi}_2 - \boldsymbol{\chi}_1\right) \boldsymbol{A}_2^{\mathsf{MT}}, \tag{5.1}$$

where (see Section 2.1.1.4)

$$\boldsymbol{A}_2^{\mathsf{MT}} = \boldsymbol{A}_2^{\mathsf{dil}} \left[c_1 \boldsymbol{I} + c_2 \boldsymbol{A}_2^{\mathsf{dil}}\right]^{-1} \quad \text{and} \quad \boldsymbol{A}_2^{\mathsf{dil}} = \left[\boldsymbol{I} - \boldsymbol{S}\boldsymbol{\chi}_1^{-1} \left(\boldsymbol{\chi}_1 - \boldsymbol{\chi}_2\right)\right]^{-1}. \tag{5.2}$$

An explicit form of $\boldsymbol{S}$ for this particular case of aligned circular fibers in an isotropic matrix is available in (Hatta and Taya, 1986).

Formal similarity between heat conduction and elasticity problems then readily provides

$$\boldsymbol{L}^{\mathsf{MT}} = \boldsymbol{L}_1 + c_2 \left(\boldsymbol{L}_2 - \boldsymbol{L}_1\right) \boldsymbol{A}_2^{\mathsf{MT},\boldsymbol{\varepsilon}}, \tag{5.3}$$

where $\boldsymbol{A}_2^{\mathsf{MT},\boldsymbol{\varepsilon}}$ denotes the concentration factor for elasticity. The needed Eshelby tensor can be found in (Mura, 1987). The resulting homogenized properties then appear in Tabs. 5.2 and 5.3.

5.1.1.2 Effective conductivities of homogenized porous tow

Having derived the effective properties of the fiber matrix composite we proceed with the second homogenization step to account for the porous phase. As evident in Fig. 4.2(a), several distinct shapes of voids can be identified. It is certainly out of the question to treat each void separately. Therefore, in the present study, they are all combined into a single equivalent inclusion resembling an elliptic cylinder. Here, the cylinder is embedded into a transversely isotropic matrix.

However, since the S_{11} component of $\boldsymbol{S}$ is equal to zero, the solution of an elliptic cylinder in an isotropic matrix summarized in (Hatta and Taya, 1986) is again applicable. This results in the same form of estimate of the effective conductivity matrix $\boldsymbol{\chi}^{\mathsf{MT}}$ as given by Eq. (5.1).

Nevertheless, there is still one open problem associated with the shape of the elliptical cross-section. Clearly, since the equivalent inclusion represents all possible shapes of voids, it can hardly be determined directly from the images of real composites such as the one in Fig. 4.2(a). Instead, to solve this particular problem, we exploited the results of effective conductivities available from the finite element (FE) simulations carried out in (Tomková et al., 2008). In particular, the optimal aspect ratio ξ_2/ξ_3 ($\xi_1 \to \infty$) of the elliptical cross-section was found by matching the effective material properties derived from both the MT method and FE solutions. Because axial direction is not affected by the change of ξ_2/ξ_3 ratio, only in-plane thermal conductivities were considered in the formulation of the objective function

$$\mathcal{O}(\xi_2, \xi_3) = \max_{i=2,3} |\chi_{ii}^{\mathsf{FEM}} - \chi_{ii}^{\mathsf{MT}}| \tag{5.4}$$

plotted in Fig. 5.1 for illustration.

Note that volume fractions of fibers and air voids used in (Tomková et al., 2008) differs from the fractions presented by Černý et al. (2000) which are utilized in present study. Therefore, the volume ratio of fibers $c_f = 0.55$ and voids $c_v = 0.12$ (Tomková et al., 2008) are employed only for optimization process (Tab. 5.1). Furthermore, both direct comparison with FE element predictions and the values of relative error $\mathcal{O}(\xi_2, \xi_3)$, also stored in Tab. 5.1, clearly show a significance in properly choosing the shape of the cross-section of the equivalent elliptic cylinder. Thereby, to make the analysis more robust, an empirical re-

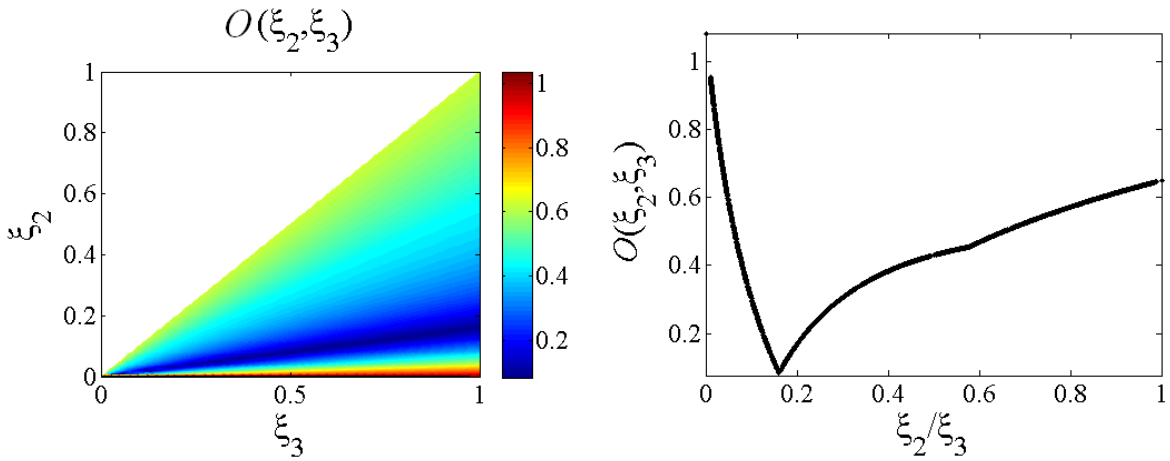

(a) (b)

Figure 5.1: Evolution of the objective function as a function of the aspect ratio

lation between the observed porosity and representative equivalent inclusion is needed. This particular topic enjoys our current research interest. The present approach is verified by the comparison of the predicted and measured longitudinal moduli shown in Tab. 5.3. The resulting effective thermal conductivities provided by the proposed two-step homogenization scheme are stored in Tab. 5.2. (Note that the fiber volume fraction c_f is estimated from Fig. 4.2(b), i.e. the tow without the pore phase, while the volume fraction of voids c_v stands for the total volume of voids in the fiber tow in Fig. 4.2(a)).

Table 5.1: Effective thermal conductivities $[\mathrm{Wm^{-1}K^{-1}}]$ of the fiber tow for optimization

Material	Equivalent inclusion		Thermal conductivity	$E(\xi_2,\xi_3)$
	fiber ($c_f = 0.55$)	void ($c_v = 0.12$)	$\chi_{11}, \chi_{22}, \chi_{33}$	
Fiber-matrix	$\infty,\ 1,\ 1$	—	22.09, 2.14, 2.14	—
Porous tow		$\infty,\ 1,\ 1$	19.44, 1.54, 1.54	0.42
		$\infty,\ 1,\ 10$	19.44, 1.02, 1.63	0.14
(optimal)	$\rightarrow$	$\infty,\ 1.6,\ 10$	**19.44, 1.12, 1.85**	0.08
3D FEM	—		19.01, 1.12, 1.77	—

Table 5.2: Effective thermal conductivities $[\mathrm{Wm}^{-1}\mathrm{K}^{-1}]$ of the fiber tow

Material	Equivalent inclusion		Thermal conductivity
	fiber ($c_f = 0.68$)	void ($c_v = 0.066$)	$\chi_{11}, \chi_{22}, \chi_{33}$
fiber-matrix	$\infty,\ 1,\ 1$	—	25.82, 1.53, 1.53
porous tow (optimal)		$\infty,\ 1.6,\ 10$	**24.12, 1.05, 1.42**

5.1.2 Meso-scale

While unidirectional fiber matrix composites reviewed in the previous section have been of a general interest since some fifty years ago, composite systems with a formidable textile texture have received more attention from both academic and industrial communities only recently.

This section examines, at least from the geometrical point of view, the most simple representative - a plain weave textile composite. One of the earliest known computational models focusing on actual geometry of the textile ply is developed by Kuhn and Charalambides (1999). A three-dimensional idealized model and a typical cross-section are plotted in Fig. 4.4.

Although tempting, a direct application of this model is precluded by a number of imperfections and irregularities present in real systems as illustrated in Figs. 1.1 and 1.2(b). These include a non-uniform waviness, mutual shift of individual yarns from layer to layer and most importantly a non-negligible porosity. Unlike finite element simulations which enable incorporating most of these imperfections directly through the formulation of a certain statistically equivalent periodic unit cell (Zeman and Šejnoha, 2004a; Šejnoha and Zeman, 2008), the MT method has only limited means which are, nevertheless, still sufficient when quick estimates of the effective "bulk" response is needed. These will be discussed next in the framework of the two-step homogenization procedure examined already in the previous section.

Table 5.3: Effective elastic properties. Comparison of MT and measured (EXP) results (Černý et al., 2000). Young's and shear moduli are given in [GPa]

Parameter	Fiber-matrix (MT)	Porous tow (MT) (optimal)	Porous tow (EXP)
E_{11}	207.5	**193.8**	≈ 200
G_{12}	11.1	**10.3**	≈ 11.5
E_{22}	15.7	**8.0**	—
E_{33}	15.7	**14.3**	—
G_{13}	11.1	**7.4**	—
G_{23}	5.8	**4.0**	—
ν_{12}	0.23	**0.23**	—
ν_{13}	0.23	**0.23**	—
ν_{23}	0.35	**0.38**	—
Equivalent inclusion	fiber ($c_f = 0.68$) $\infty,\ 1,\ 1$	void ($c_v = 0.066$) $\infty,\ 1.6, 10$	—

5.1.2.1 Effective properties of plain weave textile composite ply

Consider a simple plain weave fabric ply in the absence of porous phase (Fig. 4.4). At this level, the carbon fiber tow is treated as a homogeneous phase with known material properties bonded again to an isotropic carbon matrix. In order to address the influence of various geometrical flaws, the approach proposed in (Skoček et al., 2008) is adopted. This involves:

1. Determination of an ideal geometrical model to asses the volume fraction of the fiber tow.

2. Determination of the optimal shape of an equivalent ellipsoidal inclusion substituting the fiber tow in the solution of the Eshelby problem.

3. Proper evaluation of orientation dependent quantities from Eq. (5.16) to account for a non-uniform waviness along the fiber tow path.

Ideal geometrical model

The model described in Section 4.3 is utilized. To formulate one particular "ideal" representative, a tedious image analysis of a number of sections of a real textile ply such as the one in Fig. 1.1(a) was carried out. The averages of the basic geometrical parameters presented in Tab. 5.4 are used to construct the required geometrical model. Note that this geometry provides the volume fraction of tows equal to 0.51.

Table 5.4: Quantification of PUC1 parameters (Tomková and Košková, 2004; Skoček et al., 2008)

Statistics $[\mu m]$	a	h	b	g
Average (avg)	2250	300	150	400
Standard deviation (std)	155	50	20	105

Optimal shape of the equivalent ellipsoidal inclusion

Bearing in mind certain randomness in the geometry of a single ply unit cell, Fig. 4.3(a), it is possible to derive a certain statistically equivalent ellipsoidal inclusion, for which the macroscopic estimates are reasonably close to FE simulations for a certain range of parameters a, b, g, h.

An extensive numerical study was performed in (Skoček et al., 2008) to conceive how the Mori-Tanaka predictions are influenced by a "random" deviation of basic geometrical parameters of real systems from their ideal representative. The results revealed a certain correlation between the model parameters and "optimal" shape of an equivalent ellipsoidal inclusion characterized by three semi-axes (ξ_1, ξ_2, ξ_3). When setting $\xi_1 = 1$ (recall that the Eshelby solution depends only on the mutual ratio of the ellipsoid semi-axes), it was concluded that the ξ_2 parameter is strongly correlated with g/a ratio, while it is almost independent of b/a value. An analogous trend could be observed between ξ_3 and b/a parameter. For the present material system the three semi-axis $\xi_1 = 1, \xi_2 = 0.1, \xi_3 = 0.01$, characterizing the shape of the ellipsoidal inclusion, were found optimal regardless of the type of the homogenization problem, see Fig. 5.2. Note that the objective functions are defined

according to Skoček et al. (2008) as

$$\mathcal{O}(\xi_2, \xi_3) = \max_{i,j=1,\dots,6} |L_{ij}^{\mathsf{FEM}} - L_{ij}^{\mathsf{MT}}| \tag{5.5}$$

for elasticity and

$$\mathcal{O}(\xi_2, \xi_3) = \max_{i,j=1,2,3} |\chi_{ij}^{\mathsf{FEM}} - \chi_{ij}^{\mathsf{MT}}| \tag{5.6}$$

for conduction problem.

Further to this matter, searching for an optimal shape of the equivalent inclusion for various geometries permitted us to relate the values of ξ_2, ξ_3 axes, given $\xi_1 = 1$, to g/a and b/a ratios, respectively, see also discussions in (Skoček et al., 2008) and (Vorel and Šejnoha, 2009). Therefore, knowing at least the averages of parameters a, b and g allows us to define the shape of the ellipsoid with a relative ease as

$$\xi_2 \approx \frac{1}{7}(1 - \frac{g}{a}), \quad \xi_3 \approx \frac{1}{60}(1 - 4\frac{b}{a}). \tag{5.7}$$

Remind, however, that these relations were originally derived to match effective elastic properties. As shown in Fig. 5.2 the minimums of the error functions for elasticity and heat transfer are defined for the similar mutual ratios of the ellipsoid semi-axes. To support the validity of Eq. (5.7) by numerical results we further assumed an equivalent inclusion in the form of an infinite elliptic cylinder with elliptical cross-section estimated directly from actual cross-section of tows in the representative model giving

$$\xi_1 = \infty, \ \xi_2 = 12.3, \ \xi_3 = 1. \tag{5.8}$$

Orientation averaging

Suppose that the heterogeneity possess a certain orientation described by the orientation distribution function $g(\phi, \theta, \beta)$. A particular form of g for plain weaved composites is given in Section 4.3. In general, following (Jeong et al., 1998; Benveniste et al., 1990) and Eq. (2.2), the overall average temperature gradient for a two-phase composite with an orientation-dependent inclusion given in the global $\mathbf{X}$-coordinate system then attains the form

$$\langle \mathbf{h} \rangle = c_1 \langle \mathbf{h}_1 \rangle + c_2 \langle\langle \mathbf{h}_2 \rangle\rangle . \tag{5.9}$$

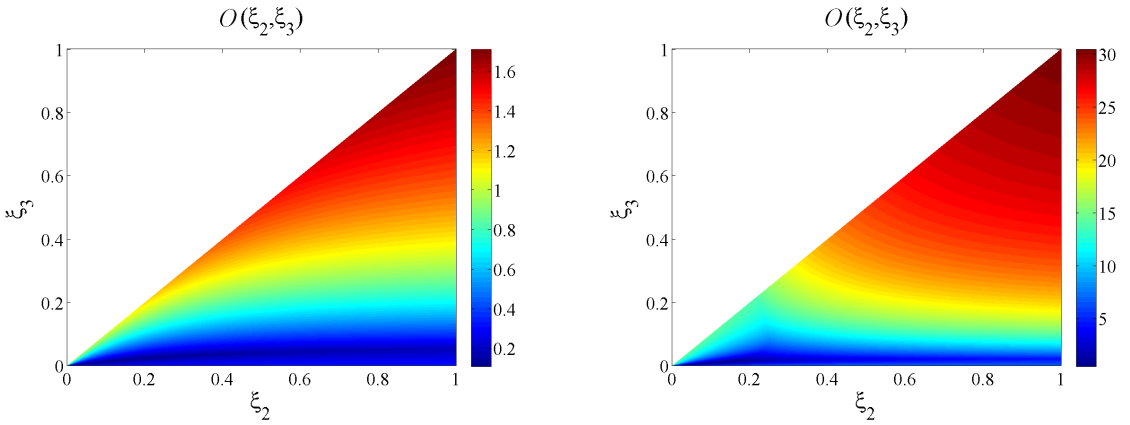

(a) (b)

Figure 5.2: Evolution of the objective function as a function of the aspect ratio: (a) Heat conduction problem, (b) elasticity

Recall that c_r is the volume fraction of the phase r, $\langle\ \rangle$ stands for the volumetric averaging and the double brackets $\langle\langle\ \rangle\rangle$ denote averaging over all possible orientations (Mayerhöfer, 2005). The vector $\mathbf{h}_2$ in Eq. (5.9) follows from standard transformation of coordinates (Eq. (4.8)) and definitions in Chapter 2 so that

$$\langle \mathbf{h}_2 \rangle = \boldsymbol{Q} \langle \mathbf{h}_2^x \rangle = \boldsymbol{Q} \boldsymbol{A}_2^{\mathsf{dil},x} \boldsymbol{Q}^{\mathsf{T}} \langle \mathbf{h}_1 \rangle = \boldsymbol{A}_2^{\mathsf{dil}} \langle \mathbf{h}_1 \rangle , \tag{5.10}$$

where the upper index x denotes the quantity in the local coordinate system.

Next, suppose that the local temperature gradient $\mathbf{h}_2$ is expressed in terms of the prescribed macroscopically uniform temperature gradient as written in Eq. (2.24). Clearly, the orientation average of $\mathbf{h}_2$ then follows from

$$\langle\langle \mathbf{h}_2 \rangle\rangle = \left\langle\left\langle \boldsymbol{A}_2^{\mathsf{dil}} \right\rangle\right\rangle \langle \mathbf{h}_1 \rangle = \left\langle\left\langle \boldsymbol{A}_2^{\mathsf{MT}} \right\rangle\right\rangle \mathbf{H}, \tag{5.11}$$

which, recall Section 2.1.1.4, gives

$$\left\langle\left\langle \boldsymbol{A}_2^{\mathsf{MT}} \right\rangle\right\rangle = \left\langle\left\langle \boldsymbol{A}_2^{\mathsf{dil}} \right\rangle\right\rangle \left[c_1 \boldsymbol{I} + c_2 \left\langle\left\langle \boldsymbol{A}_2^{\mathsf{dil}} \right\rangle\right\rangle \right]^{-1} . \tag{5.12}$$

Combining Eqs. (5.9) and (5.11) further provides

$$c_1 \langle \mathbf{h}_1 \rangle = \left[\boldsymbol{I} - c_2 \left\langle\left\langle \boldsymbol{A}_2^{\mathsf{MT}} \right\rangle\right\rangle \right] \mathbf{H}. \tag{5.13}$$

In analogy to Eq. (5.9), the volume average of the overall heat flux is provided by

$$\langle \mathbf{q} \rangle = c_1 \langle \mathbf{q}_1 \rangle + c_2 \langle\langle \mathbf{q}_2 \rangle\rangle . \tag{5.14}$$

Then, define an overall conductivity matrix $\boldsymbol{\chi}$ in the fixed coordinate system $\mathbf{X}$ and write Eq. (5.14) as

$$\boldsymbol{\chi}^{\mathsf{MT}} \mathbf{H} = c_1 \boldsymbol{\chi}_1 \langle \mathbf{h}_1 \rangle + c_2 \langle\langle \boldsymbol{\chi}_2 \mathbf{h}_2 \rangle\rangle . \tag{5.15}$$

Introducing Eqs. (2.24) and (5.13) into Eq. (5.15) finally yields

$$\boldsymbol{\chi}^{\mathsf{MT}} = \boldsymbol{\chi}_1 + c_2 \left[\langle\langle \boldsymbol{\chi}_2 \boldsymbol{A}_2^{\mathsf{MT}} \rangle\rangle - \boldsymbol{\chi}_1 \langle\langle \boldsymbol{A}_2^{\mathsf{MT}} \rangle\rangle \right] . \tag{5.16}$$

Next, let $\boldsymbol{D}$ represents an orientation dependent quantity in Eq. (5.16)

$$\langle\langle \boldsymbol{D} \rangle\rangle = \langle\langle \boldsymbol{\chi}_2 \boldsymbol{A}_2^{\mathsf{MT}} \rangle\rangle - \boldsymbol{\chi}_1 \langle\langle \boldsymbol{A}_2^{\mathsf{MT}} \rangle\rangle , \tag{5.17}$$

written, for the warp system, as

$$\langle\langle \boldsymbol{D}_{\mathsf{warp}} \rangle\rangle = \int_{-\alpha}^{\alpha} g(\phi, \theta, \beta) \boldsymbol{D}(0, \theta, 0) \, \mathrm{d}\theta, \tag{5.18}$$

and similarly for the weft system we get

$$\langle\langle \boldsymbol{D}_{\mathsf{weft}} \rangle\rangle = \int_{-\alpha}^{\alpha} g(\phi, \theta, \beta) \boldsymbol{D}(\frac{\pi}{2}, \theta, 0) \, \mathrm{d}\theta. \tag{5.19}$$

Finally, following the work by (Skoček et al., 2008), the resulting homogenized conductivity matrix given by Eq. (5.16) then becomes

$$\boldsymbol{\chi}^{\mathsf{MT}} = \boldsymbol{\chi}_1 + \frac{c_2}{2} \left[\langle\langle \boldsymbol{D}_{\mathsf{warp}} \rangle\rangle + \langle\langle \boldsymbol{D}_{\mathsf{weft}} \rangle\rangle \right] . \tag{5.20}$$

The homogenized stiffness matrix can be written in the same manner as

$$\boldsymbol{L}^{\mathsf{MT}} = \boldsymbol{L}_1 + \frac{c_2}{2} \left[\langle\langle \boldsymbol{D}^{\boldsymbol{\varepsilon}}_{\mathsf{warp}} \rangle\rangle + \langle\langle \boldsymbol{D}^{\boldsymbol{\varepsilon}}_{\mathsf{weft}} \rangle\rangle \right] . \tag{5.21}$$

One may also suggest to model the plain weave fabric as a three-phase composite with warp and weft systems of yarns being considered as two distinct phases. The homogenized matrices then attain a slightly different forms

$$\begin{aligned} \boldsymbol{\chi}^{\mathsf{MT}} \quad = \quad & \boldsymbol{\chi}_1 + \frac{c_2}{2} \left\{ \left[\langle\langle \boldsymbol{\chi}_{\mathsf{warp}} \boldsymbol{T}_{\mathsf{warp}} \rangle\rangle - \boldsymbol{\chi}_1 \langle\langle \boldsymbol{T}_{\mathsf{warp}} \rangle\rangle \right] + \left[\langle\langle \boldsymbol{\chi}_{\mathsf{weft}} \boldsymbol{T}_{\mathsf{weft}} \rangle\rangle - \boldsymbol{\chi}_1 \langle\langle \boldsymbol{T}_{\mathsf{weft}} \rangle\rangle \right] \right\} \\ & \left\{ c_1 \boldsymbol{I} + \frac{c_2}{2} \left[\langle\langle \boldsymbol{T}_{\mathsf{warp}} \rangle\rangle + \langle\langle \boldsymbol{T}_{\mathsf{weft}} \rangle\rangle \right] \right\}^{-1} , \end{aligned} \tag{5.22}$$

and

$$\begin{aligned}\boldsymbol{L}^{\mathsf{MT}} &= \boldsymbol{L}_1 + \frac{c_2}{2}\left\{\left[\left\langle\!\left\langle \boldsymbol{L}_{\mathsf{warp}}\boldsymbol{T}^{\boldsymbol{\varepsilon}}_{\mathsf{warp}}\right\rangle\!\right\rangle - \boldsymbol{L}_1\left\langle\!\left\langle \boldsymbol{T}^{\boldsymbol{\varepsilon}}_{\mathsf{warp}}\right\rangle\!\right\rangle\right] + \left[\left\langle\!\left\langle \boldsymbol{L}_{\mathsf{weft}}\boldsymbol{T}^{\boldsymbol{\varepsilon}}_{\mathsf{weft}}\right\rangle\!\right\rangle - \boldsymbol{L}_1\left\langle\!\left\langle \boldsymbol{T}^{\boldsymbol{\varepsilon}}_{\mathsf{weft}}\right\rangle\!\right\rangle\right]\right\} \\ &\quad \left\{c_1\boldsymbol{I} + \frac{c_2}{2}\left[\left\langle\!\left\langle \boldsymbol{T}^{\boldsymbol{\varepsilon}}_{\mathsf{warp}}\right\rangle\!\right\rangle + \left\langle\!\left\langle \boldsymbol{T}^{\boldsymbol{\varepsilon}}_{\mathsf{weft}}\right\rangle\!\right\rangle\right]\right\}^{-1}, \end{aligned} \tag{5.23}$$

However, the differences in predictions provided by Eqs. (5.20) and (5.22) are, as seen in Tabs. 5.5 and 5.6, negligible.

Improvements when compared to the assumed ideal geometry are contained in the third route which allows us to introduce the non-uniform waviness and to some extent also the mutual shift of individual layers by utilizing histograms of inclination angles shown in Fig. 4.3(a). These are derived from centerlines of individual fiber tows described in detail in (Vopička, 2004). Representing the joint probability density function by these histograms, the orientation average of a certain quantity $\boldsymbol{D}(0,\psi_i,0)$, e.i. for the warp direction $(\phi = 0)$, reads

$$\left\langle\!\left\langle \boldsymbol{D}_{\mathsf{warp}}\right\rangle\!\right\rangle = \sum_{i=1}^{SV} p_i \boldsymbol{D}(0,\theta_i,0), \tag{5.24}$$

where SV denotes the number of sampling values. The discrete angles θ_i and probabilities p_i follow directly from the image analysis data. Ten such histograms associated with several sections measured along individual plies were considered. The resulting averages together with the estimates provided by the simplified distribution functions are summarized in Tabs. 5.5 and 5.6. The 3D finite element solutions of the PUC (with the material properties obtained from the MT solution on a micro-scale) are provided for a comparison. The solution of the Eshelby problem of an ellipsoidal inclusion in an isotropic matrix can be found in (Hatta and Taya, 1986; Jeong et al., 1998; Mura, 1987) or Appendix A.

5.1.2.2 Effective properties of homogenized porous matrix

When carefully observing Fig. 1.1(d) we identify three more or less periodically repeating geometries further displayed in Fig. 5.3. These segments readily confirm the need for the proposed two step homogenization procedure as the ideal representative plotted in Figs. 5.3(a,b) (already analyzed in the previous section) cannot be used to represent the entire composite. Instead, the second homogenization step is required to account for the presence of large vacuoles evident from Figs. 5.3(c-f).

Table 5.5: Effective thermal conductivities of a plain weave fabric without porosity in $[\mathrm{Wm}^{-1}\mathrm{K}^{-1}]$ (volume fraction of tows = 0.51)

Method	Fiber tow shape	Thermal conductivity					
		Eq. (5.20)		Eq (5.22)		Eqs. (5.22)&(5.24)	
		warp/weft	trans.	warp/weft	trans.	warp/weft	trans.
MT	∞, 12.3, 1	9.44	2.51	9.32	2.49	9.24	2.53
	1, 0.1, 0.01	9.42	2.55	9.29	2.52	**9.19**	**2.57**
3D FEM	—	9.24	2.71	—			

Owing to the orthogonal arrangement of tows in the ideal (representative) model the new homogenized matrix employed in the second homogenization step is no longer isotropic. Thereby, the Eshelby solutions used so far are not directly applicable. Instead, the $\boldsymbol{S}$ tensor is found by imagining an equivalent ellipsoidal inclusion in an infinite matrix being orthotropic, see Appendix A and the numerical solution of the Eshelby tensor for elasticity in (Gavazzi and Lagoudas, 1990).

With the encouraging results presented in Appendix A at hand we proceeded with the analysis of real systems. Unlike the micro-scale, the method of observation and measuring tools provided by the **LUCIA G** software (LIM, 2008) is utilized here to approximate the shape of individual vacuoles in Figs. 5.3(c-f). Since only two-dimensional (2D) images were supplied, the voids were assumed to be well approximated by an oblate spheroid defined in Tabs. 5.7,5.8 for both types of representative periodic unit cells in Figs. 5.3(d,f). To estimate the mesoscopic effective properties the voids were introduced into the homogenized matrix derived in the 1st homogenization step by combining Eqs. (5.22) and (5.24).

A word of caution, however, is appropriate when dealing with 2D images only. While the shape of the inclusion acquired from 2D images may play a minor role in final predictions of the effective properties, the volume fraction of a relevant heterogeneity also estimated from 2D images may prove much more important. This is documented in (Vorel and Šejnoha, 2009) listing the predicted effective properties of a plain weave fabric free of pores for two different volume fractions of the homogenized fiber tow. Recall that the assumed volume fraction of tows 0.51 corresponds to a representative 3D mesostructure in Fig. 4.4(b),

Table 5.6: Effective elastic properties of a plain weave fabric without porosity. Young's and shear moduli are given in [GPa] (volume fraction of tows = 0.51; 2P = Eq. (5.20); 3P = Eq. (5.22); 3PH = Eqs. (5.22)&(5.24))

Parameter	Inclusion						3D FEM
	$\infty,\ 12.3,\ 1$			$1,\ 0.1,\ 0.01$			
	2P	3P	3PH	2P	3P	3PH	
$E_{\mathsf{warp,weft}}$	62.9	61.8	61.0	62.0	60.3	**60.8**	60.4
$G_{\mathsf{warp,weft}}$	8.6	8.5	8.5	8.5	8.5	**8.5**	8.6
$\nu_{\mathsf{warp,weft}}$	0.05	0.05	0.05	0.05	0.05	**0.05**	0.06
E_{trans}	18.9	18.9	18.9	18.9	18.9	**18.9**	19.2
G_{trans}	8.1	7.5	7.8	8.1	7.6	**7.8**	7.4
ν_{trans}	0.07	0.08	0.08	0.07	0.08	**0.08**	0.07

whereas the value of 0.78 would follow from the corresponding 2D image in Fig. 5.3(b). This objective will become even more important when the porous phase is introduced into the new homogenized mesoscopic matrix.

The mesoscopic effective conductivities and elastic properties derived for individual geometries in Fig. 5.3 are summarized in Tabs. 5.7 and 5.8 for both shapes of the fiber tow. Note that the results corresponding to a representative model denoted as PUC1 are essentially those stored in Tabs. 5.5 and 5.6. Similar cells to PUC1 with the adjusted volumes of tows serve as a point of departure for the second homogenization step performed for models PUC2 and PUC3. This adjustment follows from the assumption that in all cells the volumes of tows are equal, i.e. the voids replace the phase of matrix. (The tow volume fraction (0.51) is estimated for the cell without the pore phase, while the volume fraction of voids c_v stands for the total volume of voids in the cell). For better representation of the tow paths the results derived by means of histograms are used hereafter.

5.1.3 Macro-scale

The final, clearly the most simple, step requires construction of the homogeneous laminated plate. The stacking sequence of individual periodic unit cells complies with that observed for

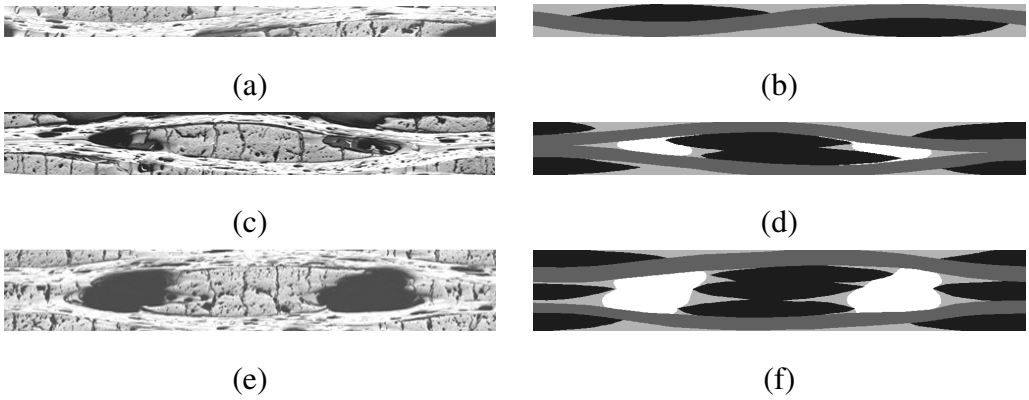

Figure 5.3: Homogenization on meso-scale: (a)-(b) PUC1 representing carbon tow-carbon matrix composite, (c)-(d) PUC2 with vacuoles aligned with delamination cracks due to slip of textile plies, (e)-(f) PUC3 with extensive vacuoles representing the parts with textile reinforcement reduction due to bridging effect in the middle ply

the actual composite sample (Tomková et al., 2008, Fig. 2), see also Fig. 1.1(d) identifying the PUC1/PUC2/PUC3/PUC1 stacking sequence. The dimensions of each ply are assumed to be the same as the size of unit cell without pores (PUC1), see Tab. 5.4.

While in-plane conductivities (warp/weft or longitudinal directions) were found from a simple arithmetic rule of mixture, the out-of-plane (transverse) conductivity followed from the inverse (geometric) rule of mixture, Section 4.4. The resulting effective thermal conductivities are available in Tab. 5.9 comparing the MT predictions and experimental measurements presented in (Boháč, 2005), see Section 3.4 for more informations. For the elastic properties the laminate theory presented by Milton (2002) is utilized (Section 4.4) and the results are stored in Tab. 5.10.

Note that the highlighted (bolt font) values of thermal conductivities stored in Tabs. 5.2–5.10 follow from what we would call an optimal or the most appropriate approach.

5.2 Finite element analysis

The effective properties of multilayered C/C plain weave composite with pores represented by the PUC (Fig. 4.7) are determined in this section. As already mentioned, the FE analysis is time consuming, but it provides us more accurate results and allows to incorporate various

Table 5.7: Effective thermal conductivities of the porous textile plies and laminates in $[\mathrm{Wm}^{-1}\mathrm{K}^{-1}]$

Fiber tow shape	Void			Thermal conductivity	
in 1st step	PUC	shape	vol. frac.	warp/weft	transverse
∞, 12.3, 1	PUC2	3, 3, 1	0.07	8.60	2.14
	PUC3	1.6, 1.6, 1	0.15	7.63	1.83
1, 0.1, 0.01	PUC2	3, 3, 1	0.07	**8.55**	**2.17**
	PUC3	1.6, 1.6, 1	0.15	**7.59**	**1.87**

intrinsic imperfections of composites (Chapters 3,4).

Suppose that the homogenized effective conductivities of the yarn are already known from an independent micromechanical analysis performed on the level of individual fibers, see previous section. The objective now is to find effective parameters on the mesoscopic level for multilayered composite.

So far, the FEM studies have been mostly focused on a treatment of shifted layers (Zeman, 2003). In this thesis an accuracy of the two-layered model of C/C composite with air voids is presented. Two approaches are utilized to validate this technique. The first is based on the treatment of a statistically equivalent periodic unit cell defined in Section 4.1. The other uses sets of input parameters generated by the **SPERM** program (Novák and Kalousková, 2008) to define representative PUCs of the composite. All the computations are performed by means of the university finite element code **FEln** where the homogenization scheme described in Section 2.2.1 is implemented.

5.2.1 SEPUC

The technique briefly described in Section 4.1 is employed to define a SEPUC. Using the image processing operations we obtain the desired parameters describing the cell. A strong nesting of individual layers as well as relative shifts in all directions are clearly visible in Fig. 3.3. Therefore, a one-layer unit cell is not a concise geometrical model of the analyzed material so that a two-layered cell is used. Owing to a numerical complexity of such a model, the SEPUC is constructed in two steps. First, the cell without air voids is con-

Table 5.8: Effective elastic properties of the porous textile plies and laminates. Young's and shear moduli are given in [GPa]

Parameter	Fiber tow shape in 1st step			
	∞, 12.3, 1		1, 0.1, 0.01	
	PUC2	PUC3	PUC2	PUC3
$E_{\text{warp,weft}}$	55.7	46.9	**55.5**	**46.8**
$G_{\text{warp,weft}}$	7.6	6.6	**7.6**	**6.6**
$\nu_{\text{warp,weft}}$	0.04	0.06	**0.04**	**0.06**
E_{trans}	15.9	13.1	**15.9**	**13.1**
G_{trans}	6.1	5.4	**6.1**	**5.4**
ν_{trans}	0.07	0.07	**0.07**	**0.07**
Equivalent inclusion	$c_v = 0.07$	$c_v = 0.15$	$c_v = 0.07$	$c_v = 0.15$
(air void)	3, 3, 1	1.6, 1.6, 1	3, 3, 1	1.6, 1.6, 1

structed by means of the optimization procedure (Fig. 4.6), see Section 4.1. The air voids are subsequently introduced into the created cells. The volume of pores equal to 5.5% is assumed. Note that this value corresponds to both the percentage determined by the image analysis and the volume used in the previous section for the laminated plate. This volume is divided between four oblate spheroids ($\xi_1 = \xi_2 > \xi_3$) accommodated between two layers (Fig. 4.7). The relative ratio of spheroid axes is chosen as high as possible to fill the space between the tows. The contemplative reader can remark that a rotation of inclusions and a general ellipsoid would depict better the real structure of the composite. However, these added parameters would complicate an automatized generation and construction of cells. This simplification is also supported by the X-ray microimages shown in Fig. 3.4 where the pores have a shape similar to an oblate spheroid and are aligned with layers of carbon tows.

The optimization algorithm was executed twenty times to verify, whether the global optimum of the problem was found. The unscaled input parameters for the optimization procedure are stored in Tab. 5.11, see Section C.3. The upper and lower bounds of each parameter are set up at 5 and 95% probability quantiles assuming the Gauss distribution function. The unscaled resulting values of the SEPUC parameters are shown in the last column of Tab. 5.11

Table 5.9: Effective thermal conductivities of the laminate $[\mathrm{Wm}^{-1}\mathrm{K}^{-1}]$

Method	Fiber tow shape	Thermal conductivity	
		warp/weft	transverse
MT (histograms)	$\infty, 12.3, 1$	8.68	2.22
	$1, 0.1, 0.01$	**8.63**	**2.25**
EXP (Boháč, 2005)	—	10	1.6

Table 5.10: Effective elastic properties of the laminate. Young's and shear moduli are given in [GPa]

Parameter	MT (histograms)		EXP (Černý et al., 2000)
	Fiber tow shape		
	$\infty,\ 12.3,\ 1$	$1,\ 0.1,\ 0.01$	
$E_{\mathsf{warp,weft}}$	55.9	**55.7**	≈ 65
$G_{\mathsf{warp,weft}}$	7.8	**7.8**	≈ 6
$\nu_{\mathsf{warp,weft}}$	0.05	**0.05**	—
E_{trans}	16.5	**16.3**	—
G_{trans}	6.5	**6.5**	—
ν_{trans}	0.07	**0.07**	—

where symbol * denotes parameters which were not involved in the optimization, compare with Tab. 4.3.

With this at hand, we proceed to the evaluation of effective properties. The SEPUC are constructed as described in Section 4.3.2. To demonstrate the porous phase influence the effective conductivity coefficients and elastic properties are evaluated for the unit cell both without and with pores. The determined homogenized properties are presented in Tabs. 5.12 and 5.13.

Table 5.11: Parameters of the periodic unit cell (Tomková and Košková, 2004; Skoček et al., 2008; Zeman and Šejnoha, 2004b)

Parameter		Avg	Std	SEPUC
a	[μm]	2250	150	2181
b	[μm]	150	20	118
g	[μm]	400	105	422
h	[μm]	300	50	251
$\Delta_{1,2}$	[μm]	0	675	288
Δ_3	[μm]	0	110	-47
pore's volume	[%]	8	3.5	5.5*
ξ_3/ξ_1	[-]	0.4	0.2	0.13*

Table 5.12: Effective thermal conductivities of the SEPUC $[\mathrm{Wm^{-1}K^{-1}}]$

Method	Pores	Thermal conductivity	
		warp/weft	transverse
FEM	excluded	9.30	2.50
(SEPUC)	included	**9.03**	**1.89**
EXP (Boháč, 2005)	—	10	1.6

5.2.2 Representative PUCs

The principal objective of this section is to confirm the hypothesis of a two-layered SEPUC with pores and to obtain rough dispersion of the effective properties. The **SPERM** program is utilized to produce ten different PUCs. The latin hypercube sampling (LHS) method implemented in this code is utilized to generate realizations of random variables from prescribed distributions. The normal distribution function is assumed for all parameters defined by their means and standard deviations, see Tab. 5.11. The correlations between the variables are considered and set up using the engineering judgement of the authors, see Tab. 5.14. Note that parameter ξ_3/ξ_1 is not generated and is determined as the highest possible value to fit the pores between the layers. The PUCs are subsequently subjected to a finite element analysis

Table 5.13: Effective elastic properties of the SEPUC. Young's and shear moduli are given in [GPa]

Parameter	FEM		EXP (Černý et al., 2000)
$E_{\text{warp,weft}}$	61.5	**60.3**	≈ 65
$G_{\text{warp,weft}}$	8.5	**8.1**	≈ 6
$\nu_{\text{warp,weft}}$	0.05	**0.05**	—
E_{trans}	15.7	**11.9**	—
G_{trans}	6.3	**5.3**	—
ν_{trans}	0.06	**0.05**	—
Pores	excluded	included	—

with the prescribed periodic boundary conditions (Novák et al., 2004) to obtain the searched effective thermal conductivities and stiffness matrices of the laminates (Tab. 5.15).

Table 5.14: Correlation matrix

	a	b	g	h	$\Delta_1 = \Delta_2$	Δ_3	pore's vol.
a	1.0	0.3	0.7	0.3	0.0	0.0	0.5
b		1.0	0.3	0.9	0.0	0.3	-0.3
g			1.0	0.3	0.0	0.0	0.0
h				1.0	0.0	-0.3	0.3
$\Delta_1 = \Delta_2$		sym.			1.0	0.0	0.0
Δ_3						1.0	0.7
pore's vol.							1.0

5.3 Conclusions

In order to realistically model complex plain weave textile laminates with three-dimensional, generally non-uniform texture of the reinforcements and significant amount of porosity we

Table 5.15: Effective thermal conductivities $[\mathrm{Wm}^{-1}\mathrm{K}^{-1}]$ and elastic properties for different PUCs. Young's and shear moduli are given in [GPa]

PUC	Thermal conductivity		Elastic properties					
	$\chi_{\mathsf{warp,weft}}$	χ_{trans}	$E_{\mathsf{warp,weft}}$	$G_{\mathsf{warp,weft}}$	$\nu_{\mathsf{warp,weft}}$	E_{trans}	G_{trans}	ν_{trans}
1	7.8	2.4	47.9	7.9	0.07	15.4	6.5	0.08
2	8.9	2.0	58.6	8.0	0.05	15.1	6.2	0.06
3	8.5	2.0	54.9	7.8	0.06	14.4	5.9	0.06
4	8.6	2.1	55.4	7.9	0.06	14.7	6.1	0.06
5	8.1	1.5	52.8	7.5	0.06	9.6	4.3	0.04
6	8.3	2.1	52.5	8.0	0.06	13.7	5.7	0.06
7	9.1	2.1	60.0	8.2	0.05	14.2	6.1	0.06
8	8.8	2.1	57.4	8.2	0.06	14.6	6.2	0.06
9	7.9	2.0	49.4	7.7	0.06	12.1	5.4	0.06
10	8.7	2.0	56.7	8.0	0.05	13.2	5.8	0.05
avg	**8.46**	**2.04**	**54.5**	**7.9**	**0.06**	**13.7**	**5.8**	**0.06**
std	0.42	0.22	3.9	0.2	0.01	1.7	0.6	0.01

advocate to consider at least three levels of hierarchy for the Mori-Tanaka solution - the level of fiber tow, the level of yarns and the level of laminate, and two levels for the FE analysis - the level of fiber tow, the level comprising both yarns and the laminate (a two-layered PUC with pores). On each level different resolutions of microstructural details are considered for the formulation of an adequate representative model. The desired macroscopic effective properties of the laminate are then estimated with regard to two basic objectives:

- to reflect the three-dimensional character of the composite at all scales,
- to predict the effective conductivities as efficiently as possible.

Unlike computationally tedious and extensive 3D finite element simulations, the Mori-Tanaka averaging scheme appears as a reasonable candidate to comply with both objectives. Not only the fully explicit format of this method but a simple extension of the Eshelby problem, at least in the case of the solution of heat conduction problem, to generally orthotropic

reference medium (homogenized composite free of pores in this particular case) favors this technique.

In this study, the hierarchical character of the analysis is presented in a totally uncoupled format. Therefore, each level is treated entirely independently purely upscaling the results from a lower to a higher scale for subsequent calculations. An "optimal" procedure, which attempts to accommodate various sources of imperfections observed in real systems is accompanied by several modifications involving mainly the meso-scale.

Based on the previous study of effective elastic properties (Zeman and Šejnoha, 2004a; Skoček et al., 2008) it was expected that at this level the "best" estimates of the effective properties using the MT method would follow from the application of Eq. (5.7) to determined the shape of an equivalent inclusion for the fiber tow representation and histograms of fiber inclination angle to proceed with the orientation averaging step. As seen in Tabs. 5.5-5.10 the shape of the fiber tow determined from the real dimensions provides also reasonable results, thus can be used for the MT analysis as well. Comparing various modifications (different types of inclusions, ideal path of the fiber tow) suggests, perhaps even intuitively, almost negligible sensitivity of the solution of the heat conduction problem to mutual interlacing of individual tows in comparison with the solution of the elasticity problem. This is mainly attributed to a relative flatness of the reinforcing yarns in individual plies of the laminate. In view of this, one may even offer the possibility of estimating the effective mesoscopic conductivities by simply assuming two systems of perpendicular fiber tows with no interlacing, thereby completely avoiding the orientation averaging step. But bear in mind that such a "drastic" simplification can hardly be generalized and is certainly not acceptable in the case of elasticity. To discriminate between various approaches is therefore difficult.

The three-dimensional two-layered PUC used for FE analysis was constructed in order to:

- reflect the three-dimensional character of the composite,
- grasp the shift of layers,
- account for significant volume of air voids,
- use restricted number of parameters by an accuracy protection of the suggested model.

As shown in this chapter, the FEM provides more accurate results compare to the MT solution. It is worthwhile mentioning that PUCs estimated on the basis of random variables (Section 5.2.2) provide less precise results (Fig. 5.4) than the SEPUC (Section 5.2.1) which gives a better picture of a real system. The slight divergence is also caused by the restricted set of the PUCs in Section 5.2.2 and the considered probability distribution of the parameter Δ_3.

Comparison with experimental measurements is in principle twofold but also inconclusive, see Fig.5.4. On the one hand, it clearly supports the use of the proposed uncoupled multi-scale approach to arrive at the predictions of the effective macroscopic thermal conductivities and elastic properties. Furthermore, at least quantitatively, the Mori-Tanaka method proved its applicability in the solution of complicated textile composites. These remarks have already been put forward in (Skoček et al., 2008) with regard to the problem of effective elastic properties.

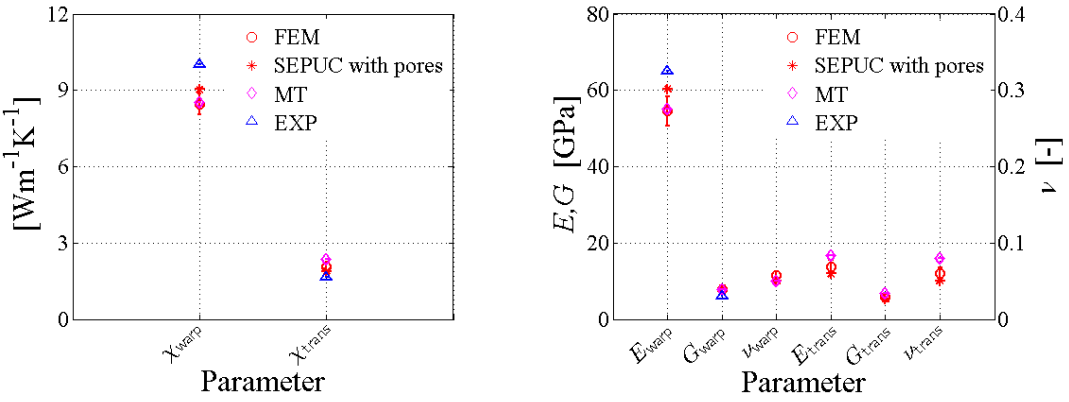

Figure 5.4: Comparison of the numerical and experimental results: (a) Coefficients of thermal conductivity, (b) elastic properties

To judge, on the other hand, the pertinence and reliability of the MT method solely by comparing the predicted and measured values, which may deny it, is certainly insufficient. While all deficiencies of the presented homogenization strategy were openly discussed, errors associated with experimental measurements were not mentioned and are not available. We should also mentioned that changes occurring in the fiber tows during the manufacturing are not clearly known and so they are not involved in this study.

In summary, focusing only on the quantitative perspective, the Mori-Tanaka method combined with popular multi-scale homogenization approach is viable and presents a suitable and efficient alternative to more precise periodic homogenization based on the finite element analysis.

Chapter 6

CONCLUSIONS AND FUTURE PERSPECTIVES

In the presented work, Benveniste's approach of the Mori-Tanaka method (Benveniste, 1987) is used as our point of departure due to its successful application to diverse heterogeneous material systems. A two-step homogenization scheme is incorporated to capture the interaction among heterogeneities.

Application of the method to the analysis of porous woven C/C composite systems involves three steps. In the first step, the parameters on micro-scale are derived. In the next step, imperfections along the fiber tow paths are taken into account by incorporating both an experimentally observed distribution of tow path angles and the joint probability density function of the simplified geometrical model. The porosity is introduced on both scales. Finally, to capture the stacking sequence of individual plies the arithmetic and inverse rules of mixture are applied for thermal conductivity problem on macro-scale and the laminate theory presented by Milton (2002) for elastic properties.

It is often desirable to derive detailed representation of the local fields rather than the volume phase averages only as provided by the Mori-Tanaka predictions. Attention is then usually given to a periodic unit cell analysis by means of the finite element method. To exploit the benefit of periodic fields, while at the same time account for uncertainties associated with real microstructure, see Fig. 1.2(b) and (Zeman and Šejnoha, 2004a; Tomková et al., 2008), the concept of statistically equivalent periodic unit cell can be used (Zeman and Šejnoha, 2007, 2004a).

As presented, reasonably accurate predictions of the overall response of a multilayered system is found from the analysis of a two-layered periodic unit cell with pores. The determination of the statistically equivalent geometrical model is based on a general methodology proposed in (Zeman and Šejnoha, 2001). In this context, the original microstructure is quantified by an appropriate (statistical) descriptor, which characterizes the most important features of the disordered microstructure. This information is subsequently used for

the definition of a simplified periodic unit cell, which optimally approximates the original microstructure in the sense of the selected statistical descriptors. Although geometrical imperfections present a distinct source of uncertainties they may prove, in comparison to a very high intrinsic porosity typical of C/C textile composites, far less important particularly from the overall response point of view.

It is also noteworthy that this approach needs much more computational effort compare with the Mori-Tanaka method, particularly when preparing the finite element model and mesh.

Finally, the comparison of numerical results with the experimental data reveals the slight discrepancy. According to the authors, this can be connected with the property changes of the individual constituents during the manufacturing process. This topic deserves another experimental treatment and should be involved into a numerical solution.

BIBLIOGRAPHY

ANSYS, I. (2005). *Documentation for ANSYS*. ANSYS, Inc. Home page: `http://www.ansys.com`.

Barbero, E., Damiani, T., and Trovillio, J. (2005). Micromechanics of fabric reinforced composites with periodic microstructure. *International Journal of Solids and Structures*, 42(9-10):2489—-2504.

Barbero, E., Trovillion, J., Mayugo, J., and Sikkil, K. (2006). Finite element modeling of plain weave fabrics from photomicrograph measurements. *Composite Structures*, 73(1):41–52.

Bensaid, S., Trichet, D., and Fouladgar, J. (2006). Electromagnetic and thermal behaviors of multilayer anisotropic composite materials. *Magnetics, IEEE Transactions on*, 32(4):995–998.

Benveniste, Y. (1987). A new approach to the application of Mori-Tanaka theory in composite materials. *Mechanics of Materials*, 6:147–157.

Benveniste, Y., Chen, T., and Dvorak, G. (1990). The effective thermal conductivity of composites reinforced by coated cyllindrically orthotropic fibers. *Journal of Applied Physics*, 67(6):2878–2884.

Billington, S. (2004). Damage-tolerant cement-based materials for performence-based erthquake engineering design: Research needs. In *Fracture Mechanics of Concrete Structures*, pages 53–60.

Bittnar, Z. and Šejnoha, J. (1996). *Numerical methods in structural mechanics*. ASCE Press and Thomas Telford, Ltd, New York and London.

Bochenek, B. and Pyrz, R. (2004). Reconstruction of random microstructures–a stochastic optimization problem. *Computational Materials Science*, 31(1–2):93–112.

Boháč, V. (2005). Measurement of thermophysical properties of C/C composite. Technical report, Slovak Academy of Science, Bratislava. In Slovak.

Böhm, H. (2007). A short introduction to basic aspects of continuum micromechanics. Technical Report 2006, Viena University of Technology.

Boshoff, W. (2007). *Time-Dependant Behaviour of Engineered Cement-Based Composites*. PhD thesis, University of Stellenbosch. Ph.D. thesis.

Boshoff, W., Mechtcherine, V., and van Zijl, G. (2009a). Characterising the time-dependant behaviour on the single fibre level of SHCC: Part 1: Mechanism of fibre pull-out creep. *Cement and Concrete Research*, 39:779–786.

Boshoff, W., Mechtcherine, V., and van Zijl, G. (2009b). Characterising the time-dependant behaviour on the single fibre level of SHCC: Part 2: The rate effects on fibre pull-out tests. *Cement and Concrete Research*, 39:787–797.

Boshoff, W. and van Zijl, G. (2007). Time-dependant response of ECC: Characterisation of creep and rate dependence. *Cement and Concrete Research*, 37:725–734.

BV., T. D. (2008). *DIANA Finite Element Analysis*.

Casal, E., Granda, M., Bermejo, J., Bonhomme, J., and Menendez, R. (2001). Influence of porosity on the apparent interlaminar shear strength of pitch-based unidirectional C-C composites. *Carbon*, 39(1):73–82.

Castañeda, P. (1992). New variational principles in plasticity and their application to composite materials. *Journal of Mechanics Physics of Solids*, 40:1757–1788.

Chen, T. and Yang, S.-H. (1995). The problem of thermal conduction for two ellipsoidal inhomogeneities in an anisotropic medium and its relevance to composite materials. *Acta Mechanica*, 111:41–58.

Cherkaev, A. (2000). *Variational methods for Structural Optimization*. Springer-Verlag.

Chow, T. and Ko, F. (1989). *Textile structural composites*. Elsevier, Amsterdam.

Chung, P. and Tamma, K. (1999). Woven fabric composites - developments in engineering bounds, homogenization and applications. *International Journal for Numerical Methods in Engineering*, 45(12):1757–1790.

Cluni, F. and Gusella, V. (2004). Homogenization of non-periodic masonry structures. *International Journal of Solids and Structures*, 41:1911–1923.

Cox, B. and Flanagan, G. (1997). Handbook of analytical methods for textile composites. NASA Contractor Report 4750, Langley Research Center. Available at `http://hdl.handle.net/2002/15043`.

Cox, B. and Yang, Q. (2006). In quest of virtual tests for structural composites. *Science*, 314(5802):1102–1107.

Černý, M., Glogar, P., and Machota, L. (2000). Resonant frequency study of tensile and shear elasticity moduli of carbon fibre reinforced composites (CFRC). *Carbon*, 38:2139–2149.

Diss, P., Lamon, J., Carpentier, L., Loubet, J., and Kapsa, P. (2002a). Sharp indentation behavior of carbon/carbon composites and varieties of carbon. *Carbon*, 40(14):2567–2579.

Diss, P., Lamon, J., Carpentier, L., Loubet, J., and Kapsa, P. (2002b). Sharp indentation behavior of carbon/carbon composites and varieties of carbon. *Carbon*, 40:2567–2579.

Djukic, L., Herszberg, G., Shoeppner, G., and Brownlow, L. (2008). Tow Visualization in Woven Composites using X-Ray Computed Tomography. In *TEXCOMP9, Recent Advances in Textile Composites*, pages 417–425. University of Delaware, Newark.

Dobiášová, L., Starý, V., Glogar, P., and Valvoda, V. (2002). X-ray structure analysis and elastic properties of a fabric reinforced carbon/carbon composite. *Carbon*, 40:1419–1426.

Dvorak, G. (2000). Composite materials: Inelastic behavior, damage, fatigue and fracture. *International Journal of Solids and Structures*, 37:155–170.

Eshelby, J. (1957). The determination of the elastic field of an ellipsoidal inclusion and related problems. *Proceeding of Royal Society, Series A*, 241:376–396.

Fischer-Cripps, A. (2004). *Nanoindentation*. Mechanical Engineering Series. Springer-Verlag, New York, second edition.

Frigo, M. and Johnson, S. (2005). The design and implementation of FFTW3. *Proceedings of the IEEE*, 93(2):216–231. special issue on "Program Generation, Optimization, and Platform Adaptation".

Gajdošík, J. (2005). Quantitative analysis of fiber composite. Master's thesis, CTU in Prague.

Gavazzi, A. and Lagoudas, D. (1990). On the numerical evaluation of eshelby's tensor and its application to elastoplastic fibrous composites. *Computational Mechanics*, 7(1):13–19.

Gommers, B., Verpoest, I., and Van Houtte, P. (1998). The Mori-Tanaka method applied to textile composite materials. *Acta Materialia*, 46(6):2223—-2235.

González, C. and Lorca, J. (2007). Virtual fracture testing of composites: A computational micromechanics approach. *Engineering Fracture Mechanics*, 74:1126–1138.

Gregory, J. and Spearing, S. (2005). Nanoindentation of neat and in situ polymers in polymer-matrix composites. *Composites Science and Technology*, 65(3–4):595–607.

Han, T.-S., Feenstra, P., and Billington, S. (2003). Simulation of highly ductile fiber-reinforced cement-based composite components under cyclic loading. *ACI Structural Journal*, 100(6):749–757.

Hatta, H. and Taya, M. (1986). Equivalent inclusion method for steady state heat conduction in composites. *International Journal of Engineering Science*, 24:1159–1170.

Hivet, G. and Boisse, P. (2005). Consistent 3D geometrical model of fabric elementary cell. Application to a meshing preprocessor for 3D finite element analysis. *Finite Elements in Analysis and Design*, 42(1):25–49.

Hrstka, O., Kučerová, A., Lepš, M., and Zeman, J. (2003). A competitive comparison of different types of evolutionary algorithms. *Computers & Structures*, 81(18–19):1979–1990.

Huysmans, G., Verpoest, I., and Van Houtte, P. (1998). A poly-inclusion approach for the elastic modelling of knitted fabric composites. *Acta Materialia*, 46(9):3003—-3013.

Jekabsons, N. and Byström, J. (2002). On the effect of stacked fabric layers on the stiffness of a woven composite. *Composites Part B: Engineering*, 33(8):619–629.

Jeong, H., Hsu, D., and Liaw, P. (1998). Anisotroic conductivities of multiphase particulate metal-matrix composites. *Composite Science and Technology*, 58:65–76.

Jirásek, M. and Zimmermann, Z. (1998). Analysis of rotating crack model. *Journal of Engineering Mechanics*, 124(8):842–851.

Kanari, M., Tanaka, K., Baba, S., and Eto, M. (1997). Nanoindentation behavior of a two-dimensional carbon-carbon composite for nuclear applications. *Carbon*, 35(10-11):1429–1437.

Knauss, W. (2000). Perspectives in Experimental Solid Mechanics. *International Journal of Solids and Structures*, 37:239–250.

Košek, M., Seják, P., and Vozková, P. (2008). Effect of Voids on Elastic Properties of Real C/C Composites. In *TEXCOMP9, Recent Advances in Textile Composites*, pages 193–201. University of Delaware, Newark.

Kubičár, L., Boháč, V., and Vretenár, V. (2002). Transient methods for the measurement of thermophysical properties: The pulse transient method. *High Temperatures - High Pressures*, 34:505–514.

Kuhn, J. and Charalambides, P. (1998). Elastic response of porous matrix plain weave fabric composites: Part I - Modeling, Part II - Results. *Journal of Composite Materials*, 32(16):1426–1471, 1472–1507.

Kuhn, J. and Charalambides, P. (1999). Modeling of plain weave fabric composite geometry. *Journal of Composite Materials*, 33(3):188–220.

Kumar, C., Matouš, K., and Geubelle, P. H. (2007). Reconstruction of periodic unit cells of multimodal random particulate composites using genetic algorithms. *Computational Materials Science*. Article in print, `http://dx.doi.org/`.

Kumar, H., Briant, C., and Curtin, W. (2006). Using microstructure reconstruction to model mechanical behavior in complex microstructures. *Mechanics of Materials*, 38(8–10):818–832. special issue on "Advances in Disordered Materials".

Li, V. and Wang, S. (2001). Tensile strain-hardening behavior of pva-ecc. *ACI Materials Journal*, 98(6):483–492.

Liao, J., Huang, B., Shi, G., Chen, T., and Xiong, X. (2002). Influence of porosity and total surface area on the oxidation resistance of C/C composites. *Carbon*, 40(13):2483–2488.

LIM (2008). *System Lucia G, User guide*. LUCIA – Laboratory Universal Computer Image Analysis. Home page: `http://www.laboratory-imaging.com`.

Lomov, S., Verpoest, I., Peeters, T., Roose, D., and Zako, M. (2003). Nesting in textile laminates: geometrical modelling of the laminate. *Composites Science and Technology*, 63(7):993–1007.

Lomov, S. V., Ivanov, D. S., Verpoest, I., Zako, M., Kurashiki, T., Nakai, H., and Hirosawa, S. (2007). Meso-FE modelling of textile composites: Road map, data flow and algorithms. *Composites Science and Technology*, 67(9):1870–1891.

Lu, B. and Torquato, S. (1992). Lineal-path function for random heterogeneous materials. *Physical Review E*, 45(2):922–929.

Mackerle, J. (2004). Finite element modelling and simulation of indentation testing: a bibliography (1990-2002). *Engineering Computations*, 21(1):23–52.

Malvern, L. (1969). *Introduction to the mechanics of a continuous medium*. Prentice-Hall, Inc., Englewood Cliffs, N.J.

Marx, D. and Riester, L. (1999). Mechanical properties of carbon–carbon composite components determined using nanoindentation. *Carbon*, 37(11):1679–1684.

Matouš, K., Inglis, H., Gua, X., Rypl, D., and Jackson, T. (2007). Multiscale modeling of solid propellants: From particle packing to failure. *Composites Science and Technology*, 67(7–8):1694–1708.

Matouš, K., Lepš, M., Zeman, J., and Šejnoha, M. (2000). Applying genetic algorithms to selected topics commonly encountered in engineering practice. *Computer Methods in Applied Mechanics and Engineering*, 190(13–14):1629–1650.

Mayerhöfer, T. (2005). Symmetric euler orientatio representation for orientational averaging. *Spectrochimica Acta*, Part A(61):2611–2621.

Mechtcherine, V. and Jůn, P. (2007). Stress-strain behaviour of strain-hardening cement-based composites (shcc) under repeated tensile loading. In *Fracture Mechanics of Concrete Structures*, pages 1441–1448.

Milton, G. (2002). *The Theory of Composites*, volume 6 of *Cambridge Monographs on Applied and Computational Mathematics*. Cambridge University Press.

Mori, T. and Tanaka, K. (1973). Average stress in matrix and average elastic energy of elastic materials with misfitting inclusions. *Acta Metallurgica*, 21:571–574.

Mura, T. (1987). *Micromechanics of Defects in Solids*. Number 3 in Mechanics of elastic and inelastic solids. Kluwer Academic Publishers, second revised edition.

Novák, J. and Kalousková, M. (2008). *Dokumentace programu SPERM 2.0*. CTU in Prague.

Novák, J., Zeman, J., and Šejnoha, M. (2004). Multiscale-based constitutive modeling of regular natural stone masonry. In *Proceedings of the Seventh International Conference on Computational Structures Technology*, pages 439–440.

Nowicki, M. and Susla, B. (2003). Nanoindentation as a tool for recognition of composites components. *Acta Physica Polonica A*, 104(3–4):365–372.

Ockham, W. (14th-century). Occam's razor. Available at `http://en.wikipedia.org/wiki/Occam's_Razor`.

Oezdemir, I., Brekelmans, W., and Geers, M. (2008). Computational homogenization for heat conduction in heterogeneous solids. *International journal for numerical methods in engineering*, 73(2):185–204.

Oh, I., Kim, J., Kim, J., Kim, K., and Joo, H. (1999). Effects of pressure on the pore formation of carbon/carbon composites during carbonization. *Journal of Materials Science*, 34(18):4585–4595.

Oliver, W. and Pharr, G. (1992). An improved technique for determining hardness and elastic modulus using load and displacement sensing indentation experiments'. *Journal of Material Research*, 7:1564–1583.

Ozcan, S. and Filip, P. (2005). Microstructure and wear mechanisms in C/C composites. *Wear*, 259(1–6):642–650.

Pahr, D. and Zysset, P. (2006). FEM surface and volume mesh extraction from CT bone data using a new segmentation method and deformable GVF models. *IEEE Transactions on Medical Imaging*. Submitted.

Palán, M. (2002). *Thermal properties of C-C composites reinforced by textile fabric*. PhD thesis, Technical University of Liberec.

Pastore, C. (1993). Quantification of processing artifacts in textile composites. *Composites Manufacturing*, 4(4):217–226.

Pešáková, V., Smetana, K., Balík, K., Hruška, J., Petrtýl, M., Hulejová, H., and Adam, M. (2003). Biological and biochemical properties of the carbon composite and polyethylene implant materials. *Journal of Material Science: Materials in Medicine*, 14:531–537.

Piat, R., Tsukrov, I., Mladenov, N., Guellali, M., Ermel, R., Beck, E., and Hoffman, M. (2007a). Material modeling of the CVI-infiltrated carbon felt II. Statistical study of the microstructure, numerical analysis and experimental validation. *Composite Science and Technology*, 66(15):2769–2775.

Piat, R., Tsukrov, I., Mladenov, N., Verijenko, M., Guellali, M., Schnack, E., and Hoffman, M. (2007b). Material modeling of the CVI-infiltrated carbon felt I. Basic formulae, theory and numerical experiments. *Composite Science and Technology*, 66(15):2997–3003.

Povirk, G. (1995). Incorporation of microstructural information into models of two-phase materials. *Acta Metallurgica et Materialia*, 43(8):3199–3206.

Rektorys, K., editor (1994). *Survey of applicable mathematics: Volume II*, volume 281 of *Mathematics and its Applications*. Kluwer Academic Publishers Group, Dordrecht, second revised edition.

Rots, J. (1998). *Computational modeling of concrete fracture*. PhD thesis, Delft University of Technology. Ph.D. thesis.

Simone, A., Sluys, L., and Kabele, P. (2003). Combined continuous/discontinuous failure of cementitious composites. In *Proceedings for EURO-C 2003: Computational Modelling of Concrete Structures*, pages 133–137.

Skoček, J., Zeman, J., and Šejnoha, M. (2006). On determination of periodic unit cell for plain weave fabric composites: Geometrical modeling of real world materials. *Engineering Mechanics*, 13(4):249–260. Available at `http://cml.fsv.cvut.cz/~zemanj/download/em_06_skocek.pdf`.

Skoček, J., Zeman, J., and Šejnoha, M. (2008). Effective properties of carbon-carbon textile composites: Application of the Mori-Tanaka method. *Modelling and Simulation in Materials Science and Engineering*, 16(8):15pp. Available at `http://arxiv.org/abs/0803.4166`.

Sol, H., Hua, H., DeVisscher, J., Vantomme, J., and DeWilde, W. (1997). A mixed numerical/experimental technique for the nondestructive identification of the stiffness properties of fibre reinforced composite materials. *NDT & E International*, 30(2):85–91.

Suryanto, B., Nagai, K., and Maekawa, K. (2008). Influence of damage on cracking behavior of ductile fibre-reinforced cementitious composite. In *Proceedings of 8th International Conference on Creep, Shrinkage and Durability of Concrete and Concrete Structures*, pages 495–500.

Sýkora, J., Vorel, J., Krejčí, T., Šejnoha, M., and Šejnoha, J. (2009). Analysis of coupled heat and moisture transfer in masonry structures. *Materials and Structures*, 42(8):1153–1167. Available at `http://arxiv.org/PS_cache/arxiv/pdf/0804/0804.3554v1.pdf`.

Šejnoha, J., Šejnoha, M., Zeman, J., Sýkora, J., and Vorel, J. (2008). Mesoscopic study on historic masonry. *Structural Engineering and Mechanics*, 30(1):99–117. Available at `http://arxiv.org/abs/0804.3262`.

Šejnoha, M., Valenta, R., and Zeman, J. (2004). Nonlinear viscoelastic analysis of statistically homogeneous random composites. *International Journal for Multiscale Computational Engineering*, 2(4):645–673.

Šejnoha, M. and Zeman, J. (2002). Overall viscoelastic response of random fibrous composites with statistically quasi uniform distribution of reinforcements. *Computer Methods in Applied Mechanics and Engineering*, 191(44):5027–5044.

Šejnoha, M. and Zeman, J. (2008). Micromechanical modeling of imperfect textile composites. *International Journal of Engineering Science*, 46:513–526.

Tomková, B. (2006). *Modeling of Thermophysical Properties of Woven Composites*. PhD thesis, TU Liberec.

Tomková, B. and Košková, B. (2004). The porosity of plain weave C/C composite as an input parameter for evaluation of material properties. In *International Conference Carbon 2004*, page 50. Providence, USA.

Tomková, B., Šejnoha, M., Novák, J., and Zeman, J. (2007). Evaluation of effective thermal conductivity of porous textile composites. *Composites Part B: Engineering*. submitted for publication.

Tomková, B., Šejnoha, M., Novák, J., and Zeman, J. (2008). Evaluation of effective thermal conductivities of porous textile composites. *International Journal for Multiscale Computational Engineering*, 6(2):153–168.

Torquato, S. (2002). *Random heterogeneous materials: Microstructure and macroscopic properties*. Interdisciplinary Applied Mathematics. Springer-Verlag New York.

Torquato, S. and Stell, G. (1982). Microstructure of two-phase random media.I. The n-point probability functions. *Journal of Chemical Physics*, 77(4):2071–2077.

Tsukrov, I., Piat, R., Novak, J., and Schnack, E. (2005). Micromechanical Modeling of Porous Carbon/Carbon Composites. *Mechanics of Advanced Materials and Structures*, 12:43–54.

Vopička, S. (2004). *Popis geometrie vyztužujícího systému v tkaninových kompozitech ("Description of geometry of textile composites reinforcing system")*. PhD thesis, Technical University of Liberec. In Czech.

Vorel, J., Sýkora, J., Šejnoha, J., and Šejnoha, M. (2006). Prediction of homogenized material properties of quarry masonry from micromechanics. In *Proceedings of The 5th International Congress of Croatian Society of Mechanics*.

Vorel, J. and Šejnoha, M. (2009). Evaluation of homogenized thermal conductivities of imperfect carbon-carbon textile composites using the mori-tanaka method. *Structural Engineering and Mechanics*, 0:0–0. Accepted.

Vozková, P. (2008). *Multiscale modeling of mechanical properties of textile composites*. PhD thesis, Texnical University in Liberec, Czech Republic. in Czech.

Wentorf, R., Collar, R., Shephard, M., and Fish, J. (1999). Automated modeling for complex woven mesostructures. *Computer Methods in Applied Mechanics and Engineering*, 172(1–4):273–291.

Whitcomb, J. and Tang, X. (2001). Effective moduli of woven composites. *Journal of Composite Materials*, 35(23):2127–2144.

Wierer, M. (2005). *Multi scale analysis of woven composites*. PhD thesis, Faculty of Civil Engineering, Czech Technical University in Prague.

Woo, K. and Whitcomb, J. (1997). Effects of fiber tow misalignment on the engineering properties of plain weave textile composites. *Composite Structures*, 37(3–4):281–417.

Yeong, C. and Torquato, S. (1998a). Reconstructing random media. *Physical Review E*, 57(1):495–506.

Yeong, C. and Torquato, S. (1998b). Reconstructing random media. II. Three-dimensional media from two-dimensional cuts. *Physical Review E*, 58(1):224–233.

Yurgartis, S., MacGibbon, B., and Mulvaney, P. (1992). Quantification of microcracking in brittle-matrix composites. *Journal of Materials Science*, 27(24):6679–6686.

Yurgartis, S., Morey, K., and Jortner, J. (1993). Measurement of yarn shape and nesting in plain-weave composites. *Composites Science and Technology*, 46(1):39–50.

Yushanov, S. and Bogdanovich, A. (1998). Stochastic theory of composite materials with random waviness of the reinforcements. *International Journal of Solids and Structures*, 35(22):2901–2930.

Zeman, J. (2003). *Analysis of composite materials with random microstructure*, volume 7 of *CTU Reports*. CTU in Prague. Available at `http://mech.fsv.cvut.cz/~zemanj/download/phd.pdf`.

Zeman, J. and Šejnoha, M. (2001). Numerical evaluation of effective properties of graphite fiber tow impregnated by polymer matrix. *Journal of the Mechanics and Physics of Solids*, 49(1):69–90.

Zeman, J. and Šejnoha, M. (2004a). Homogenization of balanced plain weave composites with imperfect microstructure: Part I - Theoretical formulation. *International Journal for Solids and Structures*, 41(22-23):6549–6571.

Zeman, J. and Šejnoha, M. (2004b). Homogenization of real-world balanced woven composites with imperfect microstructure. In *Proceedings of WCCM VI in conjunction with APCOM 04*, pages 1–10. Thinghua University Press & Springer Verlag.

Zeman, J. and Šejnoha, M. (2007). From random microstructures to representative volume elements. *Modelling and Simulation in Materials Science and Engineering*, 15:325–335.

LIST OF AUTHOR'S PUBLICATIONS

Year 2009

Sýkora, J., Vorel, J., Krejčí, T., Šejnoha, M., and Šejnoha, J. (2009). Analysis of coupled heat and moisture transfer in masonry structures. *Materials and Structures*, 42(8):1153–1167. Available at `http://arxiv.org/PS_cache/arxiv/pdf/0804/0804.3554v1.pdf`.

Vorel, J. and Boshoff, W. (2009). Numerical modelling of strain hardening fibre-reinforced composites. In *Proceedings of Advanced Concrete Materials 2009*, pages 1–8.

Vorel, J. and Šejnoha, M. (2009a). Effective thermal conductivities of multilayer plain weave textile composites. In *Proceedings of 2nd South-East European Conference on Computational Mechanics*, pages 1–6.

Vorel, J. and Šejnoha, M. (2009b). Effective thermal conductivity of porous c/c textile composites. In *Proceedings of 6th International Congress of Croatian Society of Mechanics*, pages 1–7.

Vorel, J. and Šejnoha, M. (2009c). Evaluation of homogenized thermal conductivities of imperfect carbon-carbon textile composites using the mori-tanaka method. *Structural Engineering and Mechanics*, 0:0–0. Accepted.

Year 2008

Janda, T., Vorel, J., and Šejnoha, M. (2008). *Documentation for ParamSeeker program*. Available at `http://www.inzenyr.com/download.html`.

Sýkora, J. and Vorel, J. (2008a). Analysis of coupled heat and moisture transfer in masonry structures. In *Engineering Mechanics 2008*. Institute of Thermomechanics AS CR.

Sýkora, J. and Vorel, J. (2008b). Analýza sdruženého přenosu tepla a vlhkosti ve zděných konstrukcích. In *Proceedings of Juniorstav 2008*. VUT FAST. In Czech.

Sýkora, J., Vorel, J., and Šejnoha, M. (2008). Evaluation of effective conductivities for masonry with interfaces. *Bulletin of Applied Mechanics*, 4(13):18–23.

Sýkora, J., Vorel, J., and Šejnoha, M. (2008a). Evaluation of effective conductivities for masonry with interfaces. In *Proceedings of MK2*, pages 99–100. CTU.

Sýkora, J., Vorel, J., and Šejnoha, M. (2008b). Evaluation of effective conductivities for masonry with interfaces. In *Proceedings of 4th International Conference on Advances in Structural Engineering and Mechanics*, pages 1–12. Techno-Press.

Šejnoha, J., Šejnoha, M., Zeman, J., Sýkora, J., and Vorel, J. (2008). Mesoscopic study on historic masonry. *Structural Engineering and Mechanics*, 30(1):99–117. Available at `http://arxiv.org/abs/0804.3262`.

Vorel, J. and Sýkora, J. (2008). Efektivní tepelná vodivost textilních kompozitů uhlík/uhlík: Využití metody Mori-Tanaka. In *Proceedings of Juniorstav 2008*. VUT FAST. In Czech.

Vorel, J., Sýkora, J., and Šejnoha, M. (2008a). Two step homogenization of effective thermal conductivity for macroscopically orthotropic C/C composites. *Bulletin of Applied Mechanics*, 4(14):48–53.

Vorel, J., Sýkora, J., and Šejnoha, M. (2008b). Determination of homogenized thermal conductivity using Mori-Tanaka method. In *Proceedings of 4th International Conference on Advances in Structural Engineering and Mechanics*, pages 1–11. Techno-Press.

Vorel, J., Sýkora, J., and Šejnoha, M. (2008c). Effective thermal conductivity of carbon-carbon plain weave textile composites. In *Engineering Mechanics 2008*, pages 1171–1176. Institute of Thermomechanics AS CR.

Vorel, J., Sýkora, J., and Šejnoha, M. (2008d). Two step homogenization of effective thermal conductivity for macroscopically orthotropic C/C composites. In *Proceedings of MK2*, pages 103–104. CTU.

Vorel, J. and Šejnoha, M. (2008). *Documentation for HELP program*. Available at `http://www.inzenyr.com/download.html`.

Vorel, J., Šejnoha, M., and Zeman, J. (2008e). Effective thermal conductivity of imperfect carbon-carbon textile composites using the Mori-Tanaka method. In *Proceedings of 8th World Congress on Computational Mechanics*. International Center for Numerical Methods in Engineering.

Year 2007

Sýkora, J. and Vorel, J. (2007). A three-invariant smooth cap model. In *Proceedings of Juniorstav 2007*. VUT FAST. In Czech.

Sýkora, J., Vorel, J., and Novák, J. (2007a). Experimentální a numerická identifikace materiálových parametrů zdiva. In *Engineering Mechanics 2007*. Institute of Thermomechanics AS CR. In Czech.

Sýkora, J., Vorel, J., and Šejnoha, M. (2007b). Design of damage-plastic model for quasi-brittle materials. In *Computational Plasticity IX*, pages 628–630. University of Catalunya.

Vorel, J. and Sýkora, J. (2007a). Experimentální a numerická identifikace materiálových parametrů zdiva. In *Proceedings of Juniorstav 2007*. VUT FAST. In Czech.

Vorel, J. and Sýkora, J. (2007b). A numerical model for quasi-brittle materials. In *Engineering Mechanics 2007*. Institute of Thermomechanics AS CR.

Vorel, J., Sýkora, J., and Šejnoha, M. (2007a). Determination of size independent fracture energy for regular masonry. In *Computational Plasticity IX*, pages 628–630. University of Catalunya.

Vorel, J., Sýkora, J., and Šejnoha, M. (2007b). An improved constitutive model for nonlinear homogenization of masonry structures. In *Proceedings of the 18th Engineering Mechanics Division Conference of the American Society of Civil Engineers*. Virginia Tech.

Year 2006

Sýkora, J. and Vorel, J. (2006). Numerical modelling of quarry-masonry. In *Book of Abstracts of 3rd PhD Workshop Brno - Prague - Weimar*, pages 27–28. Institut für Strukturmechanik.

Sýkora, J., Vorel, J., and Šejnoha, M. (2006a). Numerical modeling of quarry-masonry with application to the charles bridge. In *Engineering Mechanics 2006*. Institute of Theoretical and Applied Mechanics AS CR.

Sýkora, J., Vorel, J., Šejnoha, M., Zeman, J., and Šejnoha, J. (2006b). Multi-scale modeling of masonry structures - synthesis of constitutive models and scale transition. In *Proceedings of the 5th International Congress of Croatian Society of Mechanics*. Croatian Society of Mechanics.

Šejnoha, J., Šejnoha, M., Sýkora, J., and Vorel, J. (2006a). An improved material model for quarry masonry. In *Proceedings of the 5th International Congress of Croatian Society of Mechanics*. Croatian Society of Mechanics.

Šejnoha, M., Šejnoha, J., Novotná, E., Vorel, J., and Sýkora, J. (2006b). Prediction of the effective fracture energy in quarry masonry. In *Proceedings of the Eighth International Conference on Computational Structures Technology*. Civil-Comp Press Ltd.

Vorel, J. (2006). Efektivní termomechanické vlastnosti zdiva. Master's thesis, CTU in Prague. In Czech.

Vorel, J. and Sýkora, J. (2006). Effective mechanical properties of masonry. In *Book of Abstracts of 3rd PhD Workshop Brno - Prague - Weimar*, pages 39–40. Institut für Strukturmechanik.

Vorel, J., Sýkora, J., Šejnoha, J., and Šejnoha, M. (2006a). Prediction of homogenized material properties of quarry masonry from micromechanics. In *Proceedings of The 5th International Congress of Croatian Society of Mechanics*. Croatian Society of Mechanics.

Vorel, J., Sýkora, J., and Šejnoha, M. (2006b). Determination of effective thermomechanical

properties of masonry based on numerical homogenization. In *Engineering Mechanics 2006*. Institute of Theoretical and Applied Mechanics AS CR.

Year 2005

Sýkora, J., Vorel, J., Šejnoha, J., and Šejnoha, M. (2005). Effective material parameters for transport processes in historical masonry structures. In *Proceedings of the Tenth International Conference on Civil, Structural and Environmental Engineering Computing*, pages 459–460. Civil-Comp Press Ltd.

Vorel, J., Sýkora, J., Šejnoha, J., and Šejnoha, M. (2005). Materiálový model pro lomové zdivo. In *Integrovaný přístup k projektování stavebních konstrukcí*, pages 1–6. Vysoká škola báňská. In Czech.

Appendix A

ESHELBY'S TENSOR FOR AN ELLIPSOIDAL INCLUSION

The Eshelby tensor for thermal conductivity problem was introduced by Hatta and Taya (1986). For an ellipsoidal inclusion with semi-axis ξ_1, ξ_2, ξ_3 in an isotropic matrix it receives the form

$$\begin{aligned} \mathbf{S} &= \frac{\xi_1\xi_2\xi_3}{4}\frac{\partial}{\partial \boldsymbol{x}^2}\int_0^\infty \left(\frac{x_1^2}{\xi_1^2+s}+\frac{x_2^2}{\xi_2^2+s}+\frac{x_3^2}{\xi_3^2+s}\right)\frac{1}{\Delta s}\mathrm{d}s, \\ \Delta s &= \sqrt{\left(\xi_1^2+s\right)\left(\xi_2^2+s\right)\left(\xi_3^2+s\right)}. \end{aligned} \tag{A.1}$$

The evaluation of this integral can be found for special ellipsoidal cases in (Hatta and Taya, 1986). For the general ellipsoid the solution was introduced by Jeong et al. (1998) and as well by Chen and Yang (1995).

Sometimes the evaluation of $\mathbf{S}$ tensor calls for the solution of the problem of an ellipsoidal inclusion in an orthotropic matrix. To summarize the notation of the thermal conductivity tensor the anisotropic medium is represented by

$$\boldsymbol{\chi} = \begin{bmatrix} \chi_{11} & \chi_{12} & \chi_{13} \\ \chi_{21} & \chi_{22} & \chi_{23} \\ \chi_{31} & \chi_{32} & \chi_{33} \end{bmatrix}, \tag{A.2}$$

or when referring to its principal axes

$$\boldsymbol{\chi} = \begin{bmatrix} \chi_1 & 0 & 0 \\ 0 & \chi_2 & 0 \\ 0 & 0 & \chi_3 \end{bmatrix}. \tag{A.3}$$

To proceed we start from a general orthotropic form of the Laplace equation

$$\chi_1\frac{\partial^2 T}{\partial x_1^2}+\chi_2\frac{\partial^2 T}{\partial x_2^2}+\chi_3\frac{\partial^2 T}{\partial x_3^2}=0. \tag{A.4}$$

Introducing the following substitutions

$$x_1=\sqrt{\chi_1}\tilde{x}_1; \quad x_2=\sqrt{\chi_2}\tilde{x}_2; \quad x_3=\sqrt{\chi_3}\tilde{x}_3, \tag{A.5}$$

allows us to convert Eq. (A.4) into

$$\frac{\partial^2 T}{\partial \tilde{x}_1^2} + \frac{\partial^2 T}{\partial \tilde{x}_2^2} + \frac{\partial^2 T}{\partial \tilde{x}_3^2} = 0, \tag{A.6}$$

which essentially reassembles the form of Laplace equation for an isotropic medium. With similar mathematical substitution we can transform Eq. (A.1) into

$$S_{ii} = \frac{\xi_1 \xi_2 \xi_3}{2\sqrt{\chi_1 \chi_2 \chi_3}} \int_0^\infty \frac{1}{\left(\xi_i^2/\chi_i + s\right) \Delta s} \mathrm{d}s, \tag{A.7}$$

where

$$\Delta s = \sqrt{\left(\xi_1^2/\chi_1 + s\right)\left(\xi_2^2/\chi_2 + s\right)\left(\xi_3^2/\chi_3 + s\right)}. \tag{A.8}$$

A simple example of an isotropic void (ellipsoidal inclusion with $\boldsymbol{\xi} = (1, 1.5, 2)$, $\chi^v = 0.2$) surrounded by an orthotropic matrix ($\chi_{11}^m = 20, \chi_{22}^m = 1, \chi_{33}^m = 2$) was considered to acknowledge correctness of Eq. (A.7). Fig. A.1 shows the comparison of the MT predictions with the finite element results found for a hexagonal arrangement of voids under periodic boundary conditions (Tomková et al., 2008).

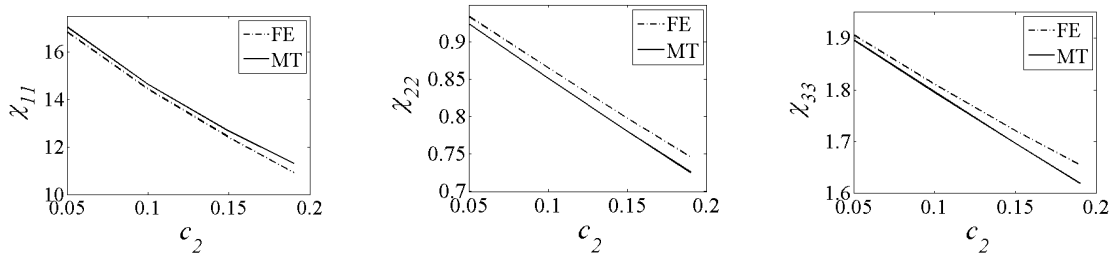

(a) (b) (c)

Figure A.1: Case study: Effective conductivities in [$\mathrm{Wm^{-1}K^{-1}}$] as a function of the volume fraction of the porous phase

Appendix B

$\mathbf{HE_LP}$ PROGRAM

B.1 Basic specifications and method

Program $\mathbf{HE_LP}$ (**H**eat and **El**asticity **P**roperties) is a simple software for the determination of effective elastic properties and effective thermal conductivities using the Mori-Tanaka homogenization method. This program can be used for ellipsoidal inhomogeneities embedded in a generally anisotropic medium. $\mathbf{HE_LP}$ was originally designed for evaluation of effective material properties of carbon-carbon plain weave textile composites on the micro- and meso-scale, see Chapter 4 and Section 5.1. Therefore, the homogenization with the orientational averaging is also implemented.

B.2 User guide

Program $\mathbf{HE_LP}$ [1] offers a user friendly environment. It allows us to address three major topics:

- Evaluation of the effective elastic properties of multi-phase composites with aligned inclusions of the ellipsoidal shape
- Evaluation of the effective thermal conductivities of multi-phase composites with aligned inclusions of the ellipsoidal shape
- Evaluation of the effective elastic properties and effective thermal conductivities of textile composites

All sheets are designed in a similar way. The program window has common tool bar buttons on the top of the window and is divided into four parts, (Fig. B.1)

[1] `www.inzenyr.com/download.html`

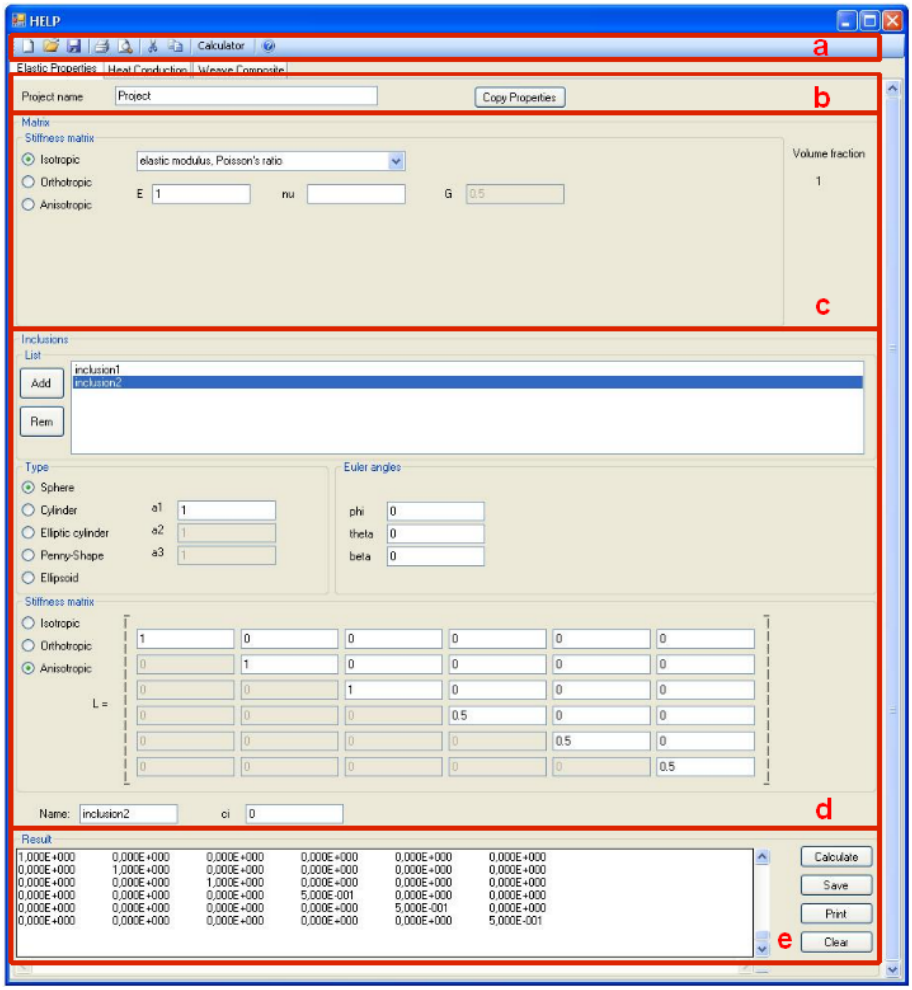

Figure B.1: HE$_L$P window structure: (a) Common tool strip buttons, (b) general informations, (c) matrix properties, (d) inclusions (tows) properties, (e) result viewer

B.2.1 Effective elastic properties and thermal conductivities

These program sheets serve to determine the effective (homogenized) stiffness and conductivity matrices, respectively. As shown in Fig. B.1, the top part of the main window (group box *"Matrix"*) is reserved for the material parameters of the matrix phase whereas the material parameters of the inclusion (group box *"Incusion"*) are assigned in the middle part of the main window. The results (group box *"Results"*) are displayed at the bottom of the main window.

The number of required parameters to input depends on the degree of material anisotropy of a given phase. The inclusion section is designed as to add or remove an arbitrary number

of inclusions. Apart from the material parameters this section requires specifying shape of the inclusion, Euler angles and volume fraction, see Fig. B.2 for the example of evaluation of effective thermal conductivities.

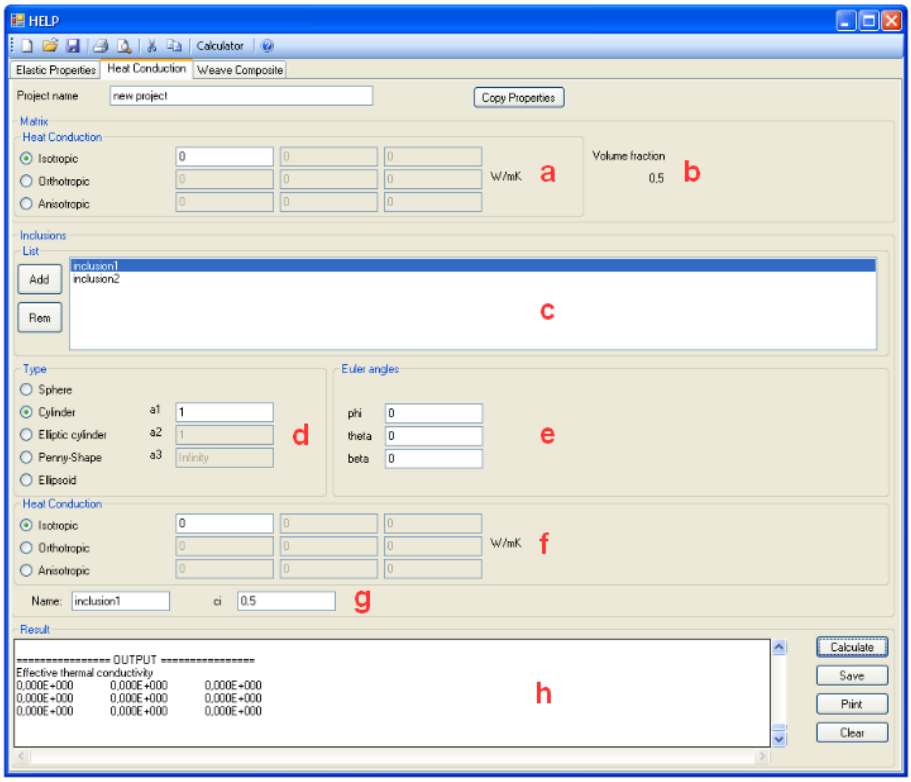

Figure B.2: Heat conduction: (a) Thermal conduction matrix, (b) matrix volume fraction, (c) inclusion list, (d) semi-axes, (e) Euler angles, (f) material properties for an inclusion, (g) name and volume fraction, (h) output window

B.2.2 Weave composite

There are only minor changes in the input when compared to more simple composite aggregates discussed in the previous section. First, the problem (elasticity or thermal conduction) must be selected (Fig. B.3a). Then the dimensions of the periodic unit cell (PUC) are required (Fig. B.3b). The quantities signs are the same as in Fig. 4.4a. The matrix material properties are assigned in the same way as above. The *"Tow"* box serves to specify the effective properties of perpendicular bundles. The common volume fraction for the weft and warp system of tows is assumed, see Fig. B.3d. The shape of the bundle is defined through its semi-axes

(Fig. B.3e) and orientation with respect to the global coordinate system using again the Euler angles (Fig. B.3f). The required material parameters are introduced next (again depending on the selected type of the material symmetry) in the bundle local coordinate system. Note that the local x_1 axis is aligned with the fiber direction. As discussed in Section 5.1, it is also required to choose the type of analysis (Fig. B.3h).

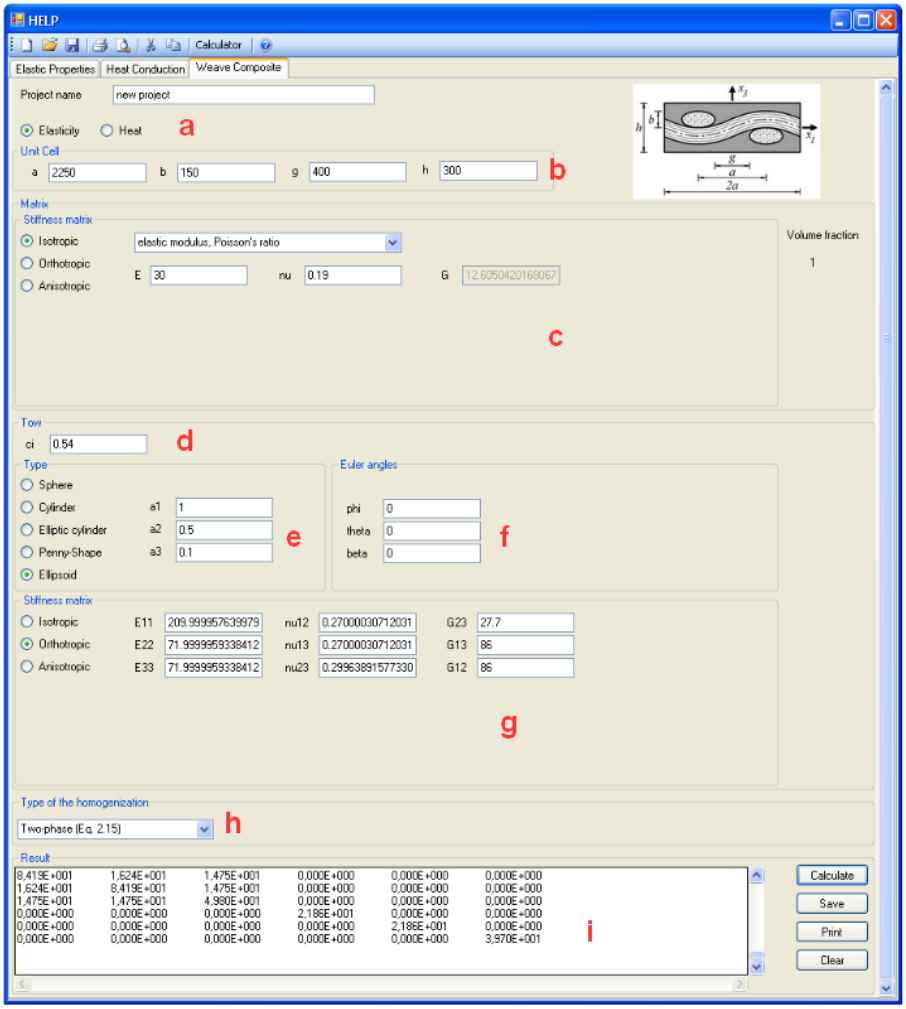

Figure B.3: Weave composite: (a) Problem type, (b) PUC dimensions, (c) matrix properties, (d) tows volume fraction, (e) semi-axes, (f) Euler angles, (g) material properties for bundles, (h) homogenization type, (i) output window

B.2.3 Input/Output file

The input/output project files includingthe matrix and inclusions (tows) parameters are stored in the *"XML"* format and are assigned the file name extension *".XMLH"*. Note that only the active sheets are saved when pressing the save bottom on the top tool bar of the main window. The same applies when loading the project. The structure of these files can be seen by generating an output file from the $\mathbf{HE_LP}$ program.

There are two possibilities to save the results displayed in the output window when pressing the save bottom on the right bottom part of the main window. The first possibility is to save the whole text in the specified text file. The other option is based on standard copy and paste operations.

Appendix C

NUMERICAL MODELING OF STRAIN HARDENING FIBER-REINFORCED COMPOSITES

C.1 Introduction

Strain Hardening Cement-based Composite (SHCC) is a type of High Performance Concrete (HPC) that was developed to overcome the brittleness of conventional concrete. Even though there is no significant compressive strength increase compared to conventional concrete, it exhibits superior behavior in tension. It has been shown to reach a tensile strain capacity of more than 4% during a pseudo strain hardening phase (Li and Wang, 2001; Boshoff and van Zijl, 2007). This pseudo strain hardening is achieved by the formation of fine, closely spaced multiple cracks with crack widths normally not exceeding $100\mu m$ (Li and Wang, 2001). These fine cracks, compared to large (larger than $100\mu m$) localized cracks found in conventional concrete, have the advantage of increased durability. For a further discussion of the mechanical properties of SHCC, the reader is referred to (Boshoff et al., 2009a,b).

Several scholars have simulated SHCC mechanical behavior with the Finite Element Method (FEM). Kabele (2000) formulated a model to simulate the mechanical behavior of SHCC using a smeared cracking approach. Despite acknowledging that a discrete cracking model would be best for the final localizing crack, Kabele decided to use a smeared cracking approach for the localization. This is due to the uncertainty of the position of the final localizing crack. Another model was proposed by Han et al. (2003). This model was created to simulate the behavior of SHCC under cyclic loading to test the improvement of structural response if SHCC elements are used to dissipate energy during earth-quake loadings. Computational modeling of SHCC was also performed by Simone et al. (2003) who used an embedded discontinuity approach for the final material softening. This method would have the same kinematic characterization as one obtained with interface elements for discrete cracking, but does not require remeshing procedures. Their conclusion was that it did not

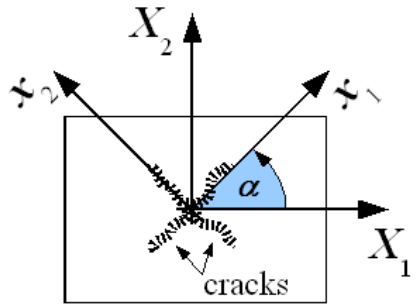

Figure C.1: Coordinates and transformation angle

simulate the experimental results of SHCC satisfactorily due to the simplicity of the model.

Boshoff (2007) created a simple damage mechanics based model for the tensile behavior of SHCC. This was implemented numerically using the FEM. Even though numerous shortcomings still exist, the model showed relatively good results. Remaining issues include an unresolved mesh dependence and the under prediction of the deformation when analyzing a structure with a strain gradient.

The primary objective of the presented research is to develop a constitutive model that can be used to simulate structural components with SHCC under different types of loading conditions. In particular, the constitutive model must be efficient and robust for large-scale simulations while restricted number of material parameters is needed. The proposed model for plane stress is outlined and the results of the preliminary implementation are shown.

C.2 Model definition

For the modeling of specific behavior of SHCC in tension, the application of classical constitutive material models used for quasi-brittle materials is not straightforward. The proposed numerical model is based on a rotating crack assumption to capture specific characteristics of SHCC, i.e. the strain hardening and softening, the multiple cracking and the crack localization. Multiple orthogonal crack patterns are allowed which is in accordance with the observations presented by Suryanto et al. (2008). A schematic representation of orthogonal cracking using the rotating crack model is shown using global and local axes in Fig. C.1. A complete description of the rotating crack model can be found in (Rots, 1998).

The presented model is implemented in a commercially available software package, **DIANA** (BV., 2008), for a plane stress elements using a coaxial rotating crack model (RCM) with two orthogonal cracks as described in (Han et al., 2003). This numerical approach is classified as the smeared cracking approach. When implementing the model into a non-linear fine element code, the incremental-iterative procedure based on a strain increment is assumed. Therefore, the strain vector $\boldsymbol{\varepsilon} = \{\varepsilon_{11}, \varepsilon_{22}, \gamma_{12}\}^{\mathsf{T}}$ reads

$$\boldsymbol{\varepsilon}^{(i)} = \boldsymbol{\varepsilon}^{(i-1)} + \Delta\boldsymbol{\varepsilon}, \tag{C.1}$$

where i stands for an increment number and $\Delta\boldsymbol{\varepsilon}$ is a strain increment vector. The rotating crack model evaluates a given strain state and generates the inelastic strain in the principal directions of the strain. Therefore, it is inevitably required to introduce a transformation tensor $([\mathsf{T}]_{\varepsilon}, [\mathsf{T}]_{\sigma})$ interconnecting global and a principal strain $\mathbf{e} = \{e_1, e_2, 0\}^{\mathsf{T}}$ or stress $\mathbf{s} = \{s_1, s_2, 0\}^{\mathsf{T}}$, respectively

$$\mathbf{e} = [\mathsf{T}]_{\varepsilon}\,\boldsymbol{\varepsilon}, \quad \mathbf{s} = [\mathsf{T}]_{\sigma}\,\boldsymbol{\sigma}. \tag{C.2}$$

Using the standard transformation rule the tensors are

$$[\mathsf{T}]_{\varepsilon} = \begin{bmatrix} n_{11}^2 & n_{12}^2 & n_{11}n_{12} \\ n_{21}^2 & n_{22}^2 & n_{21}n_{22} \\ 2n_{11}n_{21} & 2n_{12}n_{22} & n_{11}n_{22} + n_{12}n_{21} \end{bmatrix}, \tag{C.3}$$

$$\boldsymbol{n} = \begin{bmatrix} \cos\alpha & \sin\alpha \\ -\sin\alpha & \cos\alpha \end{bmatrix}, \tag{C.4}$$

with the relations between $[\mathsf{T}_{\varepsilon}]$ and $[\mathsf{T}_{\sigma}]$

$$[\mathsf{T}]_{\sigma}{}^{\mathsf{T}} = [\mathsf{T}]_{\varepsilon}{}^{-1} \quad \text{and} \quad [\mathsf{T}]_{\varepsilon}{}^{\mathsf{T}} = [\mathsf{T}]_{\sigma}{}^{-1}. \tag{C.5}$$

The rotation angle α can be obtained by means of a standard relation

$$\alpha = 1/2 \arctan\left[\gamma_{12}/\left(\varepsilon_{11} - \varepsilon_{22}\right)\right]. \tag{C.6}$$

The incremental stress-strain law (in the crack orientation) reads

$$\Delta\mathbf{s} = [\tilde{\mathsf{D}}]\Delta\mathbf{e}, \tag{C.7}$$

$$[\tilde{\mathsf{D}}] = \begin{bmatrix} \frac{\mathrm{d}s_1}{\mathrm{d}e_1} & \frac{\mathrm{d}s_1}{\mathrm{d}e_2} & 0 \\ \frac{\mathrm{d}s_2}{\mathrm{d}e_1} & \frac{\mathrm{d}s_2}{\mathrm{d}e_2} & 0 \\ 0 & 0 & \frac{s_1 - s_2}{2(e_1 - e_2)} \end{bmatrix}, \tag{C.8}$$

where $[\tilde{\mathsf{D}}]$ is the tangent material stiffness matrix. The derivation can be found in (Jirásek and Zimmermann, 1998). The stiffness matrix is transformed to the global coordinates using the standard transformation rule

$$[\mathsf{D}] = [\mathsf{T}_\varepsilon]^{\mathsf{T}} [\tilde{\mathsf{D}}] [\mathsf{T}_\varepsilon] \tag{C.9}$$

C.2.1 Poisson's ratio effect and equivalent principal stresses

It has to be mentioned that the rotating crack approach does not automatically include the effect of Poisson's ratio as the stress is evaluated on the basis of individual principal strains. In (Han et al., 2003) the definition of equivalent strain is used to take this effect into account. This approach is reliable when a model formulation does not permit residual deformations by cyclic loading, i.e. by changing state (tension to compression and vice versa). However, in the model presented in this study permanent (residual) deformations are allowed. Therefore, a new approach was employed to treat the effect of Poisson's ratio. The effective principal strain $(\hat{\mathbf{e}})$ is used to determine the equivalent stress $(\hat{\mathbf{s}})$ from the simplified uniaxial stress-strain diagram (see Secs. C.2.2.1, C.2.2.2). The effective principal strain is based on the principal strain $(\mathbf{e})$ which is free of inelastic deformations caused during the stress state change. The final stresses are consequently evaluated as

$$\begin{Bmatrix} s_1 \\ s_2 \end{Bmatrix} = \frac{1}{1-\nu_{12}\nu_{21}} \begin{bmatrix} 1 & \nu_{12} \\ \nu_{21} & 1 \end{bmatrix} \begin{Bmatrix} \hat{s}_1 \\ \hat{s}_2 \end{Bmatrix}, \tag{C.10}$$

$$\nu_{12} = \nu_0 E_1/E_0, \quad \nu_{21} = \nu_0 E_2/E_0, \tag{C.11}$$

where E_0 and ν_0 stand for Young's modulus and Poisson's ratio of the undamaged material respectively. The parameters E_1, E_2, ν_{12} and ν_{21} represent the characteristics of the damaged material in a given direction and are defined in Sec. C.2.2. The isotropic elastic material is represented in the state without cracks $(E_1 = E_2 = E_0,\ \nu_{12} = \nu_{21} = \nu_0)$ and the orthotropic when the crushing or cracking starts.

$$\{\hat{s}_1, \hat{s}_2\}^{\mathsf{T}} = \left\{E_1 e_1^{\mathsf{el}}, E_2 e_2^{\mathsf{el}}\right\}^{\mathsf{T}}. \tag{C.12}$$

Stiffness matrix introduced with this approach satisfies the condition of symmetry for orthotropic materials. Combining Eqs. (C.10,C.12) further gives

$$\begin{Bmatrix} s_1 \\ s_2 \end{Bmatrix} = \frac{1}{1-\nu_{12}\nu_{21}} \begin{bmatrix} E_1 & \nu_{12}E_2 \\ \nu_{21}E_1 & E_2 \end{bmatrix} \begin{Bmatrix} e_1^{\mathsf{el}} \\ e_2^{\mathsf{el}} \end{Bmatrix}, \tag{C.13}$$

where $\nu_{12}E_2 = \nu_{21}E_1$ and superscript $\cdot^{\text{el}}$ represents the elastic part.

C.2.2 Equivalent stress

The equivalent stress state in principal direction is determined by the stress function $\hat{s}_{t(c)}$ as a function of the current principal strain and associated history parameters.

The stress function is based on the uniaxial strain-stress diagrams in compression and tension. The experimental data are idealized to obtain a suitable mathematical representation of this constitutive model.

C.2.2.1 Tension

The material response for virgin loading in tension (Fig. C.2(a)) is described for each individual part by

$$\hat{s}_t\left(\hat{e} \geq \varepsilon_{tmax}\right) = \begin{cases} E_0\hat{e} & 0 \leq \hat{e} \leq \varepsilon_{t0} \\ \sigma_{t0} + (\sigma_{tp} - \sigma_{t0})\left[-2\left(\frac{\hat{e}-\varepsilon_{t0}}{\varepsilon_{tp}-\varepsilon_{t0}}\right)^3 + 3\left(\frac{\hat{e}-\varepsilon_{t0}}{\varepsilon_{tp}-\varepsilon_{t0}}\right)^2\right] & \varepsilon_{t0} < \hat{e} \leq \varepsilon_{tp} \\ \sigma_{tp}\left[2\left(\frac{\hat{e}-\varepsilon_{tp}}{\varepsilon_{tu}-\varepsilon_{tp}}\right)^3 - 3\left(\frac{\hat{e}-\varepsilon_{tp}}{\varepsilon_{tu}-\varepsilon_{tp}}\right)^2 + 1\right] & \varepsilon_{tp} < \hat{e} < \varepsilon_{tu} \\ 0 & \varepsilon_{tu} \leq \hat{e}. \end{cases} \tag{C.14}$$

The model parameters are depicted in Fig. C.2(a). The elastic part is assumed to be linear whereas the hardening and the softening sections are defined by means of Hermit functions.

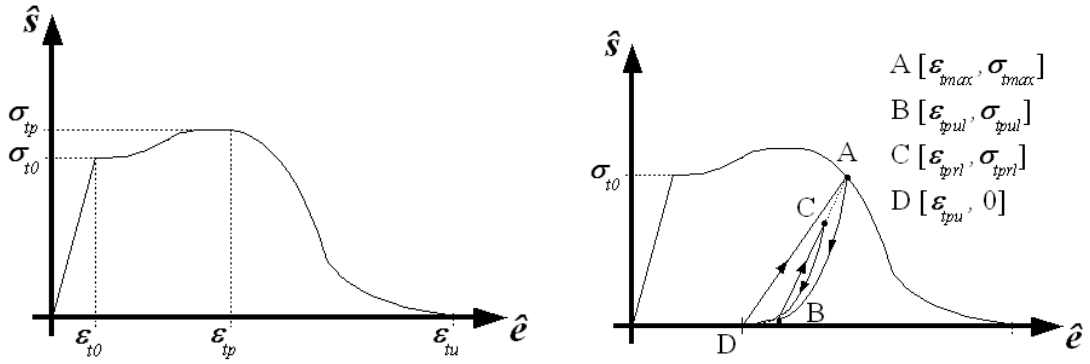

(a) (b)

Figure C.2: Tensile response: (a) Virgin loading, (b) loading/unloading

The unloading and reloading scheme shown in Fig. C.2(b) is based on the experiments presented by Mechtcherine and Jůn (2007).

$$\hat{s}_t\left(\hat{e}<\varepsilon_{tmax}\right)=\begin{cases} E_0\hat{e} & 0\leq\varepsilon_{tmax}\leq\varepsilon_{t0} \\ \sigma^*_{tmax}\left(\frac{\hat{e}-\varepsilon_{tul}}{\varepsilon^*_{tmax}-\varepsilon_{tul}}\right)^{a_t} & \varepsilon_{t0}<\varepsilon_{tmax}<\varepsilon_{tu},\dot{e}<0 \\ \sigma^*_{tul}+\left(\sigma_{tmax}-\sigma^*_{tul}\right)\frac{\hat{e}-\varepsilon^*_{tul}}{\varepsilon_{tmax}-\varepsilon^*_{tul}} & \varepsilon_{t0}<\varepsilon_{tmax}<\varepsilon_{tu},\dot{e}\geq 0 \\ 0 & \varepsilon_{tu}\leq\varepsilon_{tmax}. \end{cases} \tag{C.15}$$

The unloading curve is based on the polynomial function and the reloading is assumed to be linear. The partial unloading and reloading is incorporated using

$$\begin{aligned} \varepsilon^*_{tmax} &= \min\left(\varepsilon_{tmax},\varepsilon_{tprl}\right), \\ \varepsilon^*_{tul} &= \max\left(\varepsilon_{tul},\varepsilon_{tpul}\right), \end{aligned} \tag{C.16}$$

where $\sigma^*_{tmax},\sigma^*_{tul}$ are associated stresses and ε_{tmax} is the maximum strain experienced in previous steps with stress σ_{tmax}. The evolution of inelastic strain ε_{tul} is assumed to be linearly dependent on ε_{tmax} for the elastic and hardening part and linearly dependent on the crack opening for the softening branch (Eq. (C.17)). This simplification correlates well with recent, unpublished cyclic tensile results done at Stellenbosch University, see Fig. C.3(a).

$$\varepsilon_{tul}=\begin{cases} 0 & 0\leq\varepsilon_{tmax}\leq\varepsilon_{t0} \\ b_t\left(\varepsilon_{tmax}-\varepsilon_{t0}\right) & \varepsilon_{t0}<\varepsilon_{tmax}\leq\varepsilon_{tp} \\ \min\left\{b_t\left(\varepsilon_{tp}-\varepsilon_{t0}\right)+b_t\left[\varepsilon_{tmax}-b_t\left(\varepsilon_{tp}-\varepsilon_{t0}\right)-\sigma_{tmax}/E_{tp}\right],\right. & \\ \left. b_t\left(\varepsilon_{tp}-\varepsilon_{t0}+w_t/h\right)\right\} & \varepsilon_{tp}<\varepsilon_{tmax}, \end{cases} \tag{C.17}$$

where $E_{tp}=\sigma_{tp}/\left[\varepsilon_{tp}-b_t(\varepsilon_{tp}-\varepsilon_{t0})\right]$. The parameter a_t governs the unloading trajectory and must be determined from the experimental tests as well as the material characteristic b_t.

To ensure proper energy dissipation during localizing, the crack band approach is used which relates the strain ε_{tu} to the crack opening for the complete force transfer loss (w_t) and element size (h), see Eq. (C.18). The crack opening can be considered as a half of the fiber length (Boshoff, 2007). In the present study the equivalent crack band width is evaluated by projecting the element into the direction normal to the crack at its initiation (h). This is done for each cracking direction separately. The last term in Eq. (C.18) describes the influence of the unloading where more energy is dissipated when the non-linear law is

employed (Fig. C.3(b)).

$$\varepsilon_{tu} = \varepsilon_{tp} + \frac{w_t}{h} - 2\frac{\varepsilon_{tp} - b_t\left(\varepsilon_{tp} - \varepsilon_{t0}\right)}{a_t + 1}. \tag{C.18}$$

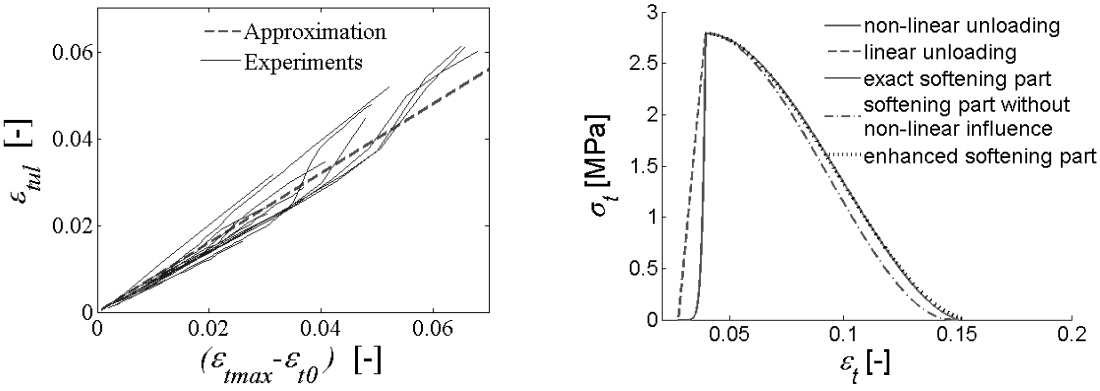

(a) (b)

Figure C.3: Tension: (a) Evolution of inelastic strain, (b) comparison of softening branches

As seen in Eq. (C.17), the damage and cracking strains are mainly driven by a single material parameter, namely b_t. By considering the standard definition of the damage parameter ω

$$E_t = (1 - \omega_t)E_0, \tag{C.19}$$

where E_t denotes actual elastic modulus, the damage variable can be determined by introducing Eq. (C.17) into Eq. (C.19) as

$$\omega_t = 1 - \frac{E_t}{E_0} = 1 - \frac{\sigma_{tmax}}{\left(\varepsilon_{tmax} - \varepsilon_{tul}\right) E_0}. \tag{C.20}$$

The transverse strain ratio in Eq. (C.11) can be then evaluated as

$$\nu_{ij} = -\nu_0\left(1 - \omega_t\right). \tag{C.21}$$

This definition assures the decreasing influence of Poisson's ratio while the material cracks.

C.2.2.2 Compression

The virgin compression loading response is shown in Fig. C.4(a) and is defined mathematically as

$$\hat{s}_c\left(\hat{e} \leq \varepsilon_{min}\right) = \begin{cases} E_0\hat{e} & 0 > \hat{e} \geq \varepsilon_{c0} \\ \sigma_{cp} - \left(\sigma_{cp} - \sigma_{c0}\right)\left(\frac{\varepsilon_{cp}-\hat{e}}{\varepsilon_{cp}-\varepsilon_{c0}}\right)^{E_0\frac{\varepsilon_{cp}-\varepsilon_{c0}}{\sigma_{cp}-\sigma_{c0}}} & \varepsilon_{c0} > \hat{e} \geq \varepsilon_{cp} \\ \sigma_{cp}\left[2\left(\frac{\hat{e}-\varepsilon_{cp}}{\varepsilon_{cu}-\varepsilon_{cp}}\right)^3 - 3\left(\frac{\hat{e}-\varepsilon_{cp}}{\varepsilon_{cu}-\varepsilon_{cp}}\right)^2 + 1\right] & \varepsilon_{cp} > \hat{e} > \varepsilon_{cu} \\ 0 & \varepsilon_{cu} \geq \hat{e}. \end{cases} \tag{C.22}$$

The unloading and reloading scheme is depicted in Fig. C.4(b) and is based on a similar assumptions as for tension

$$\hat{s}_c\left(\hat{e} > \varepsilon_{cmin}\right) = \begin{cases} E_0\hat{e} & 0 > \varepsilon_{cmin} \geq \varepsilon_{t0} \\ \sigma^*_{cmin}\left(\frac{\hat{e}-\varepsilon_{cul}}{\varepsilon^*_{cmin}-\varepsilon_{cul}}\right)^{a_c} & \varepsilon_{c0} > \varepsilon_{cmin} > \varepsilon_{cu}, \dot{e} > 0 \\ \sigma^*_{cul} + \left(\sigma_{cmin} - \sigma^*_{cul}\right)\frac{\hat{e}-\varepsilon^*_{cul}}{\varepsilon_{cmin}-\varepsilon^*_{cul}} & \varepsilon_{c0} > \varepsilon_{cmin} > \varepsilon_{cu}, \dot{e} \leq 0 \\ 0 & \varepsilon_{cu} \geq \varepsilon_{cmin}, \end{cases} \tag{C.23}$$

where

$$\begin{aligned} \varepsilon^*_{cmin} &= \max\left(\varepsilon_{cmin}, \varepsilon_{cprl}\right), \\ \varepsilon^*_{cul} &= \min\left(\varepsilon_{cul}, \varepsilon_{cpul}\right). \end{aligned} \tag{C.24}$$

where $\sigma^*_{cmin}, \sigma^*_{cul}$ are associated stresses and ε_{cmin} is the minimum strain reached in previ-

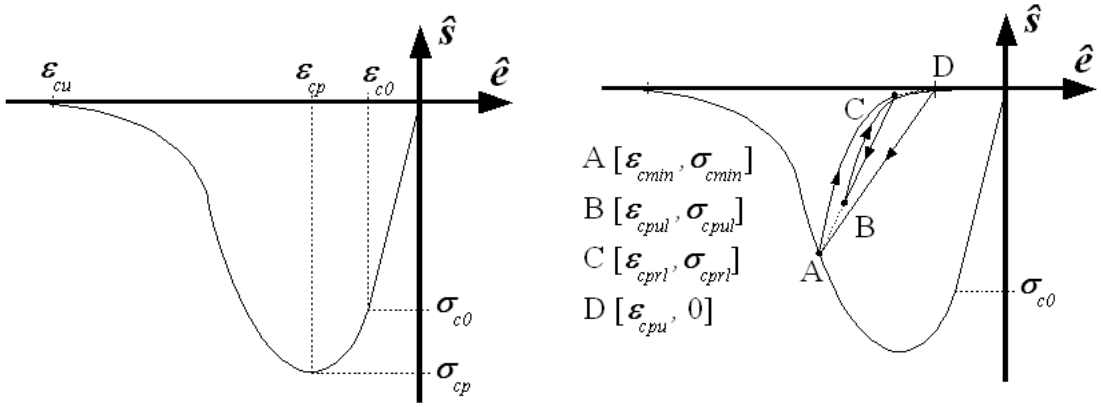

(a) (b)

Figure C.4: Compressive response: (a) Virgin loading, (b) loading/unloading

ous steps with stress σ_{cmin}. The evolution of inelastic strain is again assumed to be linearly

dependent on ε_{cmin} and crushing (Eq. (C.25)). Suppose that the strain $(\varepsilon_{cu}^{test})$ for which the force is totally released is determined from the experimental test and the corresponding localisation band in real material is denoted d_c. Next, with the knowledge of the remaining material parameters, we can define the displacement needed for releasing correct energy during material softening as $w_c = [\varepsilon_{cu}^{test} - b_c(\varepsilon_{cp} - \varepsilon_{c0})]\, d_c$. The inelastic strain then takes the form

$$\varepsilon_{cul} = \begin{cases} 0 & 0 > \varepsilon_{cmin} \geq \varepsilon_{c0} \\ b_c(\varepsilon_{cmin} - \varepsilon_{c0}) & \varepsilon_{c0} > \varepsilon_{cmin} \geq \varepsilon_{cp} \\ \min\{b_c(\varepsilon_{cp} - \varepsilon_{c0}) + b_c[\varepsilon_{cmin} - b_c(\varepsilon_{cp} - \varepsilon_{c0}) - \sigma_{cmin}/E_{cp}], & \\ b_c(\varepsilon_{cp} - \varepsilon_{c0} + w_c/h)\} & \varepsilon_{cp} > \varepsilon_{cmin}. \end{cases} \tag{C.25}$$

The material parameters a_c and b_c have to be determined from experimental test results.

The dissipated energy during the crushing should also be mesh-independent as for tensile cracking. Therefore, the strain ε_{cu} is defined with respect to the mesh size as

$$\varepsilon_{cu} = \varepsilon_{cp} + \frac{w_c}{h} - 2\frac{\varepsilon_{cp} - b_c(\varepsilon_{cp} - \varepsilon_{c0})}{a_c + 1}, \tag{C.26}$$

where h represents the equivalent band (element size) where the crushing occurs and is determined at its initiation. The damage parameter is determined, in a similar fashion as for tensile (Eq. (C.20)) as

$$\omega_c = 1 - \frac{E_c}{E_0} = 1 - \frac{\sigma_{cmin}}{(\varepsilon_{cmin} - \varepsilon_{cul})\, E_0}. \tag{C.27}$$

C.2.3 Biaxial behavior

To demonstrate the complex behavior of the pro-posed approach the failure envelope in space of principal stresses is shown in Fig. C.5. The boundaries are influenced by the transverse strain ratio of cracked and crushed material which is expected when the failure criterion is based on principal strains. This disadvantage of the presented model can be solved by defining the dependence between tensile and compressive strength. Nevertheless, the real shape of failure envelope for SHCC will only be included at a later stage as the bi-axial behavior is currently under investigation at Stellenbosch University.

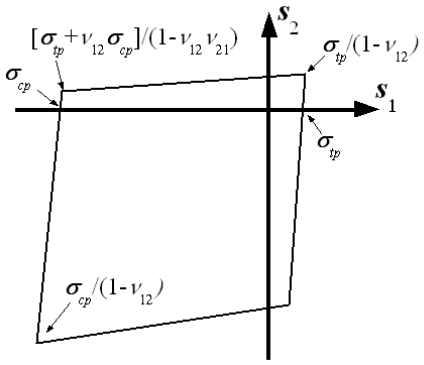

Figure C.5: Failure envelope in the principal stress space

C.2.4 Cyclic loading

The above described model is adjusted for cyclic loading when the orientation of principle stresses changes. The residual deformations are assumed to be dependant on the inelastic strain. Therefore, a simple linear definition is employed and the permissible closing (opening) strain is evaluated as

$$\varepsilon^{cl}_{t(c)} = b^{cl}_{t(c)}\varepsilon_{tul(cul)}, \tag{C.28}$$

where b^{cl}_t and b^{cl}_c are material parameters and can therefore be calculated from reverse cyclic loading tests. The trajectories of reloading after the stress state change are in a good agreement with experimental results presented in (Billington, 2004).

For the space limitation only tension behavior after stress state change is introduced (Eqs. (C.29,C.30)). The stress evolution for compression can be obtain by substitution of tensile driving parameters for compressive variables and replacement of the maximum (max) with the minimum (min) value and vice versa. Note that during the loading after stress state change the old cracks are reopened and the tangent modulus increase to reach the value of the previously experienced modulus E_t.

$$\sigma\left(\dot{e} \geq 0\right) = \sigma^*_{tul} + \left(\sigma^{**}_{tmax} - \sigma^*_{tul}\right)\left(\frac{\hat{e} - \varepsilon^*_{tul}}{\varepsilon^{**}_{tmax} - \varepsilon^*_{tul}}\right)^{E_t \frac{\varepsilon^{**}_{tmax} - \varepsilon^*_{tul}}{\sigma^{**}_{tmax} - \sigma^*_{tul}}}, \tag{C.29}$$

$$\sigma\left(\dot{e} < 0\right) = \sigma^*_{tmax}\left[\frac{\hat{e} - \varepsilon^{**}_{tul}}{\sigma^*_{tmax}/E_t}\right]^{a_t}, \tag{C.30}$$

where the driving parameter $\hat{e}$ is again shifted to correspond with the diagram for a virgin loading and $\varepsilon^{**}_{tmax} = \max\left(\varepsilon_{t0}, \varepsilon_{tmax}\right)$ with associated stress σ^{**}_{tmax}. The experienced modulus

is determined as

$$E_t = \begin{cases} E_0 & \varepsilon_{tmax} \leq \varepsilon_{t0} \quad \text{(C.31)} \\ \dfrac{\sigma_{tmax}}{\varepsilon_{tmax} - b_t\left(\varepsilon_{tmax} - \varepsilon_{t0}\right)} & \varepsilon_{tmax} > \varepsilon_{t0}, \quad \text{(C.32)} \end{cases}$$

and inelastic strain ε_{tul}^{**} is assumed to be

$$\varepsilon_{tul}^{**} = \min\left[\varepsilon_{tmax}^{*} - \sigma_{tmax}^{*}/E_t, b_t\left(\varepsilon_{tmax} - \varepsilon_{t0}\right)\right]. \quad \text{(C.33)}$$

To demonstrate the model response, a loading change from tension to compression to tension (A-G) is shown in Fig. C.6(a):

- A-B: initial virgin loading (Eq. (C.14)),
- B-C: unloading, Equation (Eq. (C.15)),
- C-D: cracks closing and compressive loading,
- D-E: virgin loading (Eq. (C.22)),
- E-F: unloading (Eq. (C.23)),
- F-G: cracks reopening and tensile loading (Eq. (C.29)),
- G-H: virgin loading (Eq. (C.14)).

Note that if the loading follows the stress state change, the loading path has the tangent equal to the actual modulus (Eq. (C.29)), intervals F-K and L-G in Fig. C.6(b). The unloading from this stage is defined in Eq. (C.30), see interval K-L in Fig. C.6(b).

C.3 Implementation and application

As mentioned in the previous section, the constitutive model is implemented in the commercial available finite element code **DIANA** version 9.3 using the "User supplied subroutine" option to demonstrate its suitability for SHCC. Newton-Raphson iterative procedure is used for the solution of nonlinear equations.

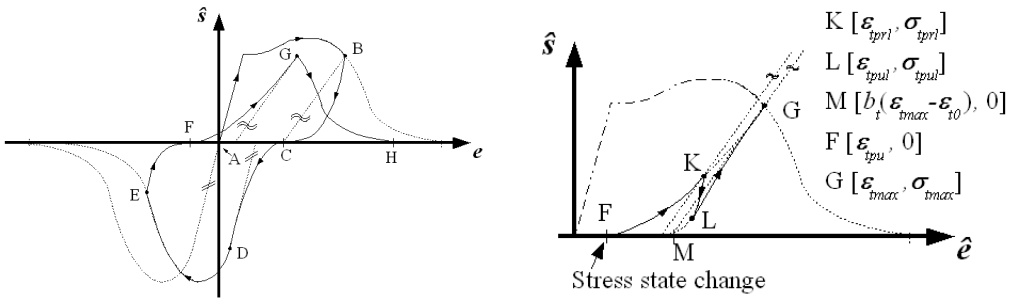

(a) (b)

Figure C.6: Schematic cyclic behavior

Finite element analyses of the flexural tests reported in (Boshoff, 2007) are performed to verify the constitutive model analyses. The three-point bending test is introduced using parameters presented in (Boshoff, 2007), see Tab. C.1. The obtained results are compared with experimental data as well as a smeared crack model based on a damage mechanics formulation done by Boshoff (2007).

C.3.0.1 Three-point bending test

The experimental setup is depicted in Figure 9. It is noteworthy that the beam is relatively thin which complicated the numerical modelling. As mentioned in (Boshoff, 2007), this beam demonstrates strong alignment of fibers close to the surface which results in a stronger, more ductile response. Therefore the results of the model are expected to underpredict the flexural behavior. This issue is however not addressed in this section.

C.3.0.2 Model description

The numerical model is based on experimental data obtained over the past 5 years by the Institute of Structural Engineering based at the Department of Civil Engineering, Stellenbosch University. Due to the lack of a reverse cyclic loading some parameters are set up using the engineering judgement of the authors as this will not have a significant influence on the presented results. All the parameters used are listed in Tab. C.1. To examine the feasibility of the proposed numerical approach, two different meshes are used. The flexural test

is modelled using linearly interpolated, four node plane stress elements. The finite element mesh is refined towards the middle of the beam with the size of the elements in the expected softening and localization zone 1.3 mm x 1.33 mm and 4.0 x 4.0 mm. The former dimension of elements in the middle of the beam is chosen in accordance with the theory introduced in (Boshoff, 2007) to deal with the crack spacing. The boundary conditions of the model are shown in Fig. C.7(a) as well as the beam dimensions. The other mesh size is chosen to study the mesh sensitivity.

Table C.1: Model parameters

General			Tension			Compression		
Param.	Value		Param.	Value		Param.	Value	
E	$9.2 \cdot 10^3$	MPa	ε_{t0}	$2.42 \cdot 10^{-4}$		ε_{c0}	$-2.5 \cdot 10^{-3}$	
ν	0.35		ε_{tp}	$3.92 \cdot 10^{-2}$		ε_{cp}	$-3.5 \cdot 10^{-3}$	
			σ_{tp}	2.79	MPa	σ_{cp}	-25.0	MPa
			w_t	6.0	mm	ε_{cu}	$-1.00 \cdot 10^{-1}$	
			a_t	3.0		d_c	50	mm
			b_t	0.8		a_c	3.0	
			b_t^{cl}	0.8		b_c	0.7	
						b_c^{cl}	0.6	

C.3.0.3 Results

The presented crack rotating model (RCM) is used to obtain the force-deflection diagrams. These results are plotted in Fig. C.7(b) together with the experimental data and response produced by the model based on a damage mechanics formulation (DM) by Boshoff (2007). As can be seen, the numerical models demonstrate good agreement with experimental data in the elastic as well as hardening part. The discrepancy is detected for the softening part. This is probably caused by the fibers alignment close to the surface which is not taken into account for generally used numerical models and the interested readers are referred to Boshoff (2007). The mesh dependency is observed by comparison of the two different mesh sizes.

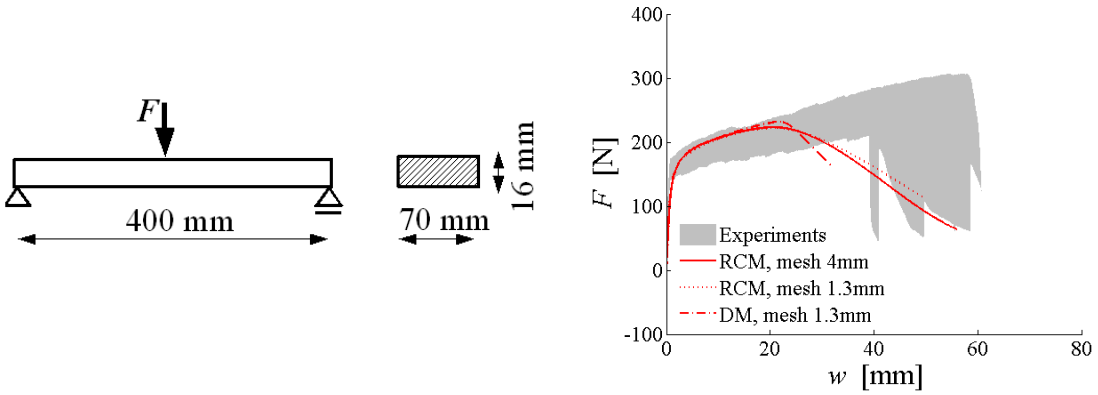

(a) (b)

Figure C.7: Three-point bending test: (a) Setup, (b) results

To provide entire overview about the model the evolution of strain in the longitudinal direction is shown in Fig. C.8. After the first elastic stage the strain starts to localize into the elements which undergo hardening and then softening. Note that more than one element can soften before the strain is finally localized into one single crack. This is believed to be the reason for the shown mesh dependence (Boshoff, 2007).

C.4 Conclusion and future work

In this study a two-dimensional numerical model for Strain Hardening Cement-based Composites was introduced. This approach is based on a rotating crack model implemented in the commercially available software package **DIANA**. The presented model takes into account:

- strain hardening and softening in tension as well as in compression,
- nonlinear unloading,
- nonlinear loading after stress state change - crack closing,
- the effect of Poisson's ratio.

The suitability of the introduced approach was demonstrated by means of a three-point flexural test. Nevertheless, the model should be verified for different loading conditions before

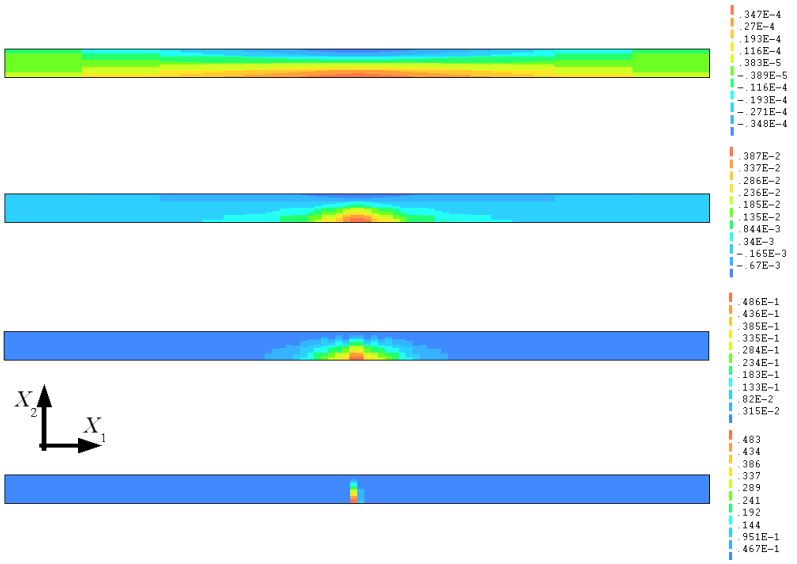

Figure C.8: Evolution of ε_{11} during three-point flexural test simulation (load vs. mid-span vertical deflection

using for larger structural components. The spurious stress transfer associated with the rotating crack models has to be treated simultaneously, for more see (Jirásek and Zimmermann, 1998). The authors also intend to incorporate the time-dependent behavior in the model.